2011

Validation of a simple go/no-go damage detection system for personal ceramic body armor using pressure sensitive film

Jason Fisher
Iowa State University

Validation of a simple go/no-go damage detection system for personal ceramic body armor using pressure sensitive film

by

Jason Travis Fisher

A thesis submitted to the graduate faculty

in partial fulfillment of the requirements for the degree of

MASTER OF SCIENCE

Major: Engineering Mechanics

Program of Study Committee:

Dale Chimenti, Major Professor

Wei Hong

Nicola Bowler

Iowa State University

Ames, Iowa

2011

TABLE OF CONTENTS

LIST OF TABLES

LIST OF FIGURES

ACKNOWLEDGEMENTS

I would like to thank my graduate professor Dr. Dale Chimenti for his help and guidance throughout my research. I would also like to thank Nathan Braymen for his contributions to my work. I would like to acknowledge the Army Research Labs through which funding for this work was provided.

ABSTRACT

A method for predicting damage in ceramic body armor using pressure sensitive dye-indicator film (PSF) is presented. Results from impact experiments using impactors of various masses onto ceramic armor panels, employing the use of a CPR manikin to model the human torso are presented. Trends of increasing impactor acceleration and force as a function of increasing impact energy are shown. Differing acceleration profiles between damaged and undamaged armor panels is seen. Experiments employing the pressure sensitive film are presented. Indication on the PSF show good correlation to the measured force of the impact. Correlation extends for each impactor through a wide range of impact energies. A simplified numerical model was developed that captures the general trends of the experimental data. An analytical model is shown to accurately predict the maximum acceleration values for each impactor through a range of impact energies. Also presented are the results of ballistics testing performed on both undamaged and damaged armor panels.

CHAPTER 1. INTRODUCTION

Advances in personnel body armor over the past 60 years have led to its wide spread usage today [Matchen (1996)]. Most current threats to which soldiers are exposed can only be defeated by the use of hard armor. Ceramic-based hard armor has always been preferred because it provides good ballistic defeat properties for a relatively low weight [Gooch (2002), Sujirote et al. (2008)]. Government standards require personnel armor to be damage-free to guarantee effectiveness. Studies by the U.S. and England have shown that while cracked plates are still able to defeat a threat, their ballistic performance is degraded [Dulay et al. (2006), Horsfall et al. (1993)]. The high cost of individual ceramic armor leads to the need for nondestructive evaluation (NDE) techniques that can readily detect damage in ceramic armor.

Current NDE techniques used on ceramic armor rely on some form of imaging using x-rays, ultrasonics, or microwaves. Equipment to perform such techniques may be setup on location, but require a trained operator. New advances in the field of NDE have led the way for some automated systems that require no experienced operator or personnel to interpret results. Haynes et al. (2009) have described and assessed an automated x-ray scanner developed by the Army and Schimdt et al. (2009, 2010) have detailed a portable microwave scanner that does not require an operator to interpret results. These systems still require expensive electronic equipment and for a soldier to surrender their armor for an extended period. Efficient methods to determine damage in ceramic armor that reduces the time a soldier is without their armor and requires little experience or training to perform are desirable.

The purpose of this thesis is to validate experimentally the use of a pressure sensitive dye indicator film (PSF) as a viable means of detecting subcritical damage in personal ceramic body armor. Damage is considered subcritical when it occurs from a non-ballistic, low velocity impact such that the armor is visibly undamaged. Application of PSF eliminates the need for

any electronic device to measure damage or interpret test result. Elimination of electronics and the need for trained operators provides a simple, fast, and effective in-field evaluation of possible impact damage.

This thesis presents the experimental testing of a damage detection system for personal ceramic body armor using PSF. In Chapter 2, a historical background of personal body armor will be given along with current NDE techniques used to detect subcritical damage. Chapter 3 will detail the experimental setup used and numerical analysis performed, together with the analytical methods that have been used to model subcritical impacts. In Chapter 4, the results of the experiments and numerical analysis are discussed. Finally, a summary and conclusions are presented in Chapter 5.

CHAPTER 2. REVIEW OF LITERATURE

This chapter provides a description of personnel ceramic body armor and covers a brief background of the development of ceramic armor that has led to its favored and prominent use and why the critical need to keep the armor damage free exists. Also discussed are current NDE techniques available and widely used to detect damage in ceramic body armor. Finally, the use of pressure sensitive dye indicator film as an NDE technique for damage detection in ceramic armor is presented.

2.1 Personnel ceramic body armor

Personnel ceramic body armor is used primarily when high velocity, full metal jacket or hard-core rounds are the primary threat. Typical ceramic body armor consists of a monolithic ceramic plate bonded to a composite type backing material made of high strength fibers such as Kevlar, Twaron, or Spectra, and wrapped in ballistic nylon; in some cases, soft metallic materials may be used as the backing material [Medvedovski (2006)]. Most ceramic armors in use today employ alumina (Al_2O_3) as the ceramic material. When weight reduction is a primary concern, silicon carbide (SiC_3) and boron carbide (B_4C_3) ceramics may be used; however, their high cost as compared to alumina limits their current use. The purpose of the ceramic material is to blunt and degrade the bullet. As the ceramic fractures and the bullet penetrates the material, ceramic pieces shred off parts of the bullet reducing its kinetic energy and blunting the bullet nose. The composite layer then absorbs the remaining energy of the bullet and fractured ceramic pieces, in much the same as a standard flexible (e.g. Kevlar) vest, preventing penetration of the person being protected.

2.2 Development of ceramic armor

The credit for the first 20^{th} century use of body armor goes to the Germans during World War I (WWI) [Viechnicki et al. (1991)]. They applied hard-faced enamel coatings to their tanks to protect against small arms fire. Soon thereafter and throughout World War II (WWII), German researchers began to study impact penetration into glass [Skaggs (2003)]. During WWII, nonmetallic armors were tested on aircraft to prevent against small arms fire and shell fragments. During the Korean War work started on siliceous cord armors (metal armor cast around a silicate core) to protect tanks against kinetic energy threats [Viechnicki et al. (1991)].

U.S. research programs were first instituted in the 1960s. Body armor was desired for soldiers in Vietnam who were standing guard at night and needed protection from sniper fire [Skaggs (2003)]. Eventually armor plates made of alumina were used. The armor was heavy, approximately 60-lbs for a front and back plate, and only practical for sentry use. During Vietnam, helicopter pilots also required armor to protect against small arms fire. They first used flak vests from WWII bombers but the vests were only designed to protect against shell fragments, and they provided no protection against small arms and machine gun fire. Owing to weight constraints, ceramics were viewed as a possible armor material. Eventually alumina plates were developed and added to aircraft. With the addition of these plates, a reduction in injuries from small arms and machine gun fire was observed. Both of these early armors were composed of sintered alumina plates bonded to a backing material made of either a ductile metal (e.g. aluminum or soft steel) or fiberglass-reinforced plastic [Matchen (1996)].

Many key design points for ceramic armor were discovered during research in the 1970s. Mark Wilkins at Lawrence Livermore National Laboratory (LLNL) put together a set of empirical rules for ceramic armor design based on his work in the 1960s and 70s [Skaggs (2003)]. The basic design points Wilkins listed, which he expanded on for armor contractors and manufacturers, include:

1) The armor needs to be as hard as the bullet (or harder) to defeat the bullet.

2) The armor layer needs to be at least 1/2 the bullet diameter in thickness to successfully defeat the bullet.

> 3) The front ceramic needs to be about 1/3 the thickness of the total plate and the backing material needs to be about 2/3 of the total.
>
> 4) The basic characteristics of the composite plate are that the front armor material needs to break and turn the bullet and the backing material needs to be ductile to catch the penetrating products without failing.
>
> 5) Understanding the fracture/cracking/breakup of the ceramic is only important for thick ceramics.

Wilkins's guidelines are still regarded as the basic layout for designing an effective ceramic-based hard armor. Large research programs continued through the 1980s when DARPA issued requests for proposals for new vehicle and body armor designs. During this time, through extensive investigation, five materials were identified as being the most promising for ceramic body armor. These materials include alumina (Al_2O_3), silicon carbide (SiC_3), boron carbide (B_4C_3), titanium diboride (TiB_2), and aluminum nitride (AlN). Today these materials are still the most widely used and researched for ceramic armor. It was discovered by Carl Cline at LLNL in the 1970s [Skaggs (2003)] that diberyllium boride (Be_2B) was by far the lightest ceramic that had ballistic stopping capabilities, however beryllium is toxic if inhaled and the Army listed it as an unacceptable material for armor.

In the late 1980s the phenomenon of dwell was discovered as remarked by Skaggs (2003).

> As the bullet entered a strongly confined target, it seemed to stall in the penetration process at the surface of the ceramic. Upon careful examination it was found that the penetrator spread out radially at a 90 degree angle with respect to the penetration axis ... [dwell] was observed to take place in all of the strongly confined ceramic targets during the first 10 microseconds of the penetrator passing into the target.

Further research since the first observance of dwell has revealed that delaying the fracture of the ceramic and increasing the length of the dwell time of the bullet by only a minimal amount of time can considerably increase the ballistic performance of a ceramic material [Skaggs (2003)].

Armor research began to diminish in the 1990s until most armor programs were stopped. During the 1990s, most research advances were in the realm of computer modeling. Skaggs (2003) has summarized much of the computing advances that took place during the 1990s.

> Anderson and Walker at Southwest Research Institute have developed newer and more closely coupled first principles models for the behavior of penetrators into armors of all kinds, but specifically the multilayered composite armors of ceramics and high strain/strain rate backing materials. In addition, they have created a database of materials tested for armor applications... Sandia National Laboratory has maximized the use of the CHT code to study many different types of armors and the interactions of penetrators with these armors. Frank Adessio at Los Alamos has attacked the problem of modeling fiber reinforced plastics on a microscale... Shocket et al at SRI International have attempted to rationalize all of the engineering models extant into one that would be very beneficial to the military services... Holmquist and Johnson at the US Army Supercomputing Center at the Univ. of Minnesota have continued to refine the EPIC model by incorporating newer cell configurations and continue to develop the model to account for damage to the material during the penetration.

Skaggs (2003) also notes that currently no armor in use today has been designed by computer. Along with computer advances, advances have occurred in armor materials. Following the five monolith ceramics recognized as best suited for armor, ceramic matrix composites, ceramic fibers embedded in a ceramic matrix, are recognized as having desirable ballistic qualities and are the most researched armor materials.Viechnicki et al. (1991) lists the following ceramic matrix composites as potential armor materials: Al_2O_3/SiC whiskers, Ni/TiC, borosilicate glass/SiC or C fibers, TiB_2/B_4C particulates,TiB_2/SiC particulates, and Al/B_4C particulates. A particularly undesirable quality monolithic ceramics have is the amount of damage they sustain during a single impact, making it difficult for current armor to provide multiple-hit protection. Owing to the material properties of ceramic matrix composites, their fracture mechanics properties in particular, damage they sustain from ballistic impacts is localized. While

not as developed and researched as monolithic ceramics, the damage localization effect of ceramic matrix composites has armor produced from these materials showing promising results for multiple-hit protection [Viechnicki et al. (1991)].

A high expense has always been associated with ceramic armor. Two prominent reasons contribute to the high cost of ceramic armor seen today. Manufacturing contributes the largest cost to ceramic armors, owing to the requirement that most armor ceramics require hot pressing to be fully bonded, made pure enough, and free of any internal discontinuities [Matchen (1996)]. The shapes desired for personnel armor add in additional complications to the manufacturing process that increases costs. Another reason contributing expense to ceramic armor is the amount of raw materials available. Alumina has always been the least expensive armor material due to the many other industrial uses that it has; thus, alumina is produced in millions of pounds per year [Skaggs (2003)]. Other armor materials, especially B_4C_3, have minimal industrial uses, resulting in only small quantities of their raw materials to be produced each year, contributing to high costs of ceramic armor employing them [Skaggs (2003)].

Initially silicon carbide and boron carbide were favored materials for use in ceramic armor, primarily for their high hardness/strength to weight ratio [Skaggs (2003)]. The high cost associated with these material has not allowed for their wide spread use in ceramic armor. Research during the 1970s and 80s showed that if alumina can be made to a high purity of an Al_2O_3 content of 96% or greater, and the grain size can be minimized, the ceramic armors produced from such alumina are comparable in terms of ballistic performance and the amount of material needed (thickness of ceramic plate) to prevent penetration with those of silicon carbide and boron carbide [Medvedovski (2002), Skaggs (2003)]. Alumina is currently the preferred material for all ceramic armor, personnel and vehicle, with silicon carbide and boron carbide only implemented when weight reduction is a high priority.

The bullet defeat process of ceramic armor has three general stages that apply to any ballistic threat and ceramic armor design [Matchen (1996), Gooch (2002)]. The first stage, referred to as the shattering stage, involves the initial impact of the bullet against the ceramic material in the armor. The high hardness and compressive strength of the ceramic as compared to that of the bullet initiates fracture in the bullet. The fracturing of the bullet is followed by

damage accumulation in the ceramic as stress waves propagate through the ceramic material. In the second stage, referred to as erosion, cracks develop in the ceramic material and pieces of the ceramic aid in eroding parts of the bullet as it moves through the material. The third stage, catching, occurs as the bullet and pieces of the ceramic impact the backing material, where their remaining kinetic energy is absorbed. Figure 2.1 shows the three stages of the bullet defeat process.

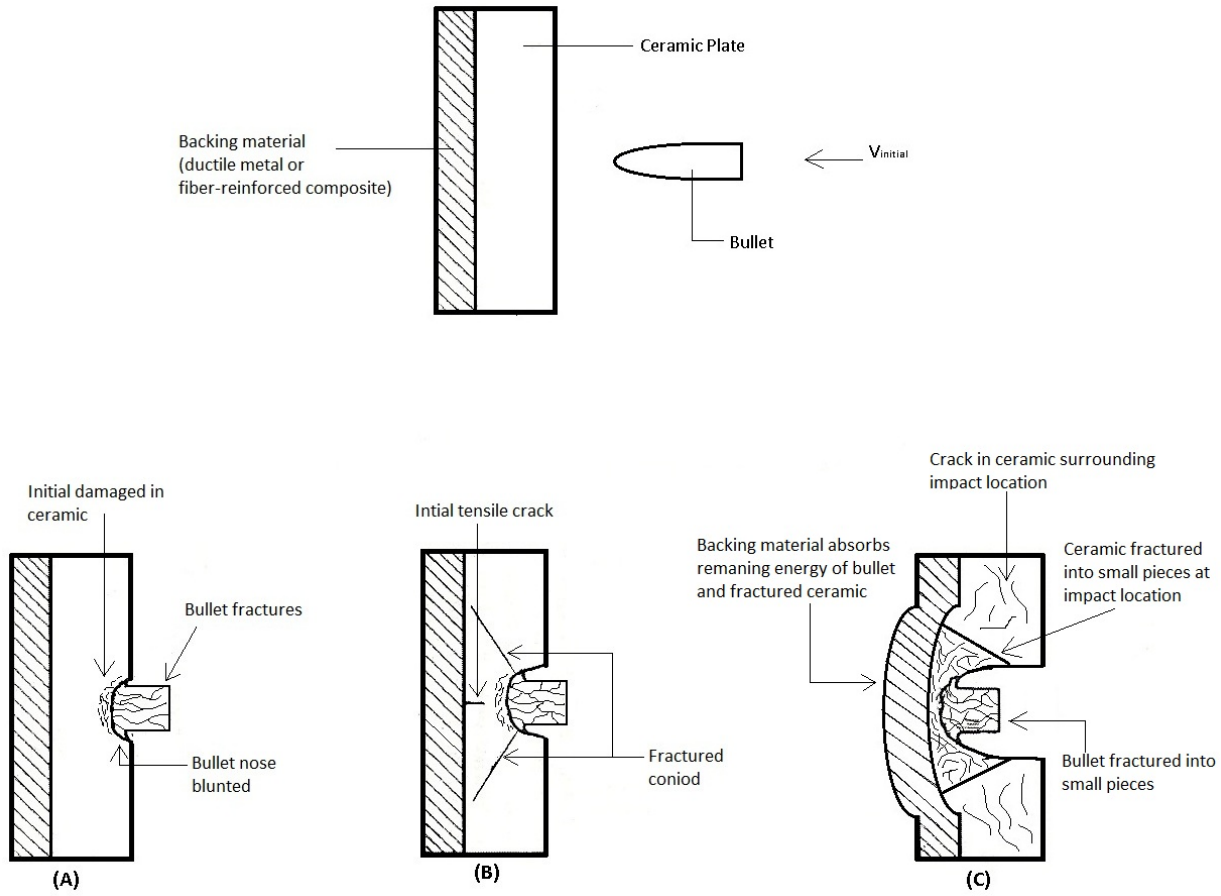

Figure 2.1 Three stages of the bullet defeat process. (A) First (shattering) stage, (B) second (erosion) stage, (C) third (catching) stage.

While the bullet defeat process may be generalized for any given ballistic threat and ceramic armor design, the particulars of an individual impact depend on the velocity of the ballistic threat. Skaggs (2003) has described the velocity dependence of the bullet defeat process.

> The response of armor ceramics to impact can be divided into the three velocity regimes: low velocity, V < 700 m/s; intermediate velocity, 700 m/s < V < 3000 m/s; and hypervelocity, V < 3000 m/s. At low velocities mechanical properties, either quasi-static or dynamic, govern penetration. At hypervelocities, the velocities of shaped charged jets, the materials behave as fluids or hydrodynamically during penetration. Penetration in the intermediate regime, where military kinetic energy threats fall, is governed by dynamic material properties and hydrodynamic flow. Penetration in the intermediate velocity regime consists of at least four stages which include (1) initial impact with hydrodynamic flow of penetrator and armor ceramic; (2) breakup and continued flow of penetrator and high-speed jetting of ceramic debris; (3) ceramic fracture, formation of Hertzian cone crack, and tensile crack on the back face, with continued penetrator breakup and flow; and (4) erosion of penetrator and wide spread fracture of ceramic.

The first standard ballistic performance criterion developed, and in continued use presently, is referred to as the V_{50} [Viechnicki et al. (1991)]. The V_{50} is the velocity at which 50% of the bullets will penetrate the armor. Still a primary means of characterizing ballistic performance, the V_{50} provides only a broad indication of the ballistic performance of a ceramic armor. Horsfall et al. (1993) summarizes the testing procedure involved in determining an armor's V_{50} as detailed by NATO.

> [NATO procedure] dictates that the [V_{50} ballistic] limit velocity is the mean of 6 shots, the three highest velocities must lie within a range of 40 m/s. If the range of velocities is greater than the average is taken over 10 shots, which must then be within a range of 50 m/s.

Owing to the destructive nature of determining an armor's V_{50} and the cost associated with individual ceramic armor pieces, many have attempted to relate a specific material property of the ceramic used in a particular armor to the ballistic performance of that given armor, allowing for both a simple evaluation of a ceramic armor's ballistic performance and for the comparison of separate ceramic armor designs. Currently no individual material property of a

ceramic has been correlated directly to the ballistic performance of a particular ceramic armor design. The absence of a material property/ballistic performance relationship is attributed to the complicated dynamic fracture process that occurs during a ballistic impact. An unexplained phenomenon exists regarding a ceramic armor's V_{50}, remarked by Skaggs (2003), which has added to the desire for a new ballistic performance criterion.

> For a specific armor, there exists two V_{50}'s. As the velocity increased the intact bullet penetrated the armor to define the first V_{50}. But upon further increase the bullet shattered into many small pieces and no longer penetrated the armor. Continuing to increase the velocity produced another V_{50} above which the bullet fragments penetrated the armor again. This phenomenon has been observed by nearly everyone who tests armor, but it has never been fully explained.

Horsfall et al. (1993) describes an additional measure of ballistic performance for ceramic armor that, while it is not currently a standard, may provide a better measure of a particular armor's ballistic performance and is more readily understood.

> An alternative measure of armour performance is to determine the highest velocity at which a projectile can strike with a negligible probability of penetration, the V_0 ballistic limit velocity. It has been suggested [Tobin (1993)] that the V_0 ballistic limit velocity, may be a better measure of performance as it is more indicative in real terms of the ability of an armour to defeat a given threat and is a more readily understood concept to potential users.

While no individual material property of a ceramic may provide an indication of ballistic performance, a set of material properties has been identified that are common to all well performing ceramic armors. Viechnicki et al. (1991) and Medvedovski (2005) detail specific material properties of ceramics and the properties's corresponding influence on the ballistic performance of a piece of ceramic armor. Particular ceramic material properties of importance are the hardness and density. The ceramic is required to be as hard as or harder than the threat (bullet or bullet-core) it is meant to defeat and the density should be kept to a minimum else the

armor becomes a hindrance to the soldier. The ceramic should have a high sonic velocity to help match its acoustical impedance to that of the bullet as best as possible. The transmission of energy through shockwaves becomes important as the velocity of the bullet increases. Fracture of the ceramic in the transgranular mode is desirable. Other properties include minimal porosity (water absorption must be less than 0.02%), high elastic modulus, low Poissons ratio, and high mechanical strength. For a given armor design, the material properties must be balanced based on the primary threat the particular piece of armor is meant to defeat. James (2002) details the importance of the adhesive used to bond the ceramic and composite backing. The acoustical impedance of the adhesive should match that of the ceramic as best possible. Even a minimal mismatch can lead to strong tensile waves being reflected back through the ceramic and the joining surface causing extensive cracking of the ceramic and possibly reducing the ability of the ceramic to stop the bullet.

2.3 Current NDE

Limited data exists on the effects of cracks in ceramic armor and their effect on the ballistic performance of the armor. Horsfall et al. (1993) and Dulay et al. (2006) note the degradation observed in a ceramic armor's ballistic performance when cracks are present. Horsfall et al. (1993) describes the possible reasons why ceramic armors with cracks have lower ballistic performances.

> If there is a pre-existing large crack in the ceramic in the impact area then it might be expected to reduce the performance of the armour. The unconfined material at the fracture surfaces would fail prematurely under a compressive load and comminuted material could flow into the crack allowing premature compressive collapse. Additionally the stiffness of the armour structure might be reduced, leading to increased radial cracking due to the bending of the armour panel.

Horsfall et al. (1993) performed a series of ballistic tests on ceramic armor panels with through thickness cracks in the ceramic material. They noted a minimal but statistically significant drop in the ballistic performance of the cracked armor panels.

> . . . therefore it can be seen that the introduction of a full width, through-thickness, pre-crack reduces the V_{50} ballistic limit velocity from 764 m/s to 740 m/s, a drop of 3% . . . The Students t-test was then used to determine the significance of the difference in the [V_{50}s] of the standard and pre-crack samples. This difference was determined to be statistically significant to a level of better than 1%. Therefore it is possible to conclude that the pre-crack does significantly reduce the V_{50} ballistic limit.

Owing to the statistically significant drop in the ballistic performance of ceramic armor with cracks present, the ability to determine the condition of the ceramic material in the armor once the armor has been assembled, ceramic and composite bonded and wrapped in ballistic nylon, is necessary. The NDE tests available to detect damage in assembled ceramic armors are limited. Ultrasonics are not readily used owing to the requirement that the armor needs to be partially disassembled and ceramic surface prepared for the techniques to be applicable. The first standard NDE technique developed for in field use, and still in prevalent use, was the torque test described by Haynes et al. (2009).

> This is a process which an individual grabs opposing corners of a plate and tries to twist the plate listening for crunching or cracking. When this test works, adjoining surfaces of a crack rub and create the sound that reveals the crack. Unfortunately, this easily-performed field test is not always reliable.

Depending on the size, location, and severity of cracks in the armor, damage can go undetected. False positives and false negatives are common [Haynes et al. (2009)].

Haynes et al. (2009) has detailed an automated NDE system using x-rays developed by the Army. The system requires an operator only to load and unload the armor panels. Image processing algorithms handle the damage analysis and automatically determine the accepting or rejecting of armor panels and isolates damaged panels. The automation of the computer algorithms require that the systems be calibrated for a specific armor design, but once completed the systems may process up to 240 armor panels an hour [Haynes et al. (2009)]. Green et al. (2009) and Brennan et al. (2010) have also detailed development of damage detection systems

using CT scans. These systems are not readily employed in field owing to the need for a trained operator and time needed to scan an individual panel [Brennan et al. (2010)]. CT scan can potentially reveal greater information about the particular damage in a given armor panel than a standard x-ray; however, CT scans do not have a better accuracy rate at detecting damage and based on the requirement that any damage in an armor panel renders it defective, the extra time and operator expense associated with CT scans does not warrant the use of them. X-ray systems have high accuracy rates, but the expense and requirements of the machines dictate they are setup in a centralized location for in field use, requiring soldiers to relinquish their armor for a period [Haynes et al. (2009)].

Schimdt et al. (2009, 2010) have detailed the development of a damage detection system based on microwave interference scanning. Systems they have described produce images similar to x-ray images. The images are not as clear and require a trained technician to interpret test results. The authors have also presented work on the development of a portable system that may be carried and used directly in-field without the need for a soldier to turn over their armor to a centralized testing facility.

2.4 Pressure sensitive dye indicator film

The work presented in this thesis is based on the use of pressure sensitive dye indicator film (PSF) as a method of damage detection. PSF employed is manufactured by the Fujifilm Corporation and distributed by Sensor Products Inc. From the website of Sensor Products Inc. on the make up and use of PSF:

> PSF is a mylar based film that contains a layer of tiny microcapsules. The application of force upon the film causes the microcapsules to rupture, producing an instantaneous and permanent high resolution topographical image of pressure variation across the contact area. PSF is between 4 to 8 mils thick allowing it to conform to curved surfaces ... Like litmus paper, the color intensity of the film is directly related to the amount of pressure applied to it. The greater the pressure, the more intense the color.

Figure 2.2 shows the makeup of PSF (obtianed from information provided on Sensor Products Inc. website).

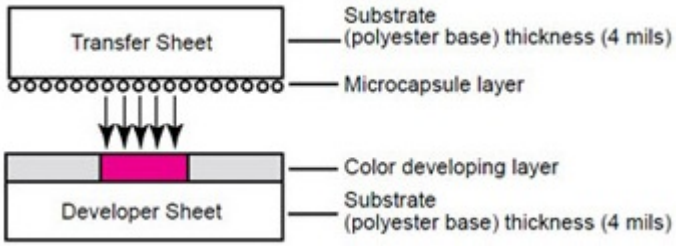

Figure 2.2 Layer by layer make up of PSF.

PSF is produced for a variety of pressure ranges. Research was conducted employing three separate pressure ranges: Medium (1400 – 7100 psi), High (7100 – 18500 psi), and Super High (18500 – 43200 psi). For each pressure range, an applied pressure that does not reach the minimum pressure value listed, produces no indication on the film. The intensity of the indication increases as the applied pressure increases within the pressure range of the film. Once the applied pressure is greater than the maximum pressure the film can measure, the film is said to be saturated. A indication is present on the film but no corresponding pressure value may be obtained. Figure 2.3 shows a sample of PSF with varying levels of indication.

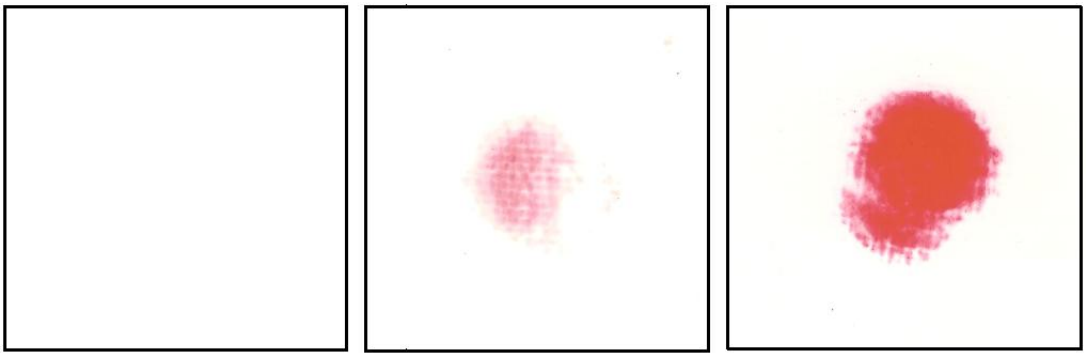

Figure 2.3 PSF samples. (left to right) unimpacted film, impact that resulted in a pressure in the middle range of the film, impact that resulted in film being over saturated.

PSF would be attached to the front (impact) face of a ceramic armor panel and then placed inside the vest. Following a sub-critical impact, the soldier would remove the armor panel and visually inspect the PSF for an indication. The absence of an indication would imply the

ceramic armor sustained no damage. The presence of an indication would imply the possibility the armor sustained damage and at which point could proceed to a testing facility for further evaluation.

PSF would not be an absolute measure of damage sustained but would provide a reliable way to determine if more intensive and accurate but time-consuming inspection should proceed, reducing the amount of time a soldier would have to relinquish their armor. PSF would provide a method to reveal if the impact sustained had the potential to damage the armor and prevent unnecessary testing after impacts that did not have the potential to cause damage. PSF may be produced in a variety of pressure ranges and based on the damage tolerance of a particular ceramic employed in an armor, an appropriate pressure range would be selected such that the minimum pressure limit of the film would correspond to the minimum impact that could potentially damage the ceramic armor.

CHAPTER 3. EXPERIMENTAL SETUP AND PROCEDURE

A series of impact experiments were performed on samples of ceramic body armor panels employing PSF. An impact test was designed and constructed along with three impactors of differing masses. In addition, ballistics tests were performed on a sampling of both undamaged and damaged ceramic armor panels. The following chapter describes the experimental setup used to perform the impact testing on the ceramic body armor and the method for which experiments were carried out. Also described is a simplified numerical model and an analytical model. Finally, the procedure followed for ballistics testing is presented.

3.1 Impact experiments and testing

To permit repeatable impact drop test to be conducted on the ceramic body armor panels, a 10-ft PVC pipe was mounted vertically along a wall to act as a guide for one of three impactors designed for these experiments, Fig. 3.1 depicts the experimental setup. The three impactors were machined out of steel and had Teflon spacers attached to them to reduce friction in the PVC pipe and to guide the masses straight down. A half inch diameter hole was machined out of the bottom (contact surface) of each impactor to allow for the insertion of a force transducer. Additionally an accelerometer was attached to the top of the transducers. Figure 3.2 shows the impactors with Teflon spacers and the machined hole for the force transducer. The final masses (weights) of the impactors were: Small impactor, 2.336-kg (5.15-lb); medium impactor, 4.245-kg (9.36-lb); and large impactor, 5.680-kg (12.52-lb). Table 3.1 lists the properties of the attainable impacts using afore mentioned experimental setup. Listed are the impact velocity, impact energy, and impact momentum for each impactor at each drop height.

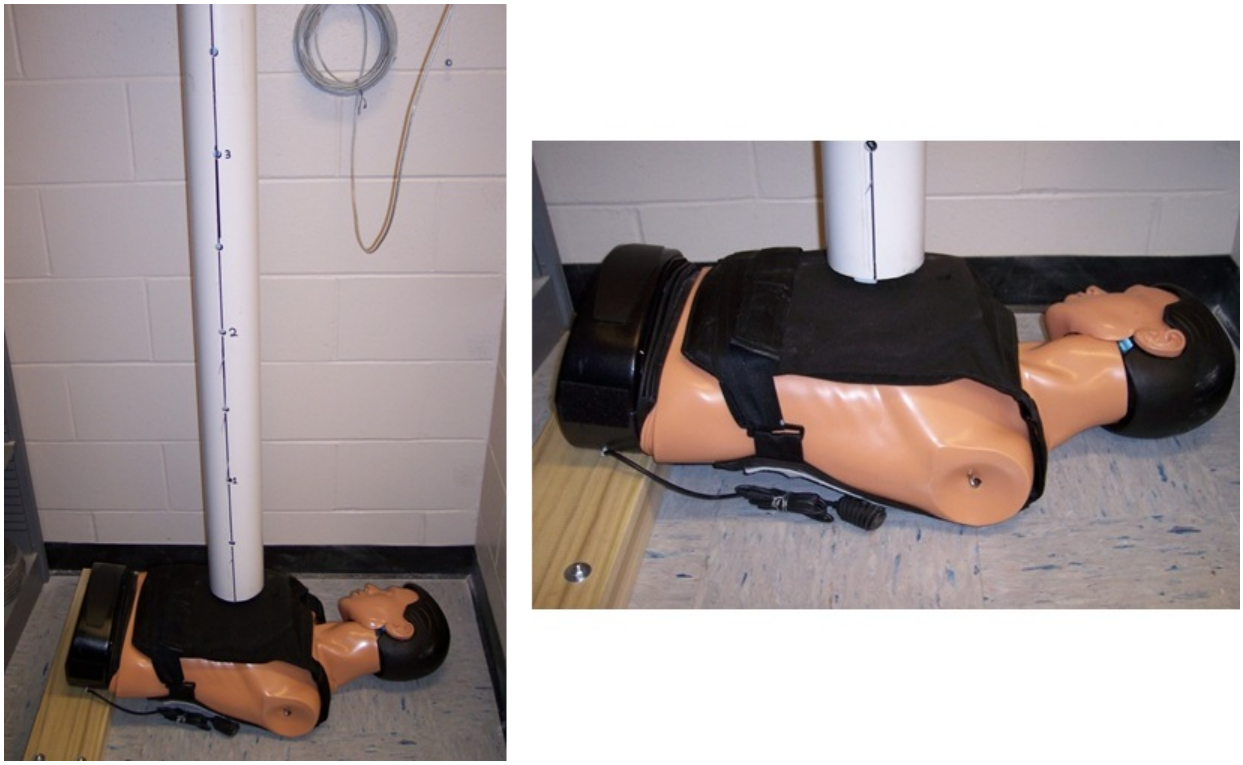

Figure 3.1 Setup for drop test experiments.

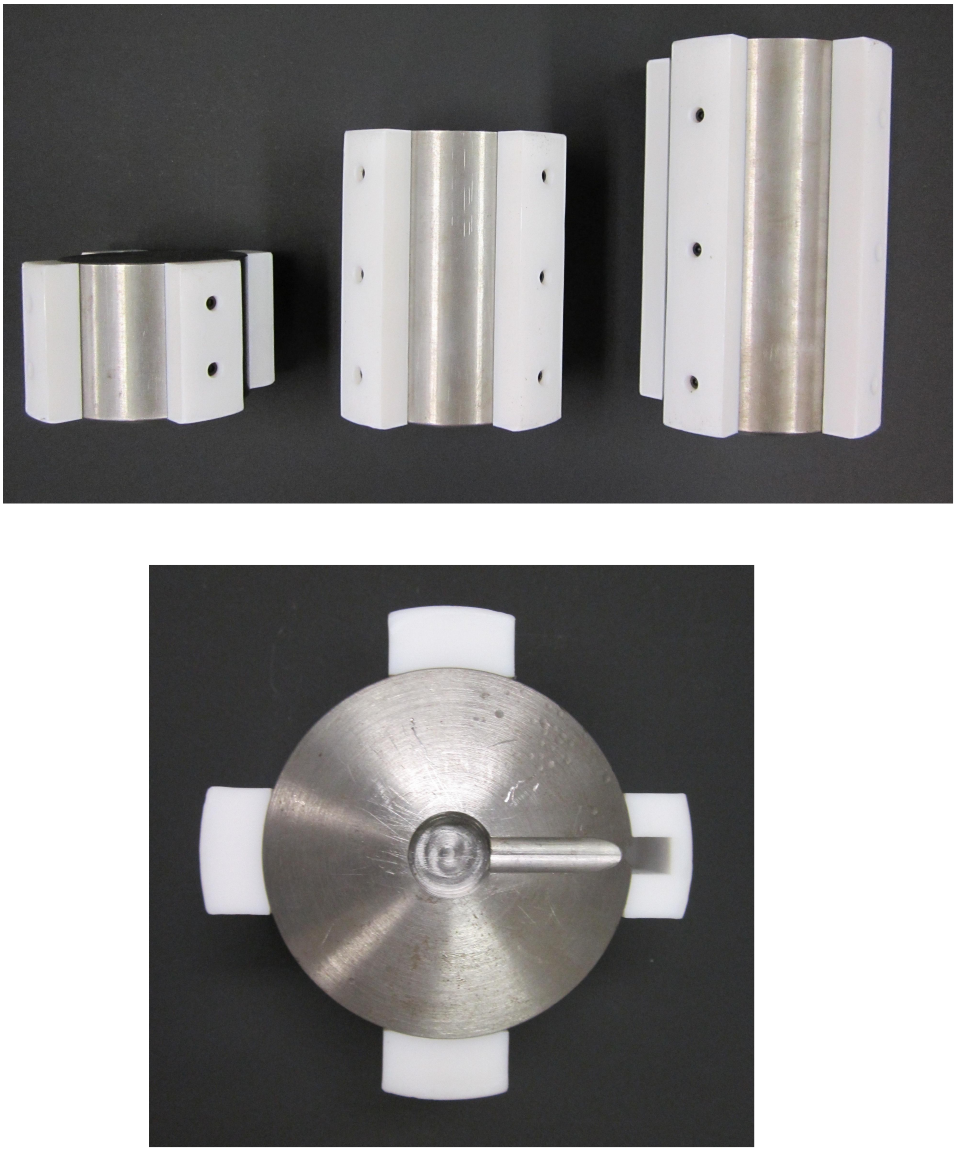

Figure 3.2 Impactors used in impact experiments. Top, left to right: small impactor, medium impactor, large impactor. Bottom: hole for force transducer.

Table 3.1 Properties of attainable impacts using experimental setup.

Drop Height		**Impact Velocity**	**Energy [J]**			**Momentum [kg*m/s]**		
[ft]	**[m]**	**[m/s]**	**Small**	**Medium**	**Large**	**Small**	**Medium**	**Large**
0.5	0.1524	1.729	3.491	6.345	8.489	4.039	7.339	9.820
1.0	0.3048	2.445	6.983	12.67	16.98	5.712	10.38	13.89
1.5	0.4572	2.995	10.47	19.03	25.47	6.995	12.71	17.01
2.0	0.6096	3.458	13.97	25.38	33.96	8.078	14.68	19.64
2.5	0.7620	3.866	17.46	31.72	42.45	9.031	16.41	21.96
3.0	0.9144	4.235	20.95	38.07	50.94	9.893	17.98	24.06
3.5	1.0678	4.574	24.44	44.41	59.43	10.69	19.42	25.98
4.0	1.2192	4.890	27.93	50.76	67.91	11.42	20.74	27.78
4.5	1.3716	5.187	31.42	57.10	76.40	12.12	22.02	29.46
5.0	1.5240	5.467	34.91	63.45	84.89	12.77	23.21	31.05
5.5	1.6764	5.734	38.41	69.79	93.38	13.40	24.34	32.57
6.0	1.8288	5.989	41.90	76.13	101.87	13.99	25.42	34.02
6.5	1.9812	6.234	45.39	82.48	110.36	14.56	26.46	35.41
7.0	2.1336	6.469	48.88	88.82	118.85	15.11	27.46	36.74
7.5	2.2860	6.696	52.37	95.17	127.34	15.64	28.43	38.03
8.0	2.4384	6.916	55.86	101.51	135.82	16.16	29.38	39.28
8.5	2.5908	7.129	59.35	107.86	144.32	16.65	30.26	40.49
9.0	2.7432	7.335	62.84	114.20	152.81	17.14	31.14	41.66
9.5	2.8956	7.536	66.34	120.55	161.30	17.61	31.99	42.81
10.0	3.0480	7.732	69.83	126.89	169.79	18.06	32.81	43.91

Figure 3.3 CPR manikin employed during impact testing. Left: manikin without vest. Right: manikin with carrying vest and armor plate.

A CPR manikin was employed to simulate the effects of a human torso during impact experiments. Ceramic armor panels were placed inside a carrying vest that was then fitted around and secured to the manikin. Figure 3.3 shows the CPR manikin employed during impact testing with and without the carrying vest and ceramic armor plate. Figure 3.1 shows a close up of the experimental setup with CPR manikin in place under drop test tube.

Figure 3.4 shows a comparison of the chest deflection of a 90% male, a CPR manikin, and a hybrid III crash test dummy. It is shown that the force-deflection curve of the CPR manikin deviates minimally from that of the 90% male. Thus, the CPR manikin provides an accurate representation of the human torso during drop test experiments.

To perform experiments employing the PSF, 2”x 2” square pieces of film from three separate pressure ranges were cut and placed under the carrying vest, on top of the ceramic armor panel

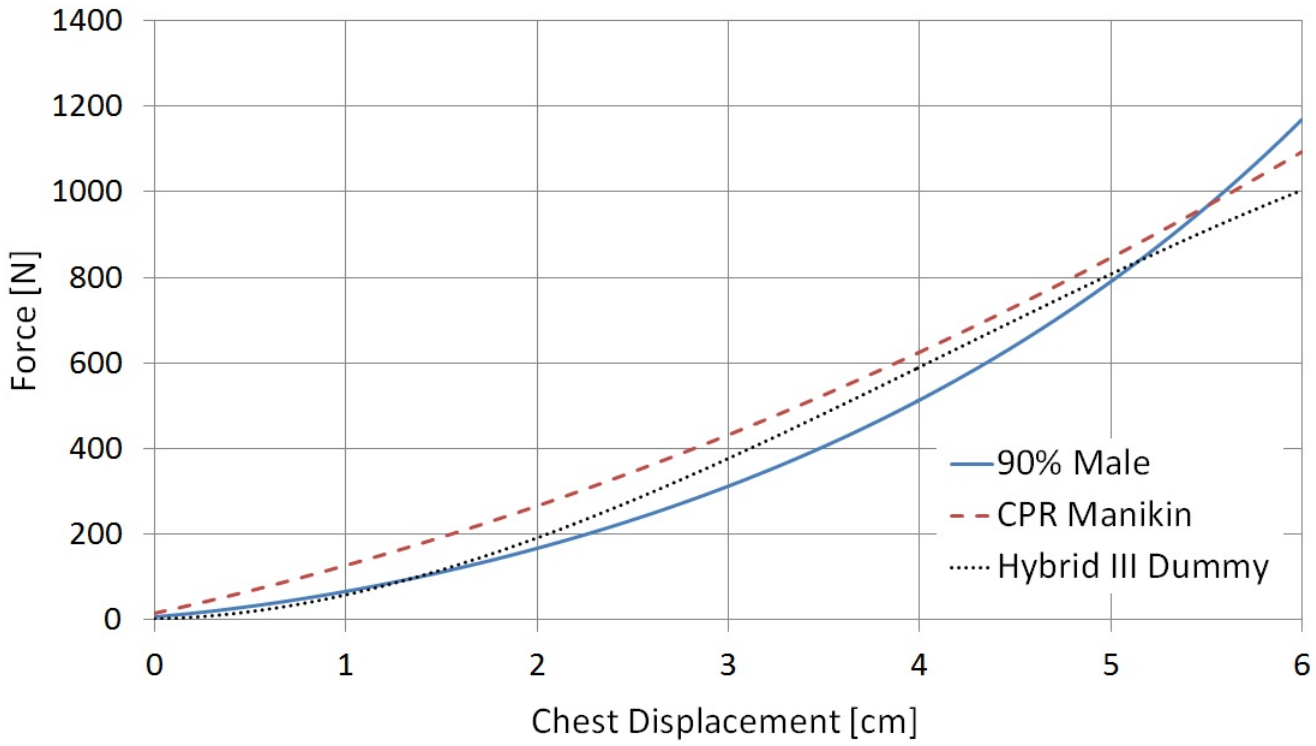

Figure 3.4 Chest deflection for 90% male, CPR manikin, and hybrid III dummy for comparison.

at the location where the impact would take place. The three pressure ranges used for impact testing were: Medium, 1400-7100 psi; high, 7100-18500 psi; and super high, 18500-43500 psi. The PSF was then scanned to acquire a computer image. The computer images were then further processed using a built in image processor in MATLAB to obtain digital contour plots of the PSF for further evaluation. All ceramic body armor panels studied were rated NIJ threat level IV [NIJ (2008)], standalone and measured approximately 10"x 12".

Further detailing of the experimental procedure including details of equipment employed and exact procedures followed for impact experiments may be found in Appendix H.

3.2 Numerical modeling

ANSYS LS-DYNA was employed to numerically model the impacts on the ceramic body armor/CPR manikin system. Figure 3.5 shows the model developed. A linear elastic material with an elastic modulus of 85000 psi was used to represent the human torso. Average material

properties of 50x10^6 psi and 4x10^4 psi were used of the elastic moduli for the alumina plate and Kevlar composite respectively.

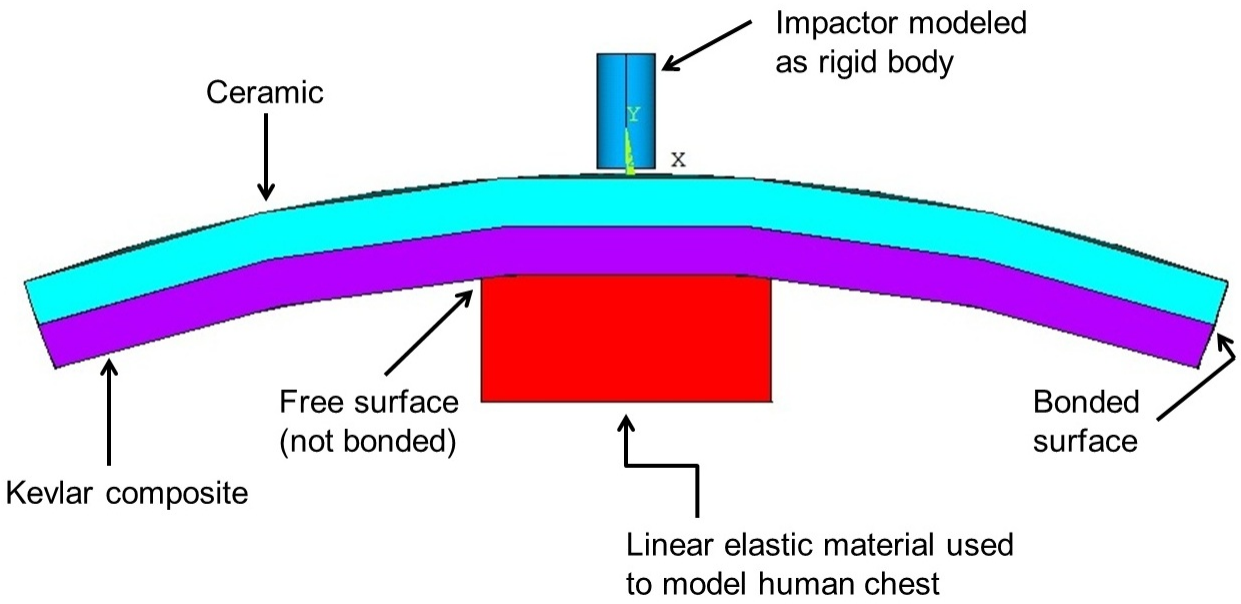

Figure 3.5 Ansys model.

Numerical analysis was performed setting the impactor mass in the numerical model to correspond to the small, medium, and large impactors (5.15-lb, 9.36-lb, 12.52-lb). In the numerical model the impactor resides 0.05-in above the ceramic armor plate and is given an initial velocity corresponding to a particular drop height.

3.3 Analytical modeling

Equation 3.1 was used to analytically model the acceleration of the impactor during an impact event.

$$-m\ddot{y} = Cy^{\alpha}\dot{y}^{\beta} + ky^{\alpha} \qquad \ddot{y}(0) = 0, \quad \dot{y}(0) = v_0 \tag{3.1}$$

In Eq. 3.1, m is the combined mass of the ceramic armor panel and impactor, C is a damping coefficient, k is a spring constant, v_0 is the impact velocity, and $\ddot{y}$, $\dot{y}$, and y are the vertical acceleration, velocity, and displacement of the impactor respectively. The β term captures the

Table 3.2 Constants used in analytical model for each impactor.

Impactor	α	β	$\boldsymbol{C}$ **[N/(m/s)]**	$\boldsymbol{k}$ **[N/m]**
Small	1.27	$\frac{3}{2}$	1.0x10^6	1.75x10^8
Medium	1.20	$\frac{3}{2}$	1.0x10^6	1.03x10^8
Large	1.21	$\frac{3}{2}$	1.0x10^6	1.25x10^8

velocity-dependent effects due to visco-elastic behavior. The α term equals $\frac{3}{2}$ for a completely elastic collision between a flat plate and a sphere (Lieberman et al. (1994) developed equation 3.1 originally to model golf ball impacts). Table 3.2 shows the values of the constants used in equation 3.1 to model each impactor.

3.4 Ballistic experiments

Several ceramic body armor panels with and without initial damaged were subjected to ballistic impacts. Panels were damaged using the small and large impactors dropped from heights between 48" and 96". Damaged panels were x-rayed prior to ballistic testing and marked for crack locations. Ballistic impacts on the damaged panels occurred at differing locations relative to the panels cracks. After ballistics testing, panels were x-rayed again for analysis. An undamaged panel was x-rayed and ballistically tested for comparison. The approximate weight, muzzle velocity, and impact energy of the ballistics test were 130 grains, 720 m/s, and 2180 J respectively. Panels were damaged using drop test setup.

CHAPTER 4. RESULTS AND DISCUSSION

4.1 Impact experiments

Figure 4.1 shows acceleration profiles for impacts onto undamaged ceramic armor panels employing the small, medium, and large impactors respectively.[1] From Fig. 4.1, it is shown that for each impactor the peak value of the acceleration profile increases with an increase in impact energy. Also shown is that the duration of the impact, the time at which the acceleration profile increase from and drops back to zero, decreases with an increase in the impact energy.

Figure 4.2 plots, for the small and large impactors from 12" and 36" drop heights, the force profile of the impacts together with the acceleration profiles multiplied by the impactors mass. It is shown that multiplying the acceleration profile of an impact with the impactors mass recovers the force profile. The small variation present between the two profiles may be attributed to the force transducer not contacting the armor evenly owing to the impactor being flat and the armor panel being curved and that the armor was not always perfectly normal to the impactor.[2]

Figure 4.3(a) plots the peak value of the acceleration profiles for each impactor as a function of impact energy. Figure 4.3(b) plots the trend lines for the data of figure 4.3(a). For all impactors, each impact energy corresponds to a drop height of 6" to 48" by intervals of 6". Ten impacts were performed at each impact energy. Figure 4.3(a) clearly shows that the maximum acceleration of an impact increases with an increase in impact energy. It is shown in Fig. 4.3(b) that the slope of the trend lines are greatest for the small impactor and lowest for the large impactor. It is also shown in Fig. 4.3 that for a given impact energy, the maximum acceleration

[1] All acceleration, velocity, and displacement profiles are that of the impactor unless stated otherwise.

[2] Owing to the direct relationship of the force profile and the acceleration profile (i.e. the force profile may be recovered from the acceleration profile and thus they follow the same trends), henceforth the acceleration profile is used as a comparison for the data.

is greatest for the small impactor and lowest for the large impactor.

Figure 4.4 shows the displacement profiles for the small and large impactors from 12" and 48" drop heights. Zero displacement corresponds to the surface of the manikin's chest with negative displacement corresponding to chest compression. It is shown for both impactors that the displacement increases as the drop height (impact energy) increases and that for a given drop height the displacement is greater for the large impactor than the small impactor. The increase in chest compression at a given impact energy with the large impactor as compared to the small impactor leads to the large impactor producing a lower acceleration profile as compared to the small impactor that is shown in Fig. 4.1 and Fig. 4.2.

The displacement profiles were obtained by integrating the acceleration profiles twice using the impact velocity and setting the displacement of the armor panel to be zero at the start of the impact. The displacement profiles flat line approximately where the acceleration reduces back to zero. Extending the profiles further in time reveals that they increase corresponding to the manikin chest expanding to its original position.

For reference, Fig. 4.5 shows an x-ray image of a damaged armor panel and an undamaged armor panel. Through thickness cracks radiate out from the point of impact that caused that damage to the edges of the panel. Cracks are only present in the ceramic material of the armor.

Figure 4.6 shows a comparison of acceleration profiles for an undamaged armor panel and a damaged armor panel for the small and large impactors from two separate drop heights of 12" and 36". A clear distinction is present in the profiles. The undamaged panel produces an acceleration profile with a single peak while the damaged panel produces an acceleration profile with two distinct peaks. Also shown is that the maximum acceleration for a given impactor at a given drop height is greater on the undamaged panel than the damaged panel. The duration of the impacts on the damaged panels is greater than that of the undamaged panels leading to the lower maximum acceleration seen on the damaged panels.

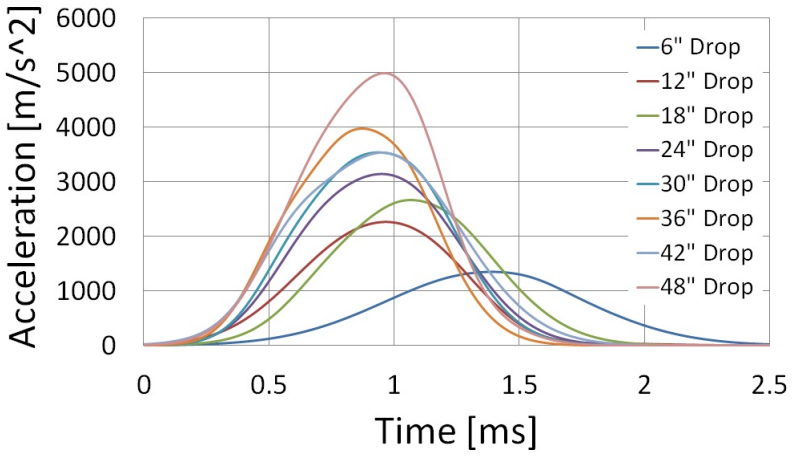

(a) Accelerations for small impactor.

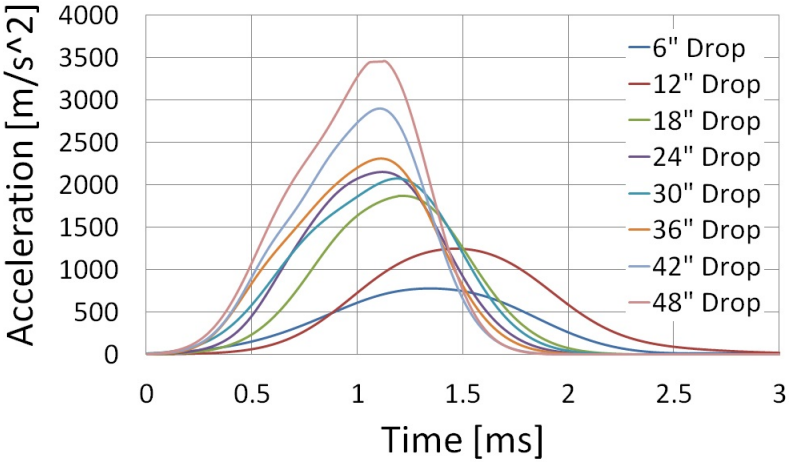

(b) Accelerations for medium impactor.

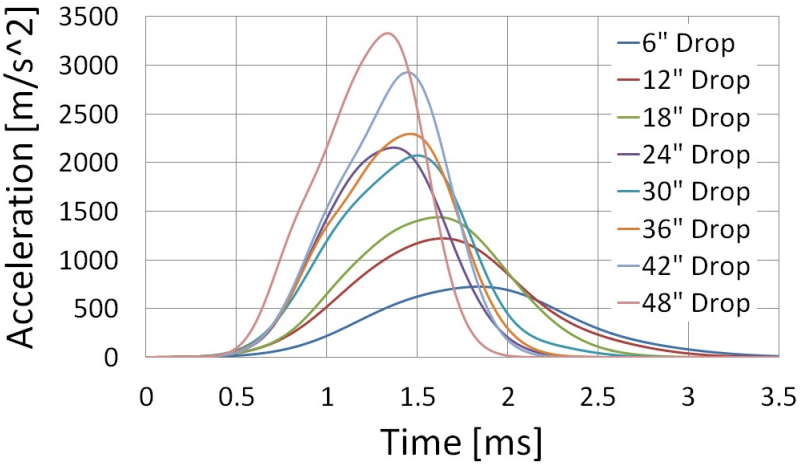

(c) Accelerations for large impactor.

Figure 4.1 Acceleration data for each impactor at drop heights ranging from 6” to 48”.

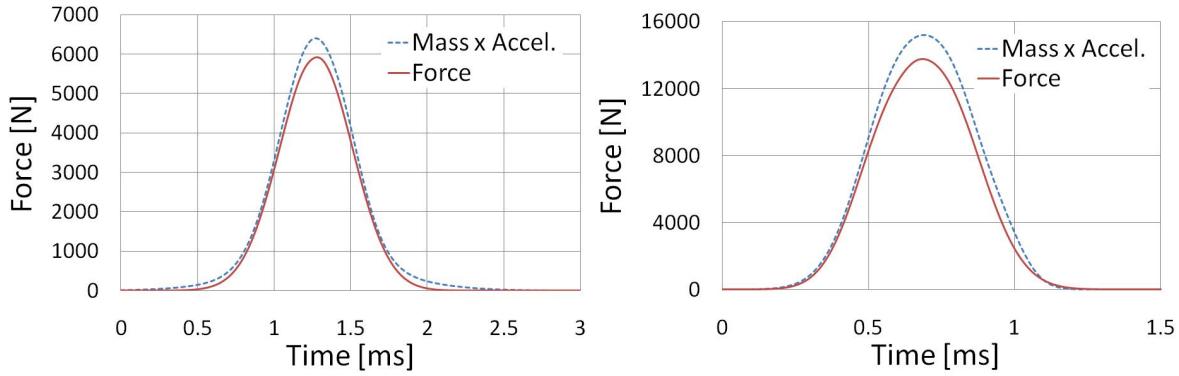

(a) Small impactor, 12” drop.

(b) Small impactor, 36” drop.

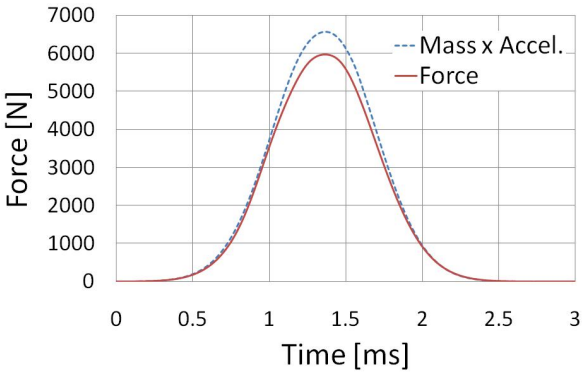

(c) Large impactor, 12” drop.

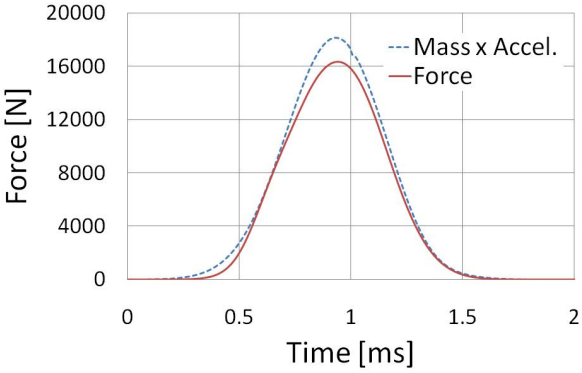

(d) Large impactor, 36” drop

Figure 4.2 Comparison of data from force transducer and data from accelerometer multiplied by the impactor mass.

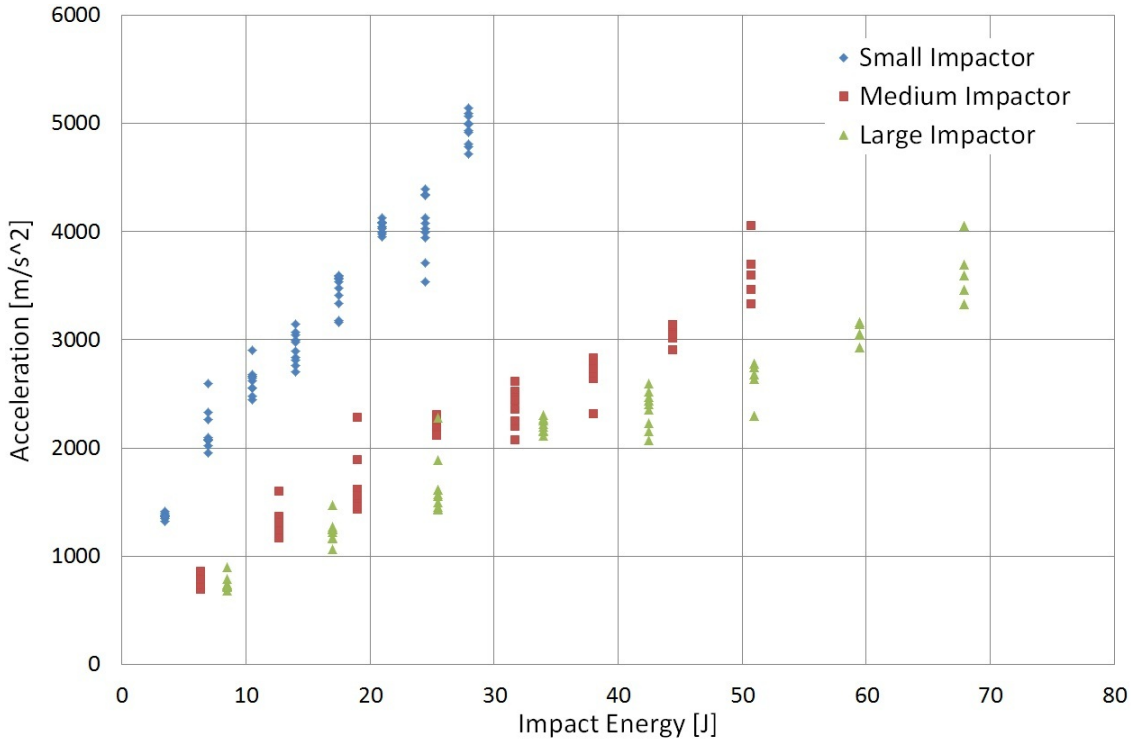

(a) Peak experimental accelerations.

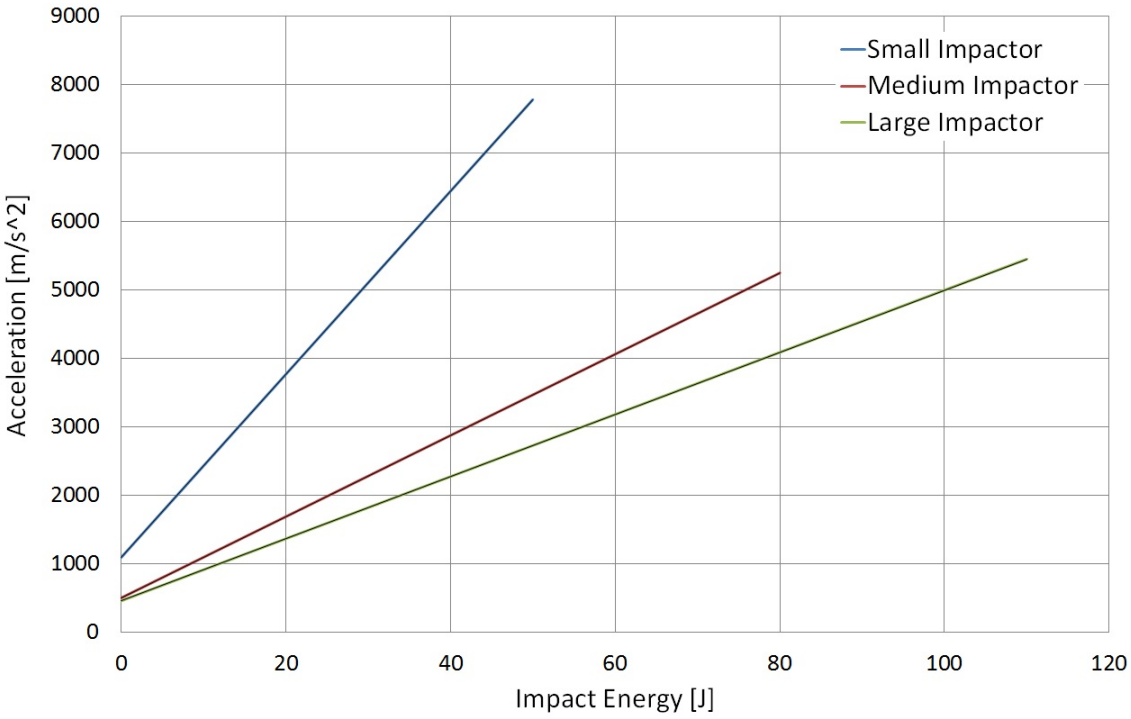

(b) Trend lines for peak experimental accelerations.

Figure 4.3 Peak acceleration values and their trend lines for experimental data.

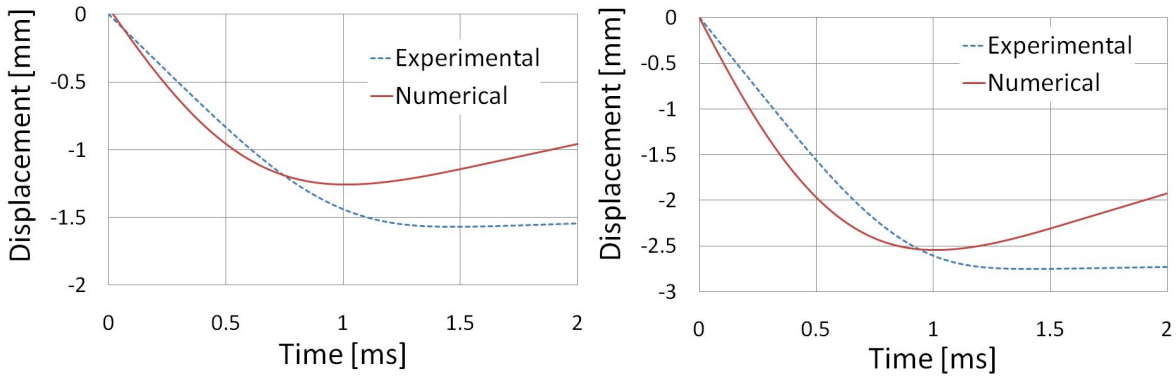

(a) Small impactor, 12” drop.

(b) Small impactor, 48” drop.

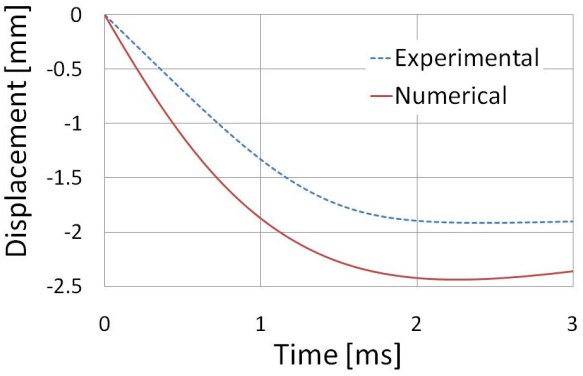

(c) Large impactor, 12” drop.

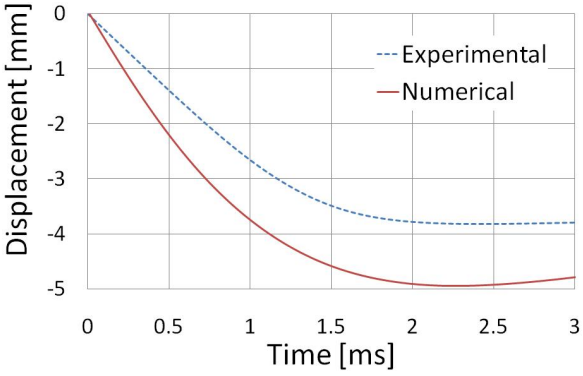

(d) Large impactor, 48” drop

Figure 4.4 Impactor displacement profiles for selected impactors and drop heights.

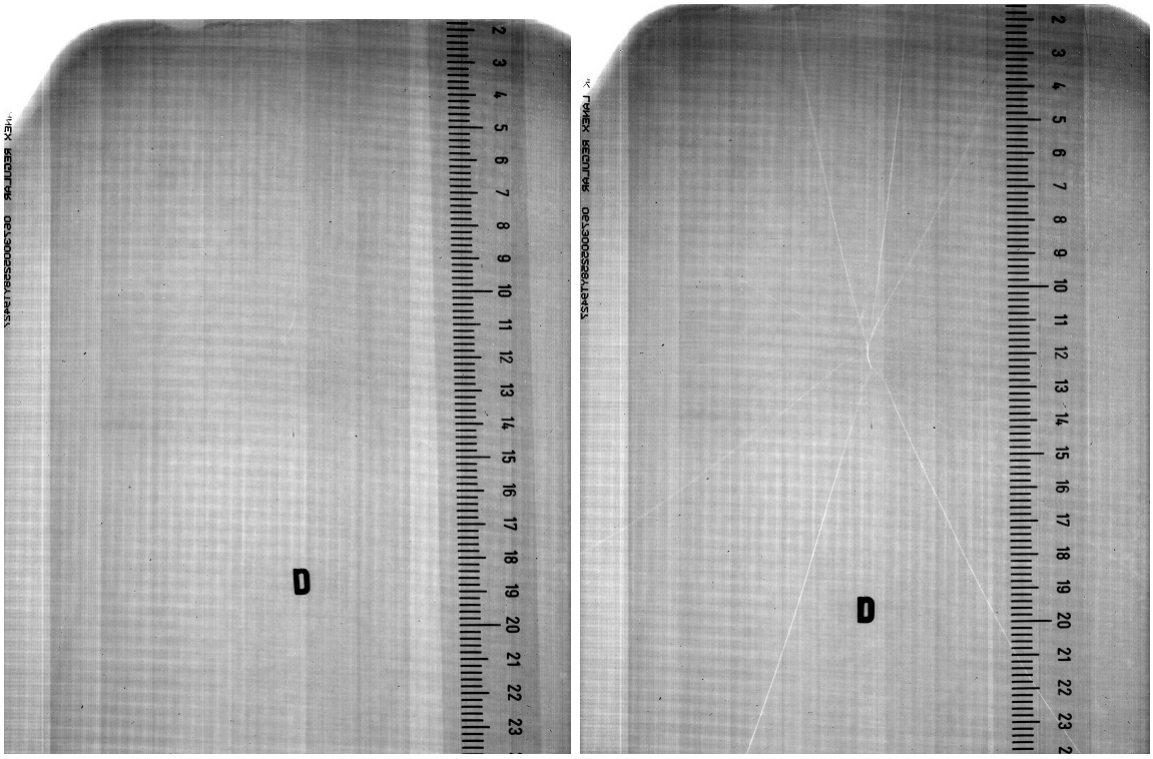

(a) Undamaged armor panel.

(b) Damaged armor panel.

Figure 4.5 Comparison of an undamaged and damaged ceramic armor panel. Bright lines in panel on the right indicate through thickness cracks in the ceramic. Damaged in this panel was caused by an impact of approximately 68J.

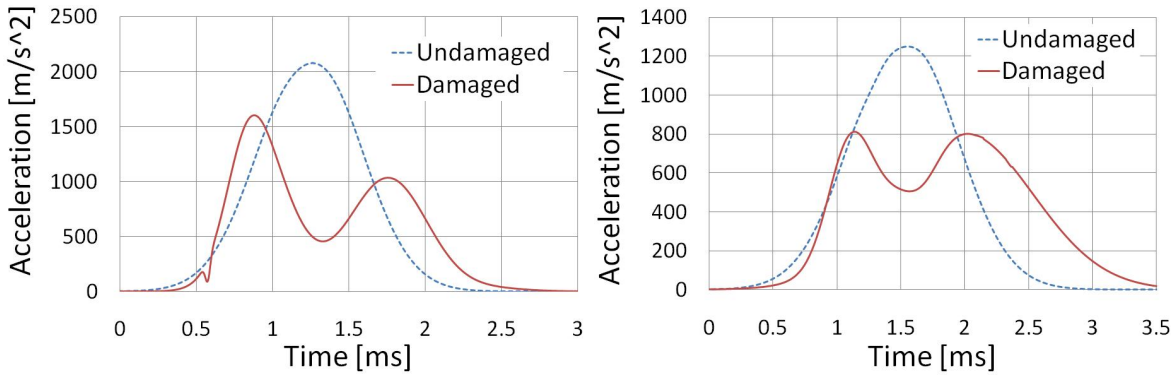

(a) Small impactor, 12” drop.

(b) Small impactor, 36” drop.

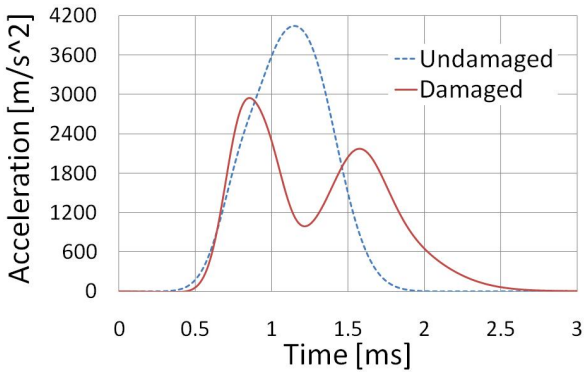

(c) Large impactor, 12” drop.

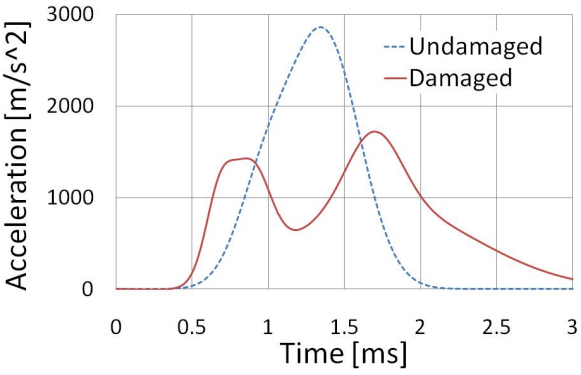

(d) Large impactor, 36” drop

Figure 4.6 Comparison of accelerations from impacts on undamaged and damaged armor panels. Dashed curves: acceleration profile from undamaged panel. Solid curves: acceleration profile from damaged panel.

4.2 PSF experiments

Figure 4.7(a) shows the amount of indication that appears on the PSF for a given saturation level.[1] Figure 4.7(b) is a digital contour image of the indication levels of Fig. 4.7(a). The indication scale in Fig. 4.7(a) was converted to a gray scale image and then a built in function in MATLAB was used to evaluate the pixel values of the gray scale image and convert them to a contour plot.[2] Table 4.1 lists the pressure values corresponding to a given saturation level for the medium, high, and super high PSF.[3]

Figures 4.8 – 4.15 are PSF with indications and their corresponding digitized images for impacts employing the small and large impactors for drop heights of 12", 24", 36", and 48". Indications on the medium, high, and super high PSF are shown for each impact. Table 4.2 lists pressure values obtained using the maximum force applied during a given impact as measured by the force transducer and the force transducer area. Table 4.3 lists the pressure values obtained by evaluating the digitized PSF images using Fig. 4.7 and Table 4.1.

Table 4.1 Pressure values corresponding to PSF saturation levels.

	Pressure values per saturation level [psi]		
Saturation level	**Medium PSF**	**High PSF**	**Super High PSF**
0.1	Below film range	Below film range	Below film range
0.2	1400	7100	Below film range
0.3	2100	8500	Below film range
0.4	2450	10600	18500
0.5	2900	12800	20100
0.6	3550	15000	23000
0.7	4000	16800	25000
0.8	4500	18500	32000
0.9	5000	20000	435000
1.0	5500	Over saturated	Over saturated
1.1	6200	Over saturated	Over saturated
1.2	6800	Over saturated	Over saturated
1.3	7900	Over saturated	Over saturated
1.4	Over saturated	Over saturated	Over saturated
1.5	Over saturated	Over saturated	Over saturated

[1] Information provided with PSF from manufacturer.
[2] Throughout this section, any image referred to as digitized underwent this same process.
[3] Data provided with PSF from manufacturer.

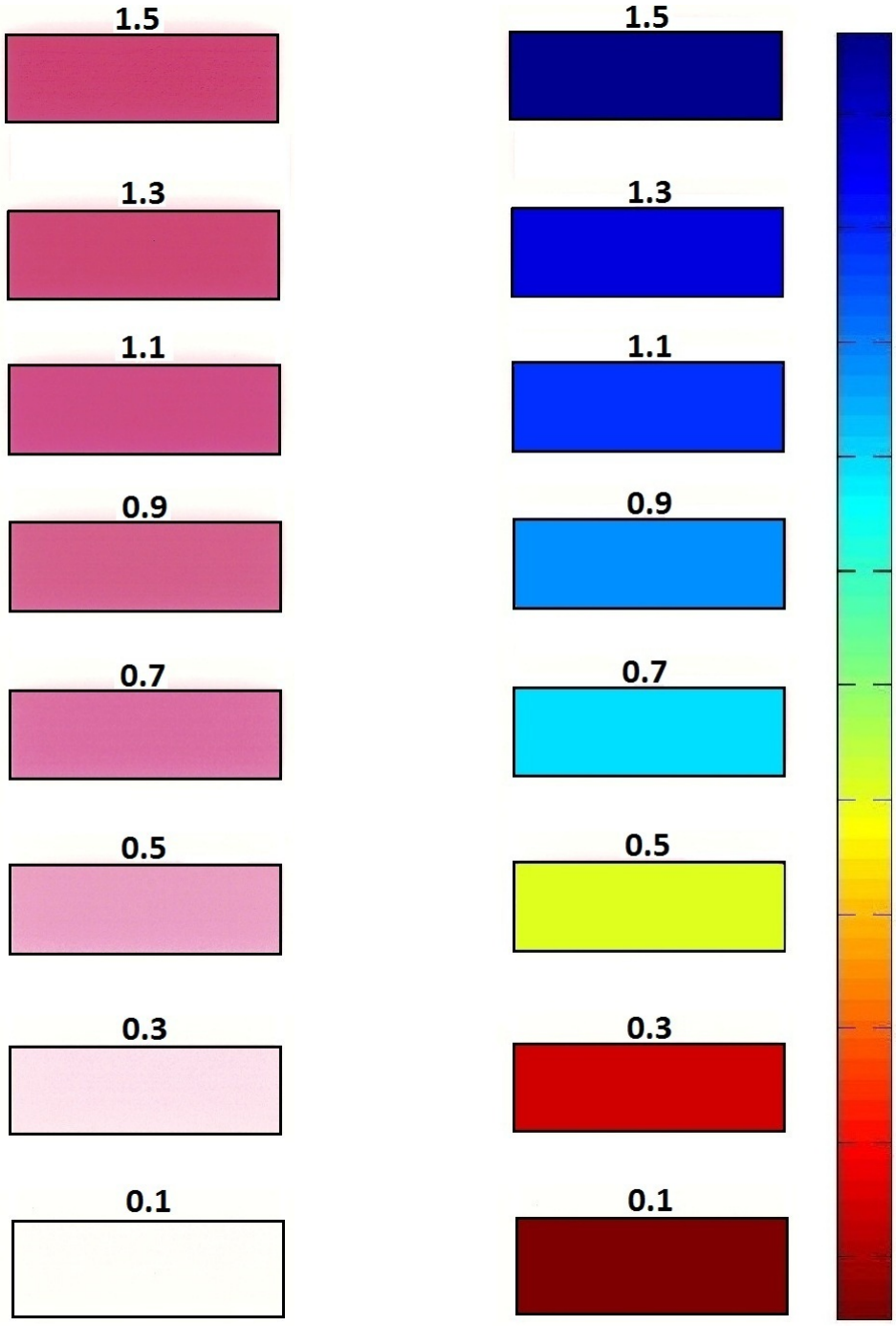

(a) PSF indication levels.

(b) Digitized PSF indication levels.

Figure 4.7 Saturation scale for PSF. Left: raw PSF indications. Right: digitized indications.

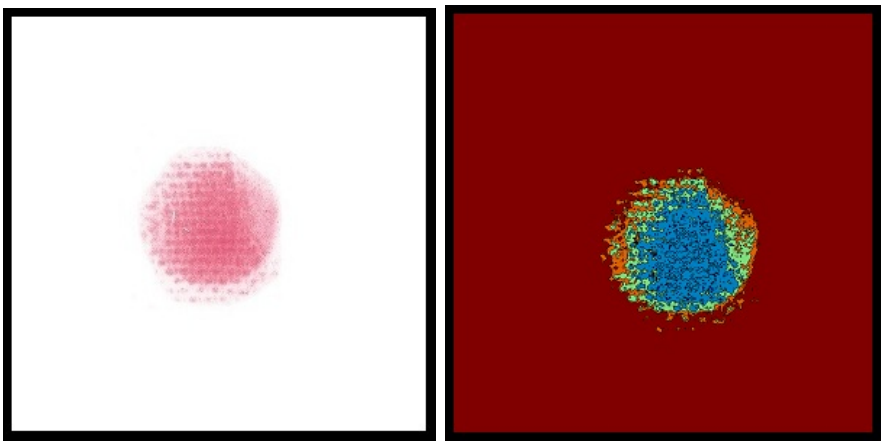

(a) Medium PSF (b) Medium PSF: digitized

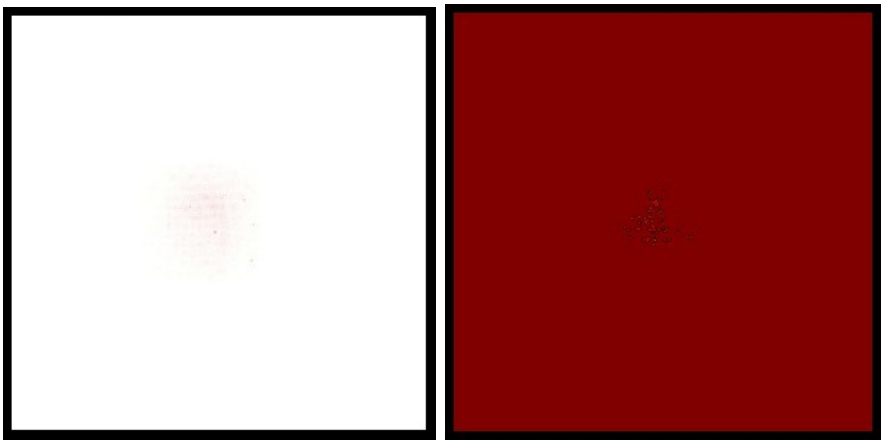

(c) High PSF (d) High PSF: digitized

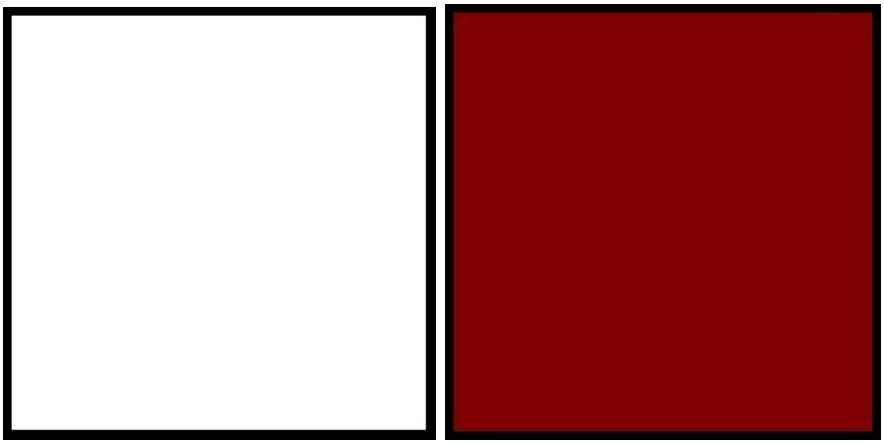

(e) Super High PSF (f) Super High PSF: digitized

Figure 4.8 Pressure film with indication and corresponding digitized image from an impact using small impactor from 12".

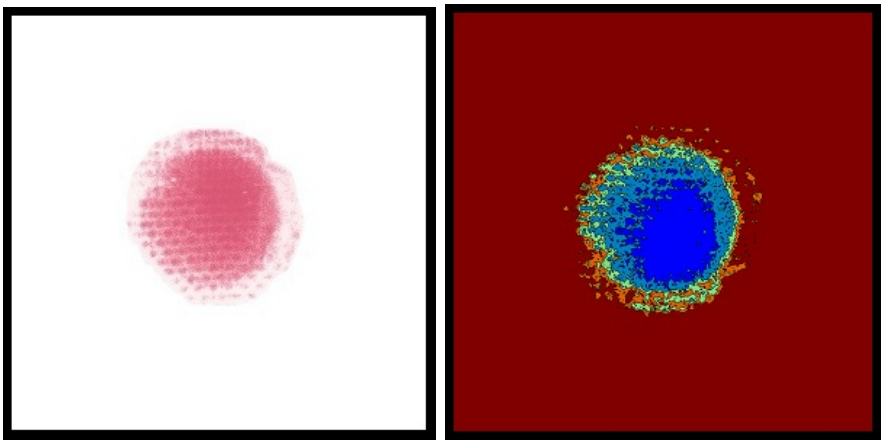

(a) Medium PSF (b) Medium PSF: digitized

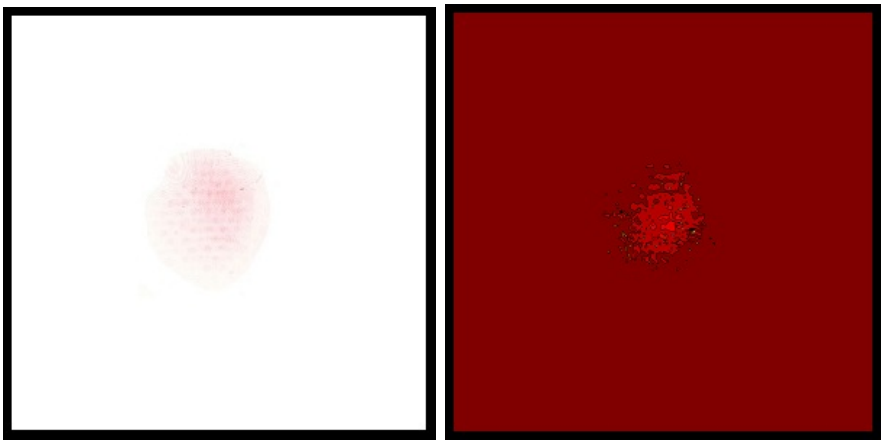

(c) High PSF (d) High PSF: digitized

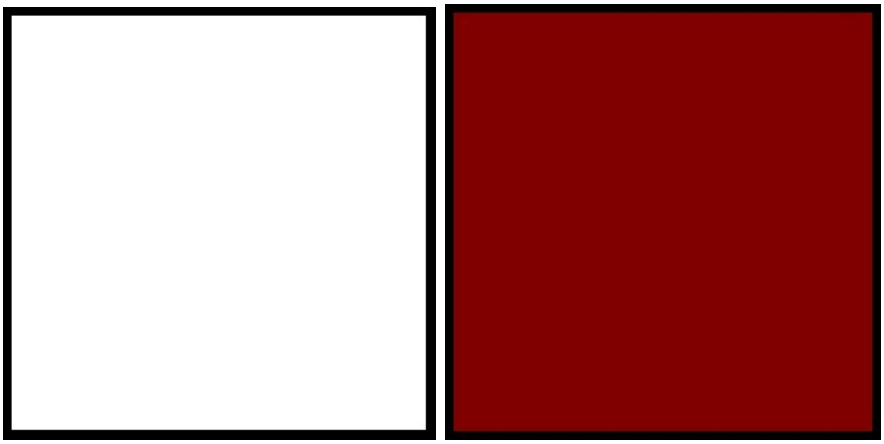

(e) Super High PSF (f) Super High PSF: digitized

Figure 4.9 Pressure film with indication and corresponding digitized image from an impact using small impactor from 24".

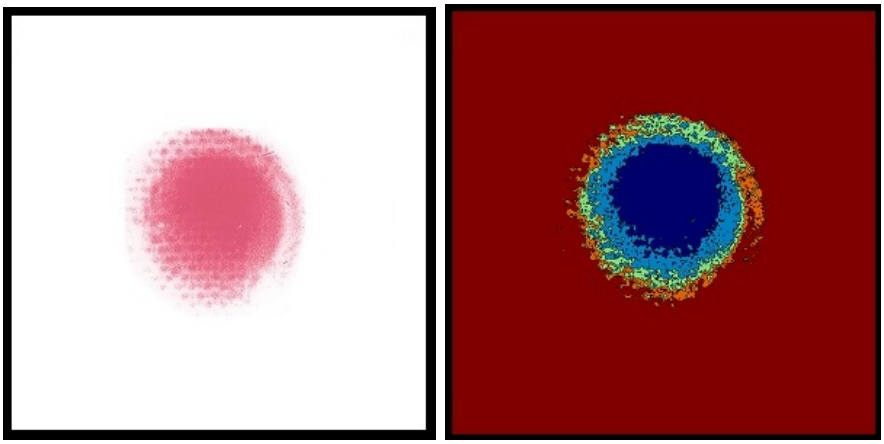

(a) Medium PSF (b) Medium PSF: digitized

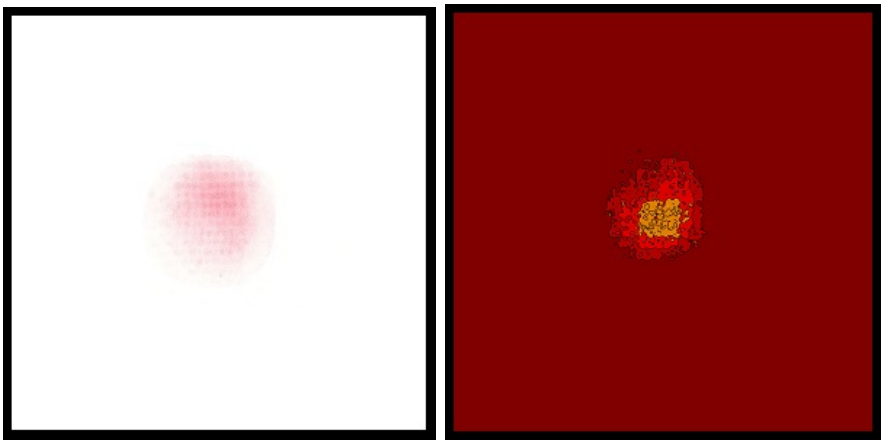

(c) High PSF (d) High PSF: digitized

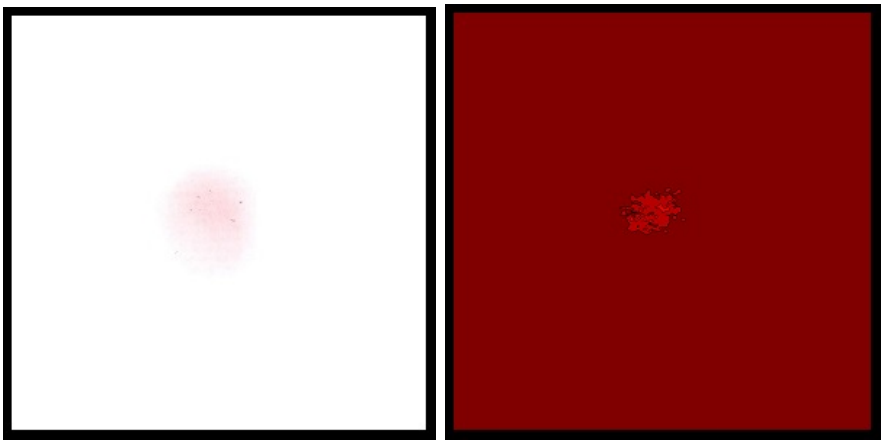

(e) Super High PSF (f) Super High PSF: digitized

Figure 4.10 Pressure film with indication and corresponding digitized image from an impact using small impactor from 36".

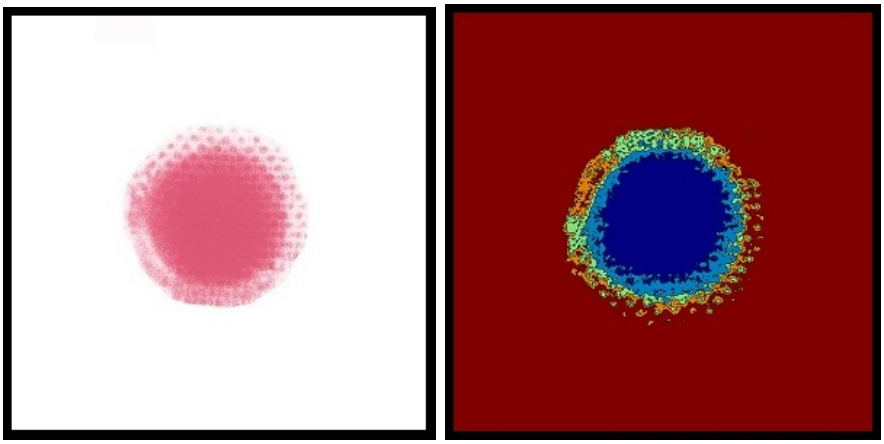

(a) Medium PSF (b) Medium PSF: digitized

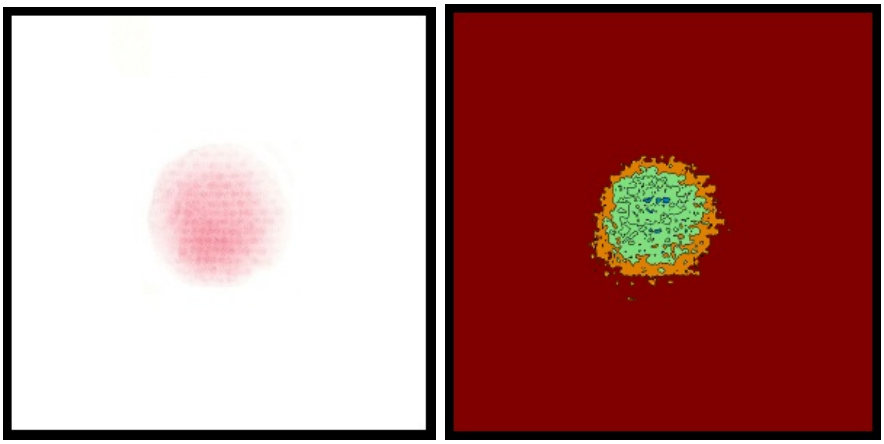

(c) High PSF (d) High PSF: digitized

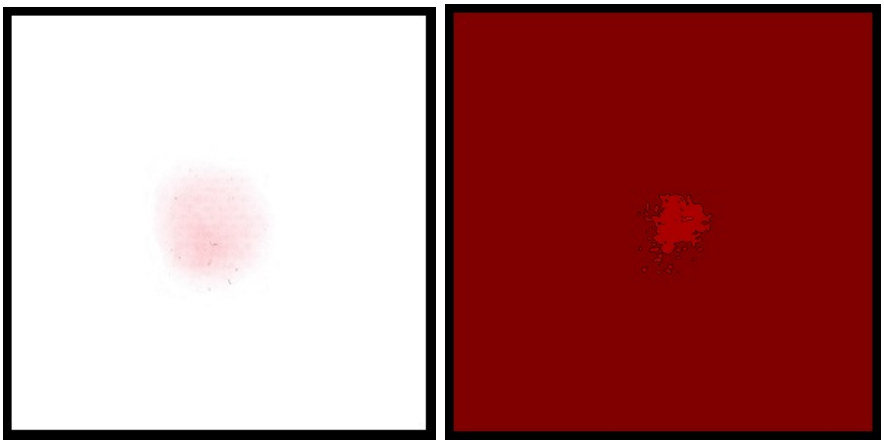

(e) Super High PSF (f) Super High PSF: digitized

Figure 4.11 Pressure film with indication and corresponding digitized image from an impact using small impactor from 48".

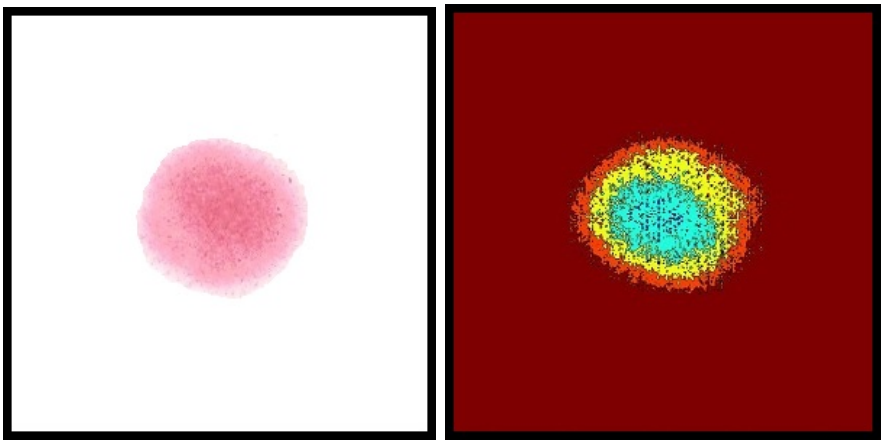

(a) Medium PSF (b) Medium PSF: digitized

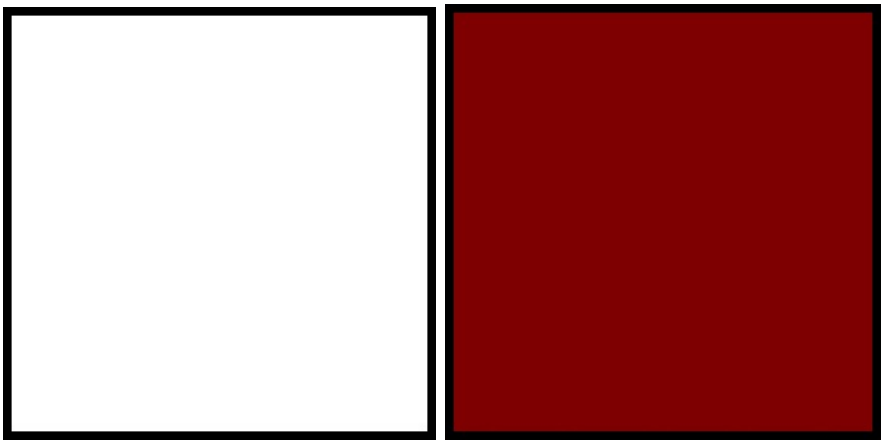

(c) High PSF (d) High PSF: digitized

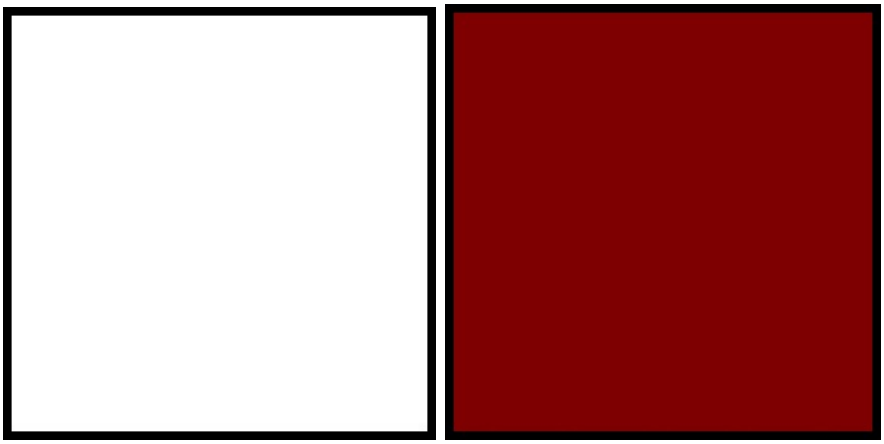

(e) Super High PSF (f) Super High PSF: digitized

Figure 4.12 Pressure film with indication and corresponding digitized image from an impact using large impactor from 12".

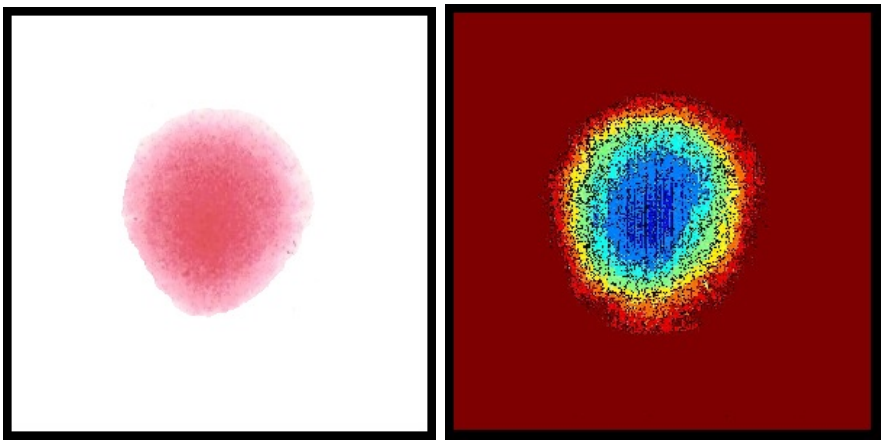

(a) Medium PSF (b) Medium PSF: digitized

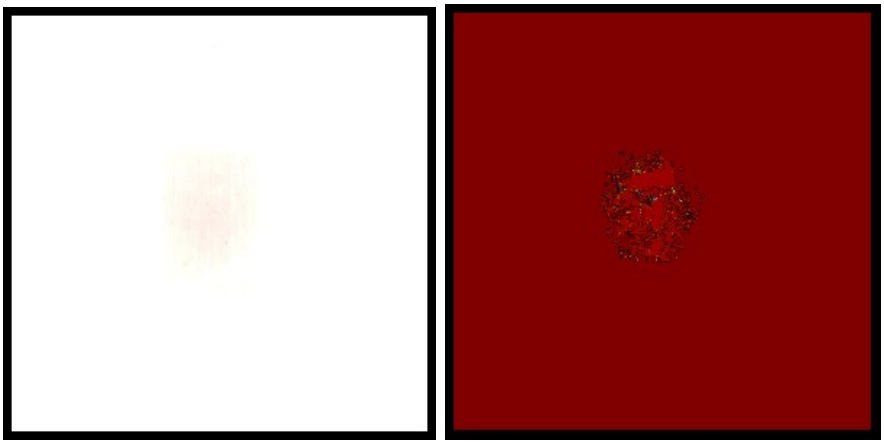

(c) High PSF (d) High PSF: digitized

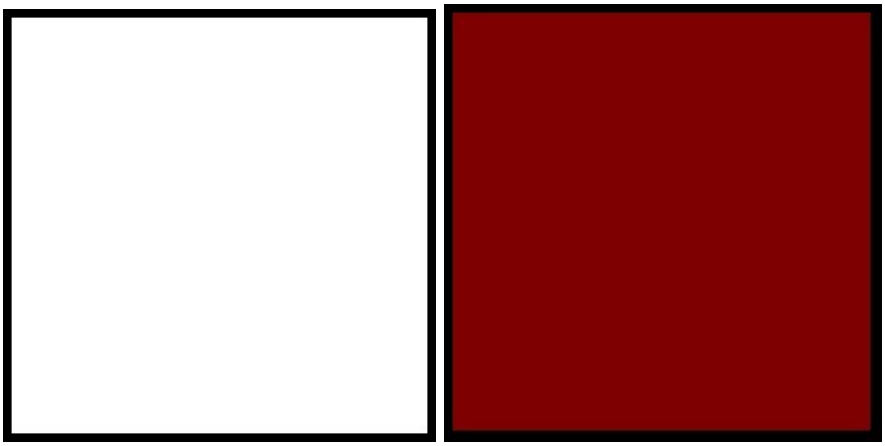

(e) Super High PSF (f) Super High PSF: digitized

Figure 4.13 Pressure film with indication and corresponding digitized image from an impact using large impactor from 24".

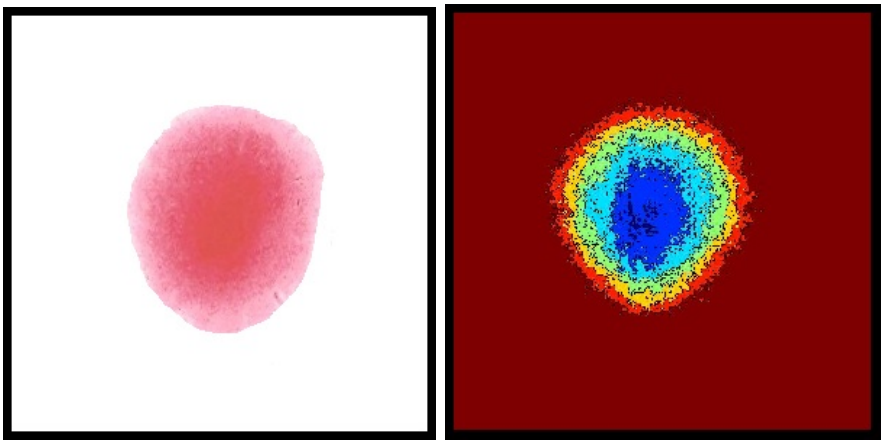

(a) Medium PSF (b) Medium PSF: digitized

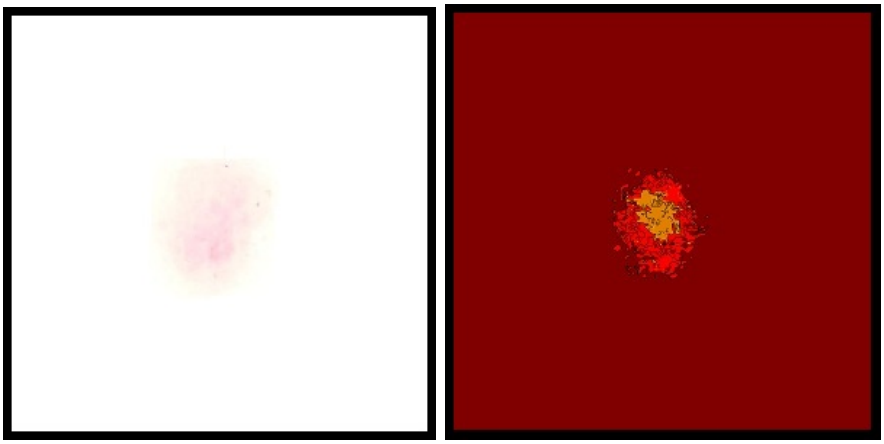

(c) High PSF (d) High PSF: digitized

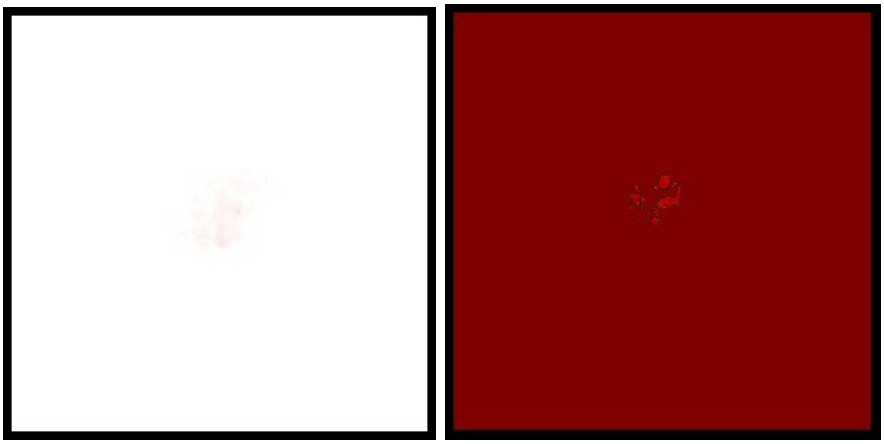

(e) Super High PSF (f) Super High PSF: digitized

Figure 4.14 Pressure film with indication and corresponding digitized image from an impact using large impactor from 36".

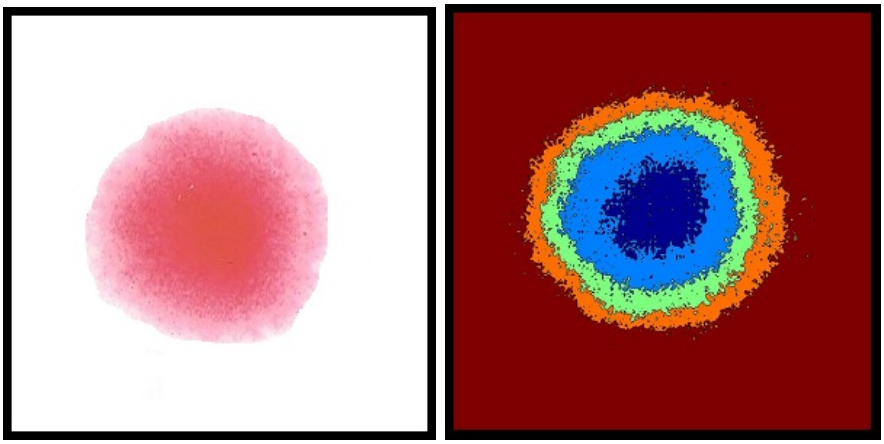

(a) Medium PSF (b) Medium PSF: digitized

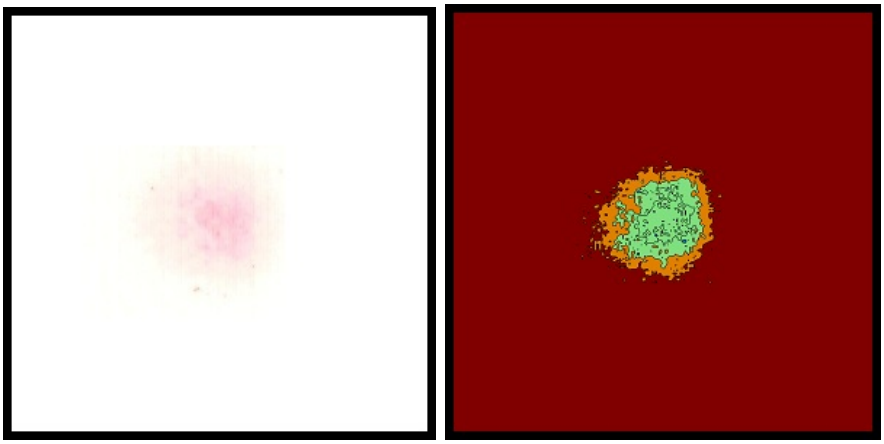

(c) High PSF (d) High PSF: digitized

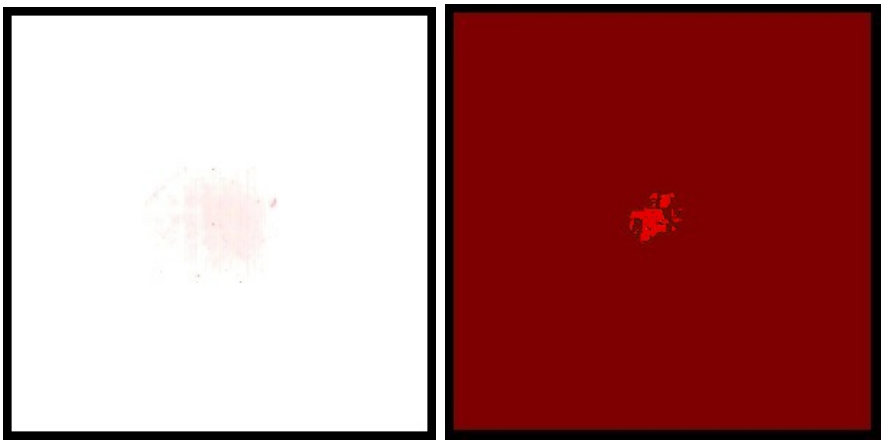

(e) Super High PSF (f) Super High PSF: digitized

Figure 4.15 Pressure film with indication and corresponding digitized image from an impact using large impactor from 48".

Table 4.2 Pressure values calculated from force transducer data and area.

Impactor	**Drop Height [in]**	**Impact Energy [J]**	**Pressure [psi]**
Small	12	6.00	4150
	24	14.0	6200
	36	21.0	8600
	48	27.9	11200
Large	12	17.0	3800
	24	34.0	6000
	36	50.9	7400
	48	67.9	9000

Table 4.3 Comparison of pressure calculated from force transducer and from indications on PSF.

		PSF indications (digitized)					
		Medium		**High**		**Super High**	
Impactor	**Drop Ht. [in]**	**Sat. Lv.**	**Press. [psi]**	**Sat. Lv.**	**Press. [psi]**	**Sat. Lv.**	**Press. [psi]**
Small	12	0.7	4000	0.1	N/A	No ind.	N/A
	24	1.2	6800	0.2	7100	No ind.	N/A
	36	1.5	Over Sat.	0.4	10600	0.2	N/A
	48	1.5	Over Sat.	0.6	15000	0.3	N/A
Large	12	0.7	4000	No ind.	N/A	No ind.	N/A
	24	1.1	6200	0.1	N/A	No ind.	N/A
	36	1.5	Over Sat.	0.3	8500	0.1	N/A
	48	1.5	Over Sat.	0.4	10600	0.3	N/A

Comparing both the PSF indications and digitized images for the small impactor in Fig. 4.8 – 4.11 it is shown that as the impact energy increases, the indication level on the PSF increases. As the impact energy increases the force of the impact increases and as expected the pressure applied to the armor increase. The same trend follows for the large impactor. For both impactors at the low impact energies little to no indication appears on the high and super high PSF while at the high impact energies the medium PSF becomes over saturated and indications arise on the high and super high PSF.

Comparing the indications produced by the small and large impactors from a 12" drop height (Fig. 4.8 and Fig. 4.12) shows that the indication level on the PSF from the impact using the small impactor is greater than that of the indication level on the PSF from the impact using the large impactor. This trend is visible in the PSF for each drop height which follows with the experimental acceleration data showing a larger acceleration for the small impactor than the large impactor at the same drop height (Fig. 4.3).

Table 4.3 shows the trend of the small impactor producing a higher pressure indication than the large impactor at a given drop height. Comparing the pressure values in Tables 4.2 and 4.3 shows that the pressure values obtained from the indications on the PSF align well with those obtained from the experimental force data. The indications obtained from the PSF are minimally higher than those from the force data.

4.3 Numerical modeling

Figure 4.16 plots acceleration profiles obtained from the numerical model together with experimental profiles for the small and large impactor at drop heights of 6" and 48" (see Appendices A-C for a comparison of all experimental and numerical acceleration profiles for each impactor at each drop height). Figure 4.17 shows a comparison of the experimental and numerical acceleration profiles for the large impactor at all impact energies (see Appendices A and B for similar figures of the small and medium impactor). Figure 4.18 shows a comparison of selected displacement profiles from the numerical model and experiemental data. Figure 4.19 shows the maximum acceleration values obtained from the numerical model along with the trend lines of the maximum acceleration values obtained from the experimental data.

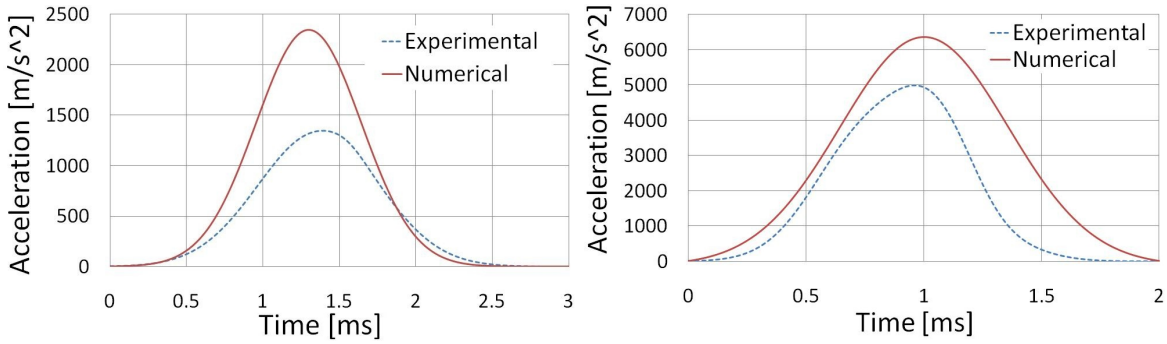

(a) Small impactor: 6” drop

(b) Small impactor: 48” drop

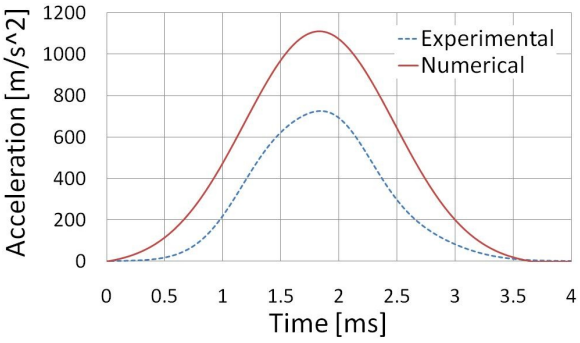

(c) Large impactor: 6” drop

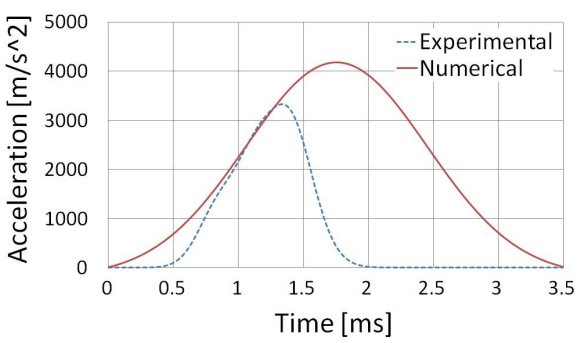

(d) Large impactor: 48” drop

Figure 4.16 Comparison of accelerations for numerical model and experimental data. Dashed curves: acceleration profiles from experimental data. Solid curves: acceleration profiles from numerical data.

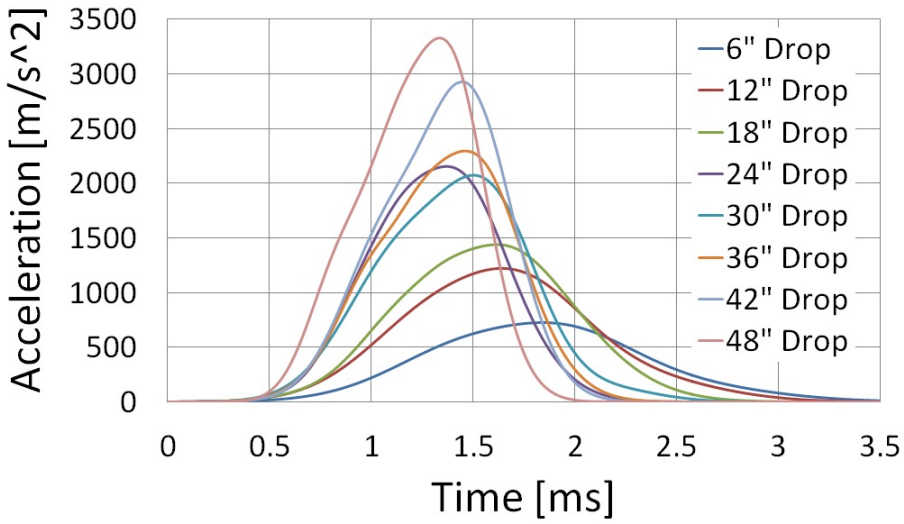

(a) Experimental acceleration profiles.

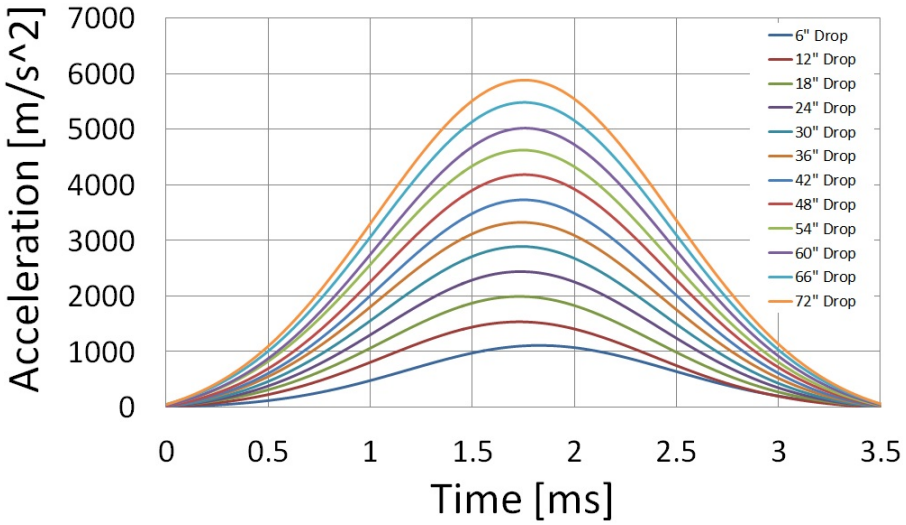

(b) Numerical acceleration profiles.

Figure 4.17 Comparison of experimental and numerical acceleration profiles for the large impactor at all impact energies.

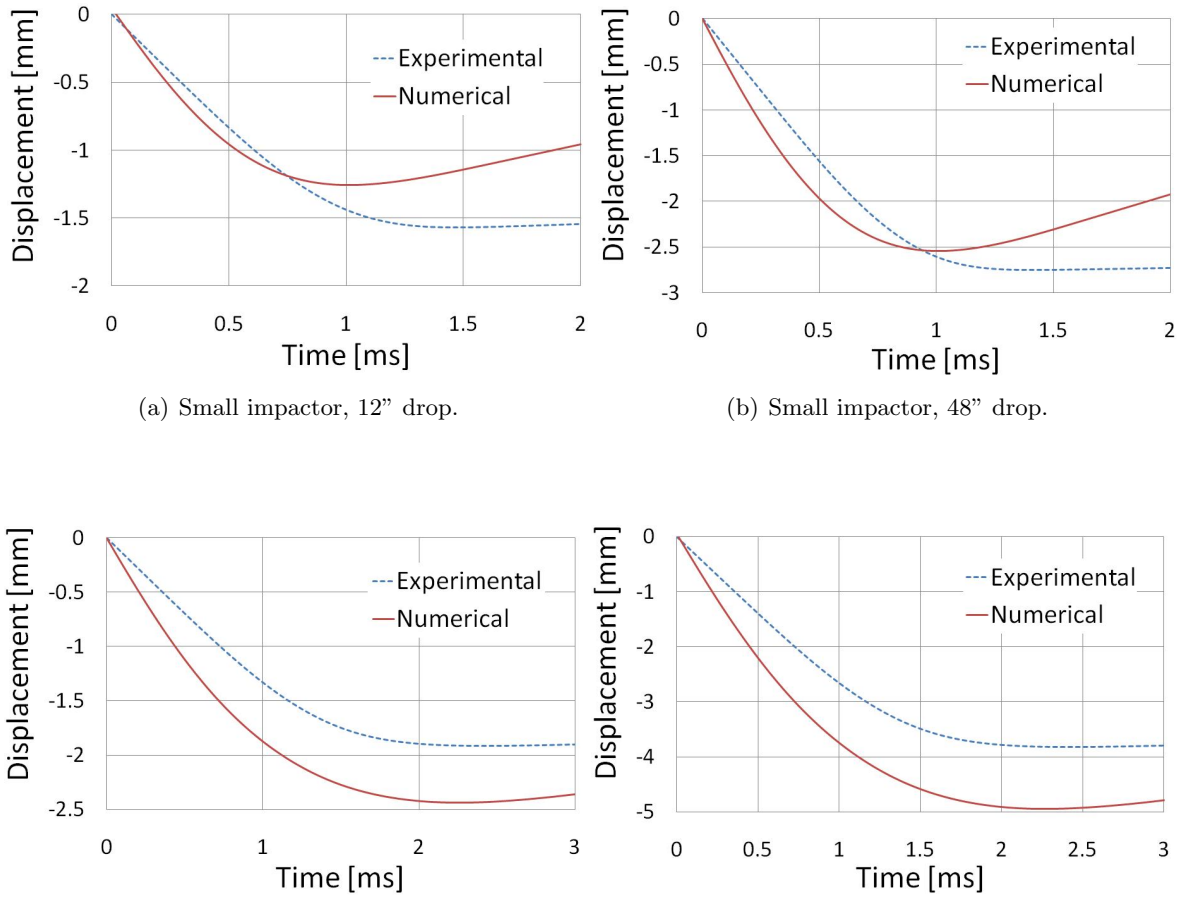

(a) Small impactor, 12” drop.

(b) Small impactor, 48” drop.

(c) Large impactor, 12” drop.

(d) Large impactor, 48” drop

Figure 4.18 Comparison of numerical and experimental impactor displacement profiles for selected impactors and drop heights. Dashed curves: displacement profiles from experimental data. Solid curves: displacement profiles from numerical data.

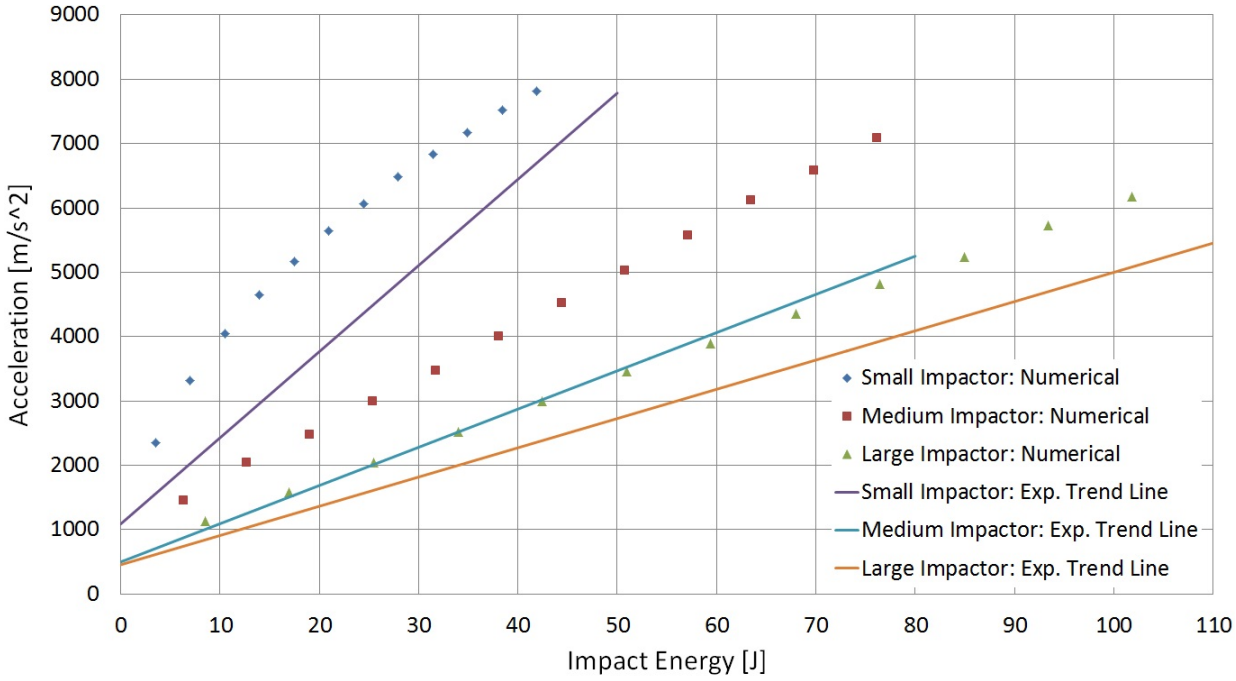

Figure 4.19 Peak acceleration values from numerical models compared with trend lines of peak accelerations from experimental data.

From Fig. 4.16 it is seen that the numerical model captures the general trends of the acceleration profiles for the experimental data. As shown in Fig. 4.17, while the time duration of the impacts for the experimental tests decreases as the impact energy increases, the time duration of the impacts for the numerical model stays the same for all impact energies, this follows for each impactor. This may be attributed to the absence of any nonlinearity or visco-elastic behavior in the numerical model as the manikin chest was modeled as a linear elastic material.

From Fig. 4.18 also shows, by comparison of the numerical and experimental displacement profiles, that the numerical model captures the same trends present in the experimental data. Maximum dispacement values are larger for the large impactor than for the small impactor from a given drop height and maximum displacement values increase with an increase in the impact energy of a given impactor. Both are trends that are present in the experimental data.

From Fig. 4.19, the maximum acceleration values obtained from the numerical model are

greater than those of the experimental data for each impactor at every impact energy. Similar to the experimental impacts, in the numerical model the small impactor produces the largest accelerations with shorter impact durations per a given impact energy while the large impactor produces the smallest accelerations with the longest impact durations. Table 4.4 lists the slopes of the trend lines for both the numerical model and experimental data and there percent difference while Table 4.5 lists the maximum accelerations for both the numerical model and experimental data and their percent difference. The numerical model of the small impactor has the highest percent difference for the maximum acceleration values at approximately 50% while the numerical model of the large impactor has an average percent difference of approximately 30%. The material properties used in the numerical model have a strong influence on both the maximum acceleration and the time duration of the impact. Average material properties were used for the numerical model and the difference between the values used and the values for the ceramic armor employed in experimental testing may have contributed to the error present between the numerical model and the experimental data.

Table 4.4 Comparison of trend line slopes of peak accelerations for numerical and experimental data.

	Slopes of peak acceleration trend lines		
Impactor	**Experimental**	**Numerical**	**% Difference**
Small	133.91	173.04	29.2
Medium	59.394	80.685	35.8
Large	45.442	53.964	18.8

Table 4.5 Comparison of peak acceleration values for numerical and experimental data.

		Peak acceleration values $[\frac{m}{s^2}]$		
Impactor	**Drop Height [in]**	**Exp. (Avg.)**	**Numerical**	**% Difference**
Small	6	1371	2346	71
	12	2157	3310	54
	18	2621	4047	54
	24	2925	4649	59
	30	3440	5166	50
	36	4041	5642	40
	42	4050	6057	50
	48	4947	6480	31
Medium	6	774	1449	87
	12	1286	2041	59
	18	1637	2478	51
	24	2221	2855	29
	30	2380	3162	33
	36	2634	3448	31
	42	3044	3706	22
	48	3590	3956	10
Large	6	751	1130	51
	12	1328	1585	19
	18	1637	2045	25
	24	2221	2525	14
	30	2369	3001	27
	36	2628	3455	31
	42	3069	3887	27
	48	3626	4355	20

4.4 Analytical modeling

Figure 4.20 shows a comparison of acceleration profiles from experimental impacts and the analytical model for the small and large impactor at drop heights of 6" and 48" (see Appendices D-F for a comparison of all experimental and analytical accelerations for each impactor at each drop height). For each impactor, through a range of drop heights, the analytical model captures the general trends of the acceleration profiles. The analytical model adheres to the same time scale and approximates the maximum acceleration of the experimental data with a minor error. The errors between the analytical model and the experimental data may be attributed to the

complexity of the system being model.

Owing to the armor plate not being directly connected to the chest, the impactor hits the armor plate and proceeds to compress the manikin, during which small lateral movements of the armor occurs, along with the nonlinearity present in the manikin, these produce an event that does not directly compare to what a typical impact the analytical model is capable of capturing [Lieberman et al. (1994)]. The error present in the prediction of the maximum acceleration is minimal enough that analytical acceleration may be used to obtain an impact force that would in turn be able to predict an approximate pressure value for a given impact.

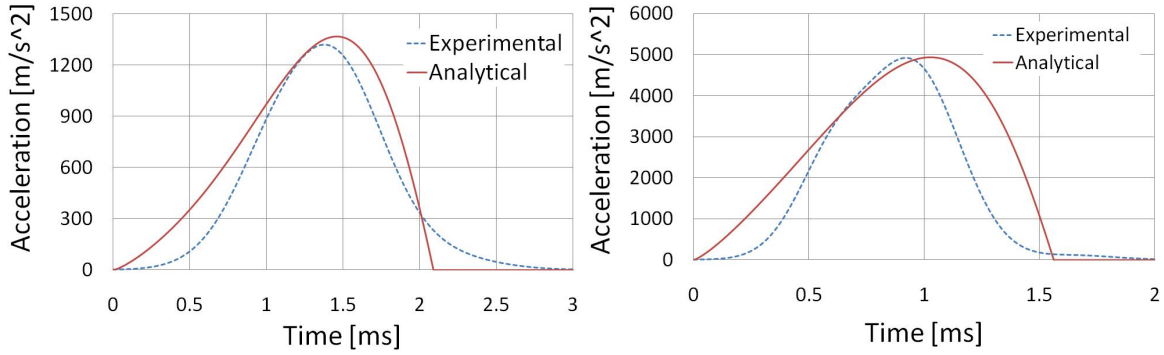

(a) Small impactor: 6” drop

(b) Small impactor: 48” drop

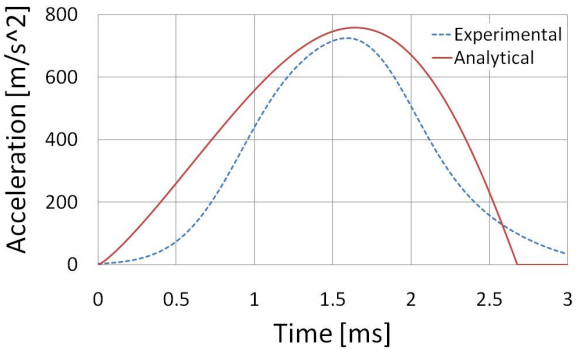

(c) Large impactor: 6” drop

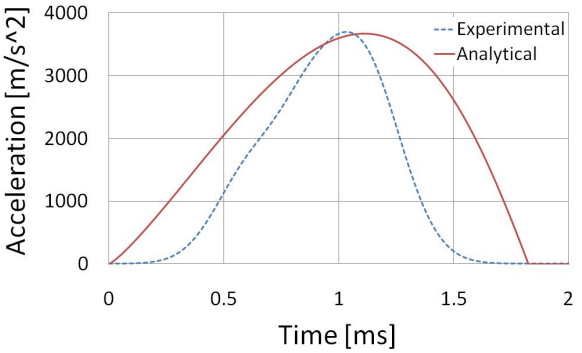

(d) Large impactor: 48” drop

Figure 4.20 Comparison of accelerations for analytical model and experimental data.Dashed curves: acceleration profiles from experimental data. Solid curves: acceleration profiles from numerical data.

4.5 Ballistic experiments

Figures 4.22(a) – 4.22(d) are x-ray images of a damaged ceramic armor panel (henceforth referred to as panel B) prior to and post-ballistics impact. Figure 4.22(a) shows cracks induced in ceramic portion of armor by drop tests. Figure 4.22(b) is the same image with initial damaged in the ceramic marked, the point where the crack lines meet was the location where the impact that induced the damaged occurred. Figure 4.22(c) is an x-ray image of panel B post-ballistics impact and Fig. 4.22(d) is the same image with the location of the initial cracks marked for comparison. Figures 4.21(a) and 4.21(b) are x-ray images of an initially undamaged armor panel prior to and post-ballistics testing. Sets of x-ray images for other initially damaged panels prior to and post-ballistics testing may be found in Appendix G.

The damage caused by the ballistic impact to the panel that had no initial damage, Fig. 4.21(b), covers a circular area with a radius of approximately 3.5 cm. Beyond that radius minimal damage appears in the ceramic panel with the exception of approximately 12 through thickness cracks that radiate out from the point of impact. The contrast between the radial cracks and the surrounding armor reduces as the cracks radiate out suggesting that the cracks become more tightly closed as they reach the edge of the armor panel. Horsfall et al. (1993) noted that if cracks in the ceramic portion of an armor plate may be considered closed, they will have a minimal to negligible effect on the ballistics performance of the armor panel. In comparison, the radial cracks in panel B that were present prior to ballistics testing, as evidence by the contrast difference of the pre and post ballistics images, appear to have opened further post-ballistics testing. Cracks induced in panel B due to ballistics impact appear to be opened wider than compared to those of the cracks induced from ballistics testing in the panel with no initial damage.

Damage at the impact site in the panels with pre-existing cracks is not uniform from panel to panel. In contrast to the armor panel with no pre-existing cracks, the damage at the impact site in the panels with pre-existing cracks follows the crack structure that was initially present. The damage does not spread out in a radially uniform manner. The behavior of the damage accumulation in the panels with pre-existing cracks is not easily predictable as compared to the

damage accumulation in panels with no pre-existing cracks and could lead to an unanticipated loss in ballistic performance that would not be expected if the panels were not initially damaged.

Visible in the post-ballistic impact x-ray images of panel B but absent in the initially undamaged panel are cracks extending between the radial cracks. The crack structure of panel B post-ballistics impact appears chaotic compared to that of the initially undamaged panel. The cracks connecting the radial cracks cause the ceramic around the impact site to be divided into small pieces. A high number of small pieces may allow for movement of the ceramic upon another ballistic impact potentially reducing the ballistic performance and multiple hit effectiveness of the armor panel. Figures G.1 and G.2 in Appendix G also show chaotic crack patterns with cracks connecting radial cracks and the ceramic surrounding the ballistic impact site being divided into small pieces.

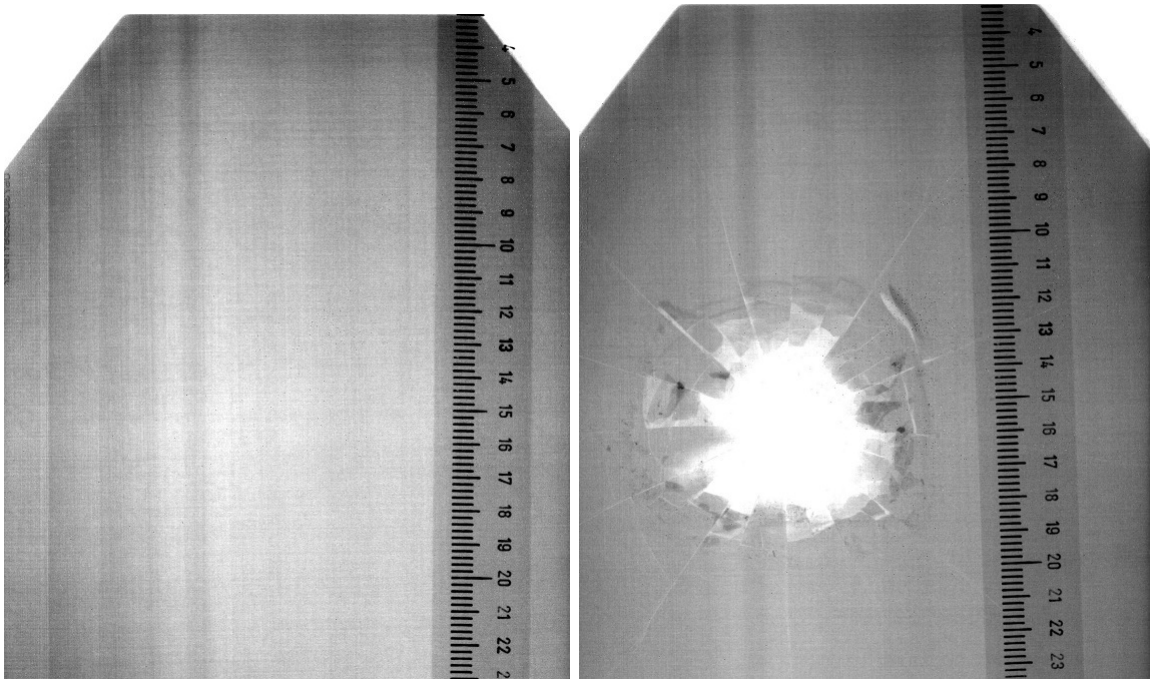

(a) Undamaged panel prior to ballistics impact. (b) Undamaged panel post-ballistics impact.

Figure 4.21 X-rays of a damaged and undamaged ceramic armor panel after ballistic impact (scale in centimeters).

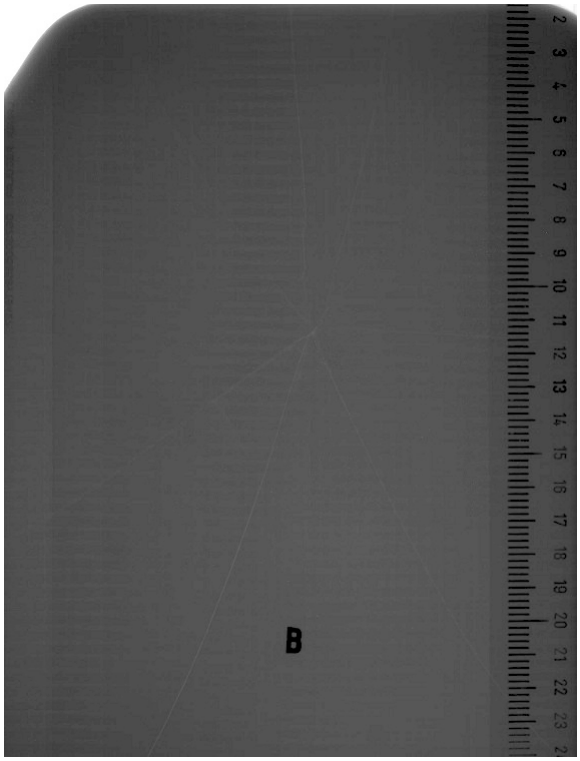

(a) Damaged panel B prior to ballistic impact

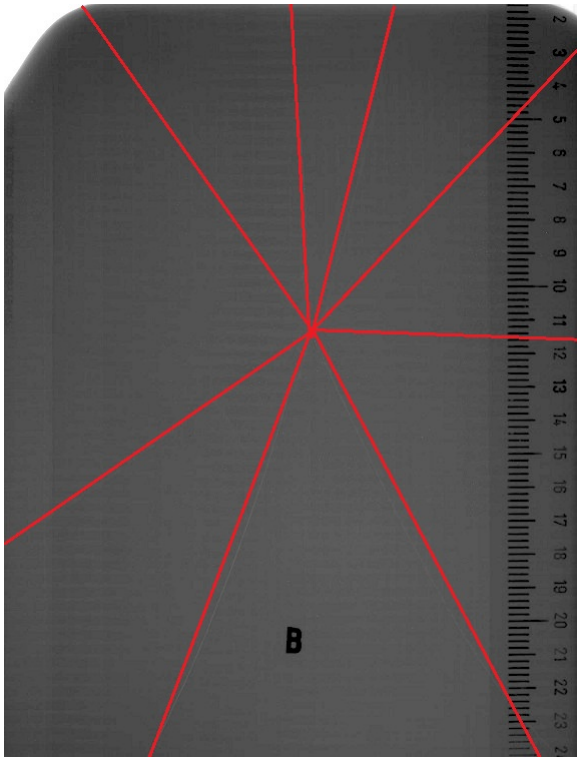

(b) Damaged panel B prior to ballistic impact (cracks marked)

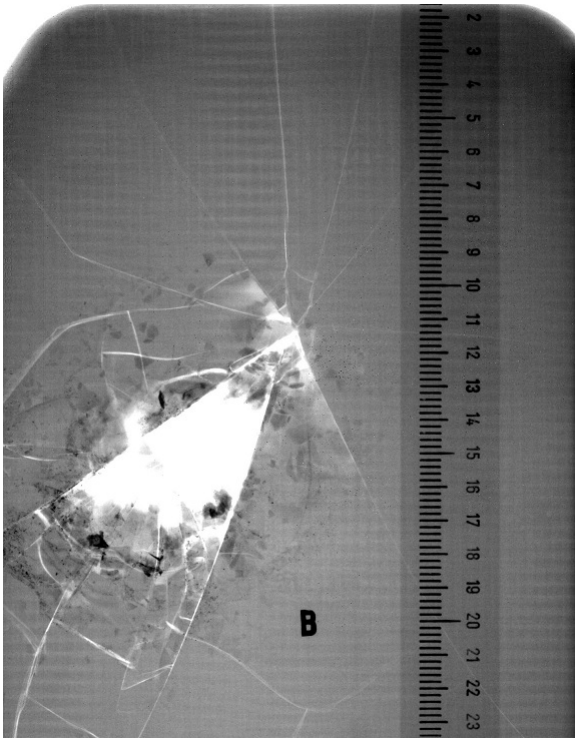

(c) Damaged panel B post-ballistic impact

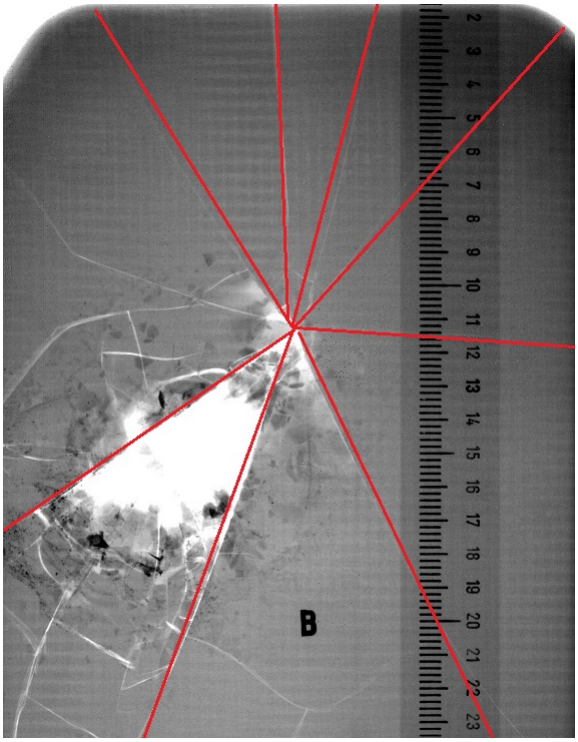

(d) Damaged panel B post-ballistic impact (pre-existing cracks marked

Figure 4.22 X-rays of a damaged ceramic armor panel prior to and post-ballistic impact (scale in centimeters).

CHAPTER 5. CONCLUSIONS

Impact experiments have been performed on ceramic armor panels with impactors of varying mass, instrumented with a force transducer and accelerometer, and employing a CPR manikin to model a human torso. Experiments have shown that as the impact energy of the mass increased the resulting acceleration of the impactor and force of impact increased. Maximum acceleration values for the small impactor were larger than those of the large impactor for a given impact energy. The amount of deflection in the manikin's chest on impact was greater for the large impactor as compared to the small impactor resulting in impact events of longer time duration and leading to lower acceleration and force profiles. Multiplying the acceleration profile of a given impact by the mass of the impactor recovered the force profile of the impact. A minor discrepancy was seen which may be attributed to the force transducer not impacting the armor at normal incidence.

Impacts onto damaged armor panels revealed force and acceleration profiles that were dissimilar to the profiles from impacts onto undamaged panels. Profiles resulting from impacts onto damaged armor panels had a lower maximum force and acceleration value as compared to impacts onto undamaged panels at a given impact energy. Cracks in the ceramic material of a damaged panel caused the armor panel to become more flexible as the composite material is left supplying the stiffness to the armor plate allowing greater deformation of the armor plate during impact, increasing the duration of the impact event and producing lower accelerations and forces.

Impact experiments employing the PSF showed that the indication level present on the PSF post impact relates to the measured force of the impact. Impacts with higher impact energies produced indications with saturation levels higher than those of indications from impacts of lower impact energy levels. Impacts from employing the small impactor produced indications

with higher saturation levels than indications from impacts employing the large impactor at the same impact energy. Good agreement was shown between pressure values obtained from PSF and those calculated from the force data and force transducer area for a given impact event. Digitized images of PSF provided a clear distinction of the saturation levels of an indication and provided an accurate pressure reading.

The numerical model captured the general trends of the experimental data for each impactor through a range of impact energies. Discrepancies arose between the model results and the experimental data for, the maximum acceleration values, the maximum displacement values, and the time duration of the impacts. The model does predict that the small impactor produces larger accelerations than the large impactor for a given impact energy and that the time duration of the impact for the small impactor is shorter than that of the large impactor, both results seen experimentally. Also a larger displacement of the impactor during the impact event was seen for the large impactor as compared to the small impactor which follows with experimental data.

Contributing to the error of the model was the use of a linear elastic material used to model the human torso, neglecting the nonlinear and visco-elastic properties of an actual human chest. The results of the numerical model were also highly dependent on the material properties of both the ceramic and the composite. Average material properties for the two were used in the model but a slight change in either results in significant changes in the magnitude of the acceleration profiles. The numerical model also did not incorporate the adhesive layer between the two materials. For the armor panels employed in the experimental tests, the adhesive was very compliant and relatively thick and its absence from the model may have led to error in the results.

The analytical model captured the general trends of the experimental acceleration profiles for each impactor through a range of impact energies. Peak values of acceleration along with the time duration of the impact events were recovered with minimal error. The error present between the analytical model and the experimental data stems from the highly complex nature of the system being modeled. Contributing extensively to the complexity of modeling the system is the armor plate not being completely constrained to the manikin. Upon impact

lateral movement may occur in the armor panel relative to the manikin. The intensity of the impact may also cause movement in the manikin. Both effects deviate from the constrained direct impacts that the analytical model was developed to handle [Lieberman et al. (1994)].

The minimal error present in the analytical models suggests that they may be used to predict acceleration profiles, and thus forces and pressures, for impact events employing a range of impactor masses and impact energies. Assuming the average maximum pressure the ceramic material in the armor panels could withstand is known, the model could be used to predict at which impact energies a given mass may produce a pressure that has the potential to cause damage. Experimental data is needed to determine the constants in the analytical model for a particular mass but once the constants are set they may be used for that mass through a wide range of impact energies.

Ballistics testing was performed on both damaged and undamaged armor panels. All armor panels tested defeated the ballistic threat and prevented penetration of the armor. Damage due to ballistic impact appears more extensive in the armor panels that had initial cracks in them. X-ray images of the armor panels prior to and post ballistics impact show that the initial cracks in the damage panels open wider after ballistics impact at a distance from the impact site. Cracks bridging occcured between the cracks that radiate out from the impact site, for both radial cracks that were initially present and created from the ballistics impact, for all initially damaged armor panels post ballistics impact. These bridging cracks did not appear in the initially undamaged armor panel post ballistics impact. Damaged acquired post ballistics impact in the initially undamaged armor panel was isolated to the impact site out to a radius of approximately 3.5 cm. Radial cracks also extended out from the impact site to the edge of the armor but remain closed compared to the radial cracks in the initially damaged armor panels post ballistics impact. While the initially damaged armor panels retained their ability to defeat a ballistics threat, the extensive damage they acquired as compared to the initially undamaged armor panel post ballistics impact may lead to a loss in their ability to provide multiple hit protection.

Pressure sensitive dye-indicator film has been shown to provide an accurate estimate of the pressure applied to a piece of ceramic body armor due to an impact. The PSF has been

shown accurate for a range of impactor masses and through a range of impact energies from lower energies through energy levels that produced forces with the potential to damage the ceramic armor. While the PSF does not provide a direct measure of damage sustained on a piece of ceramic through an impact, it does reveal the approximate maximum pressure applied by the impact. Knowing the maximum applied pressure allows an individual to quickly tell if the impact was enough to cause possible damage to the armor and eliminates the need to examine the armor after every sustained impact, cutting down on the time and expense needed to inspect the armor.

APPENDIX A. NUMERICAL RESULTS: SMALL IMPACTOR

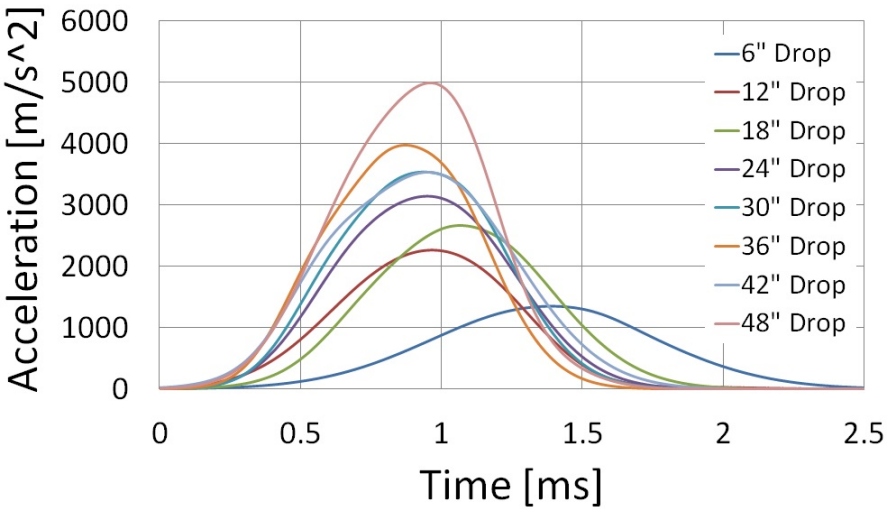

Figure A.1 Experimental accelerations for the small impactor.

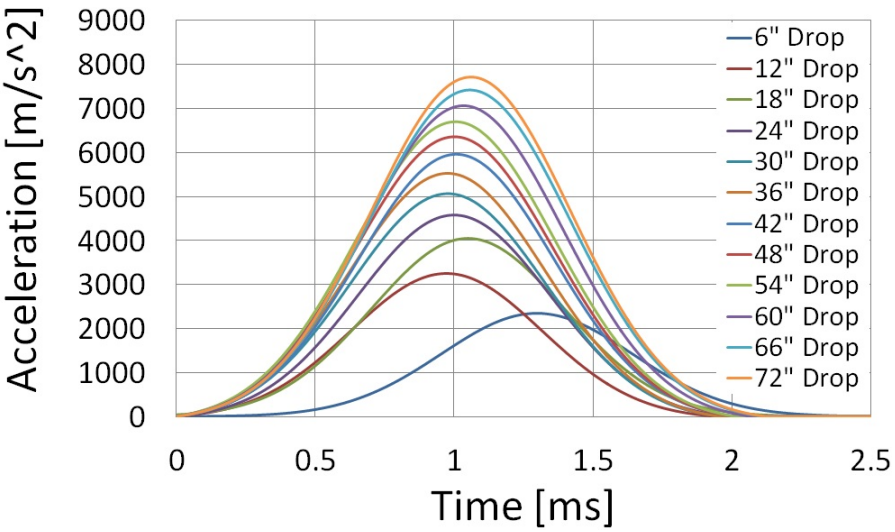

Figure A.2 Numerical accelerations forthe small impactor.

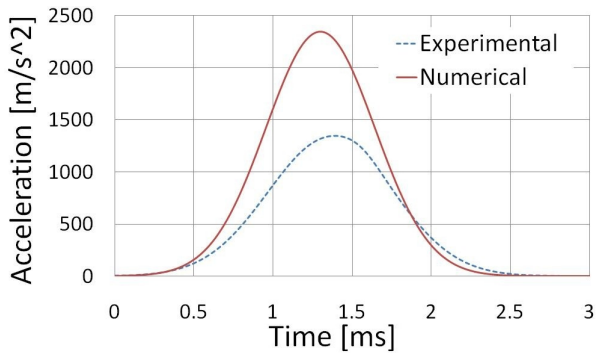

Figure A.3 Comparison of experimental and numerical accelerations for the small impactor from a 6" drop.

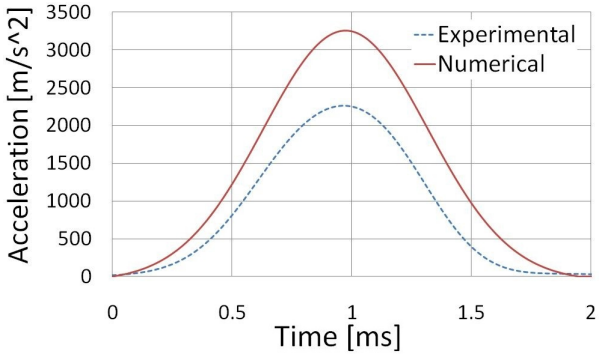

Figure A.4 Comparison of experimental and numerical accelerations for the small impactor from a 12" drop.

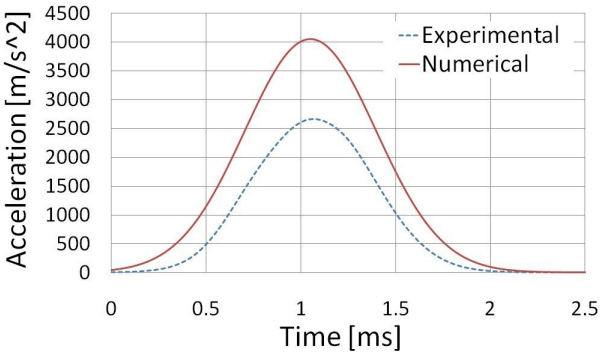

Figure A.5 Comparison of experimental and numerical accelerations for the small impactor from a 18" drop.

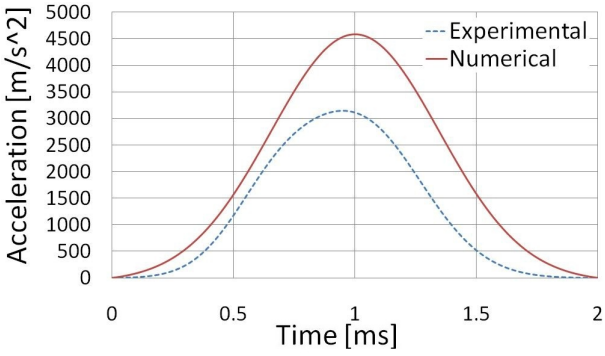

Figure A.6 Comparison of experimental and numerical accelerations for the small impactor from a 24" drop.

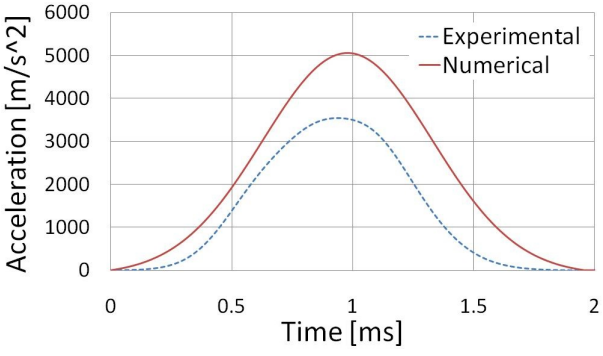

Figure A.7 Comparison of experimental and numerical accelerations for the small impactor from a 30" drop.

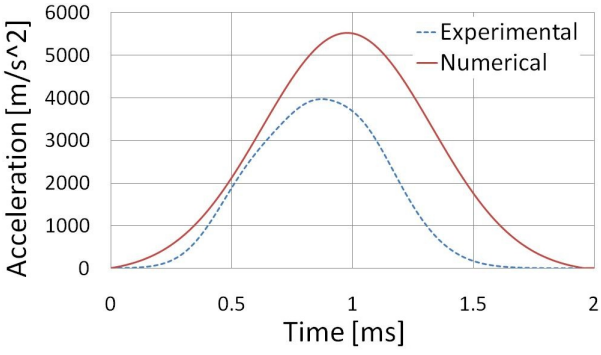

Figure A.8 Comparison of experimental and numerical accelerations for the small impactor from a 36" drop.

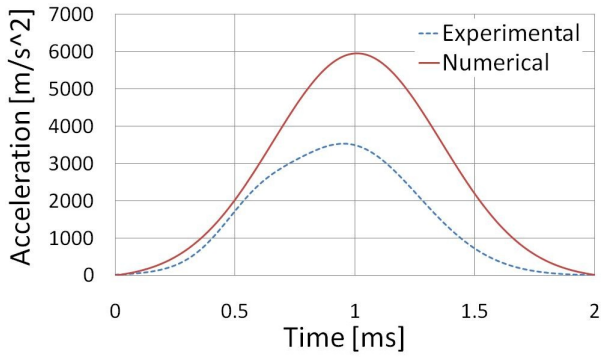

Figure A.9 Comparison of experimental and numerical accelerations for the small impactor from a 42" drop.

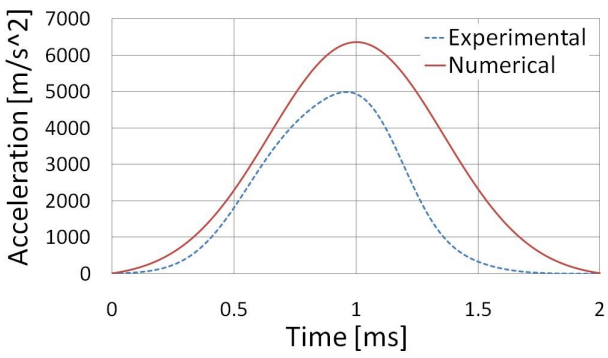

Figure A.10 Comparison of experimental and numerical accelerations for the small impactor from a 48" drop.

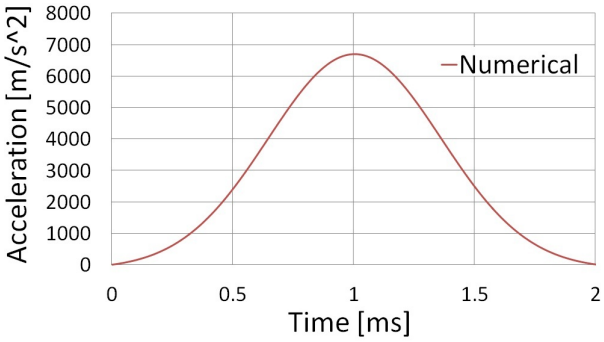

Figure A.11 Numerical acceleration for the small impactor from a 54" drop.

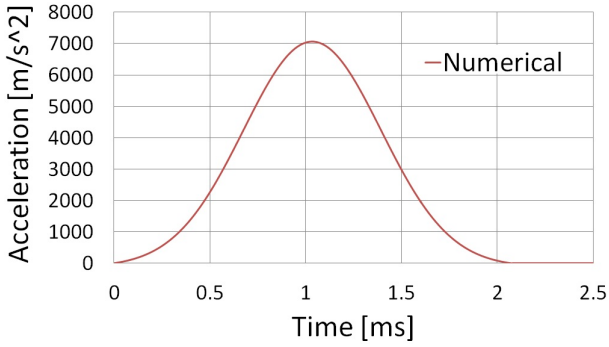

Figure A.12 Numerical acceleration for the small impactor from a 60" drop.

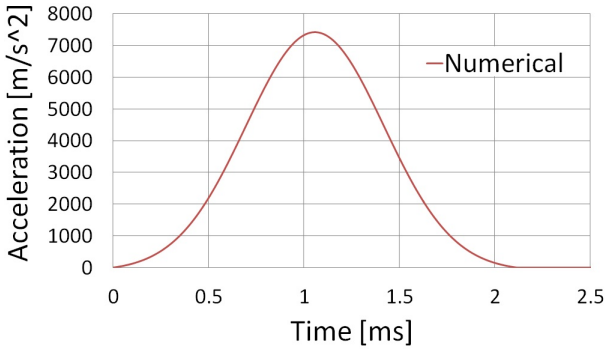

Figure A.13 Numerical acceleration for the small impactor from a 66" drop.

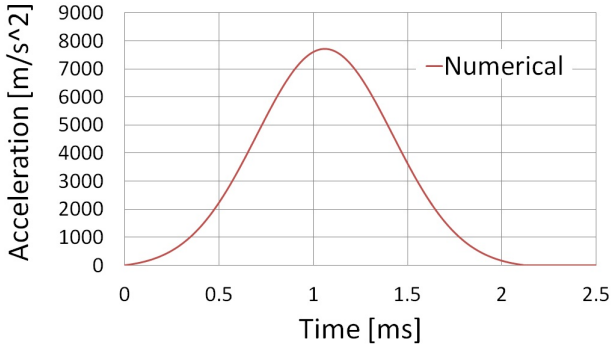

Figure A.14 Numerical acceleration for the small impactor from a 72" drop.

APPENDIX B. NUMERICAL RESULTS: MEDIUM IMPACTOR

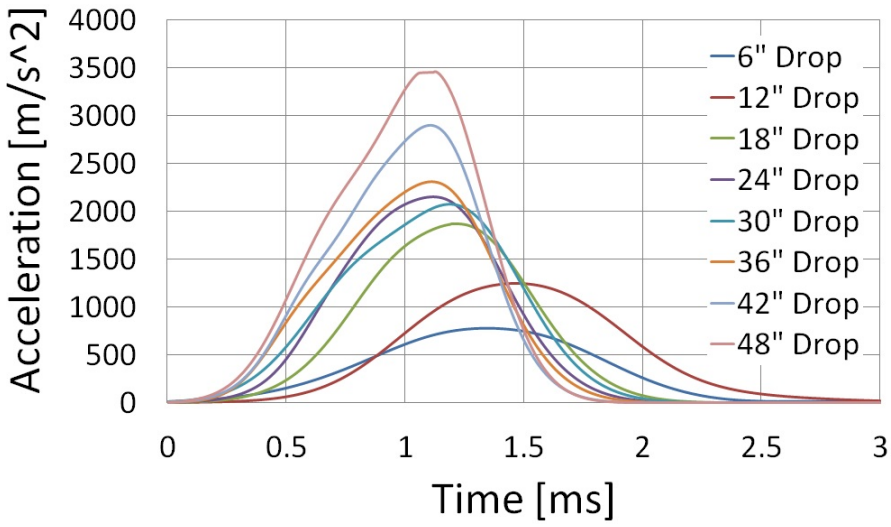

Figure B.1 Experimental accelerations for the medium impactor.

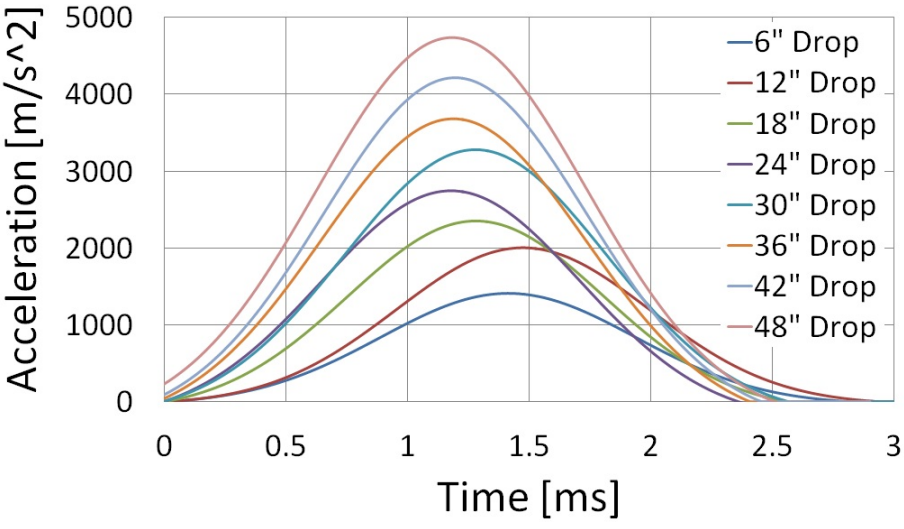

Figure B.2 Numerical accelerations for the medium impactor.

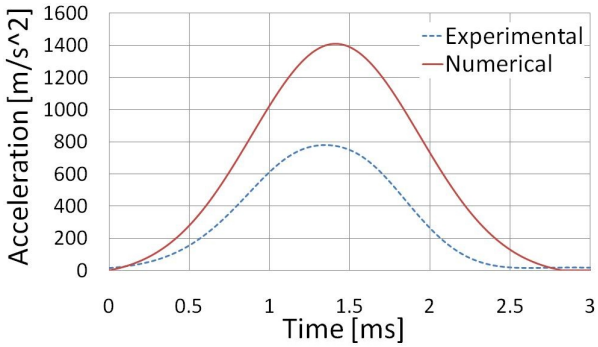

Figure B.3 Comparison of experimental and numerical accelerations for the medium impactor from a 6" drop.

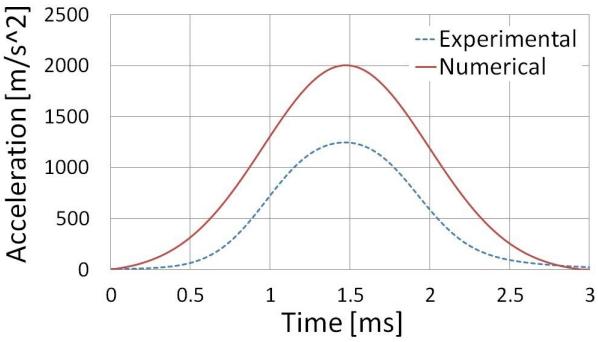

Figure B.4 Comparison of experimental and numerical accelerations for the medium impactor from a 12" drop.

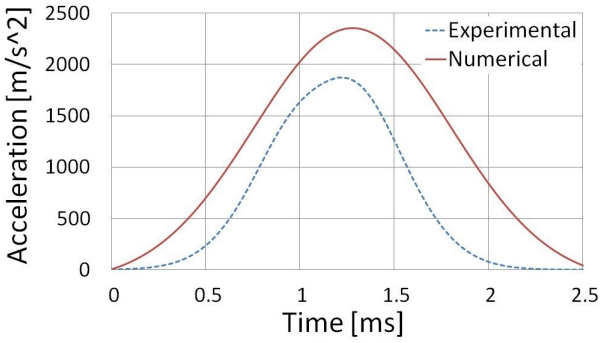

Figure B.5 Comparison of experimental and numerical accelerations for the medium impactor from a 18" drop.

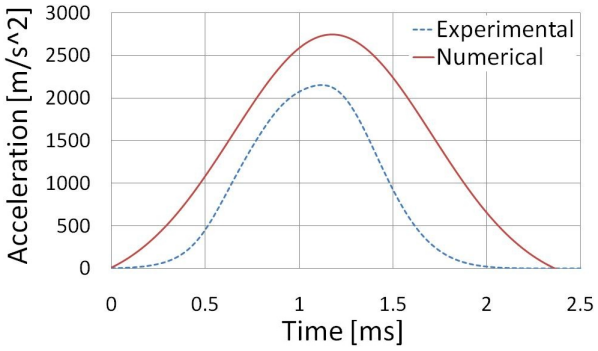

Figure B.6 Comparison of experimental and numerical accelerations for the medium impactor from a 24" drop.

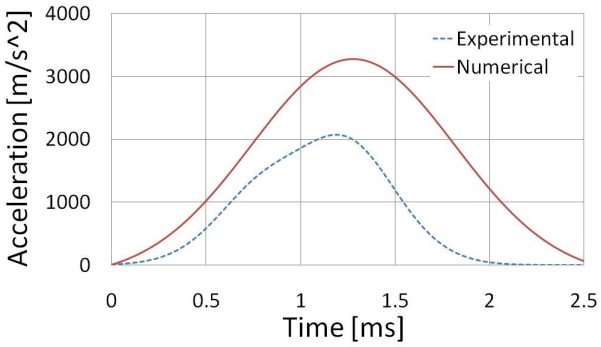

Figure B.7 Comparison of experimental and numerical accelerations for the medium impactor from a 30" drop.

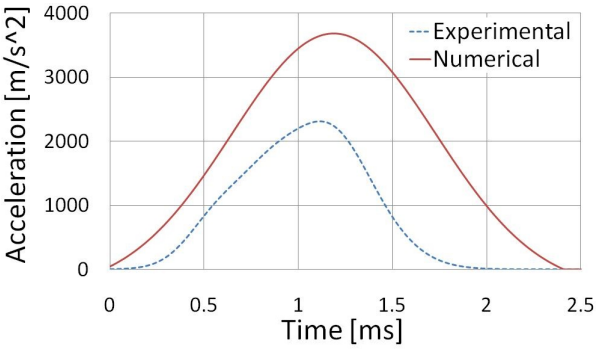

Figure B.8 Comparison of experimental and numerical accelerations for the medium impactor from a 36" drop.

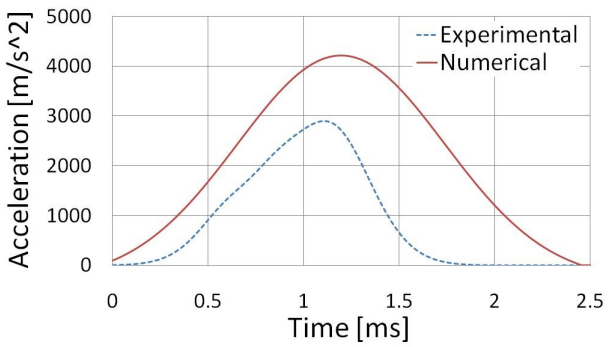

Figure B.9 Comparison of experimental and numerical accelerations for the medium impactor from a 42" drop.

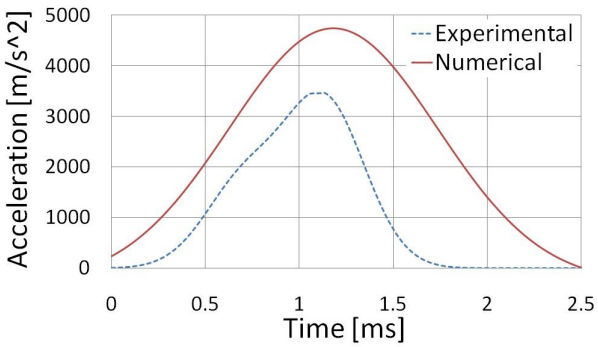

Figure B.10 Comparison of experimental and numerical accelerations for the medium impactor from a 48" drop.

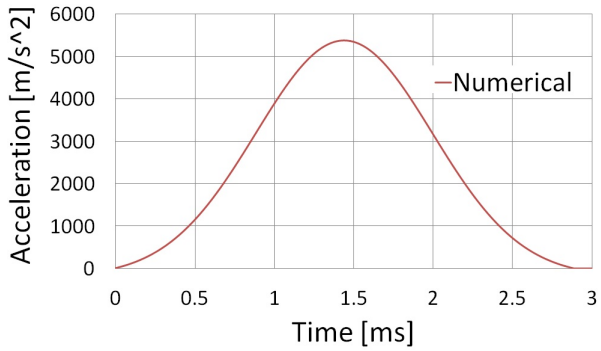

Figure B.11 Numerical acceleration for the medium impactor from a 54" drop.

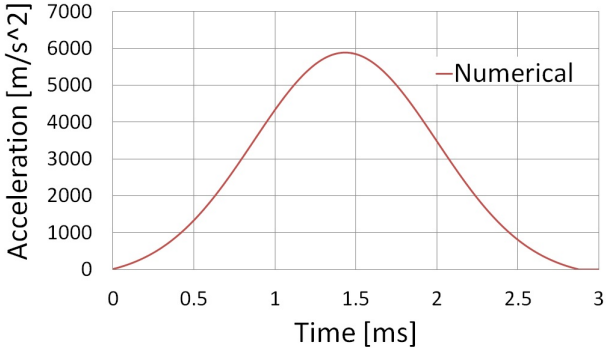

Figure B.12 Numerical acceleration for the medium impactor from a 60" drop.

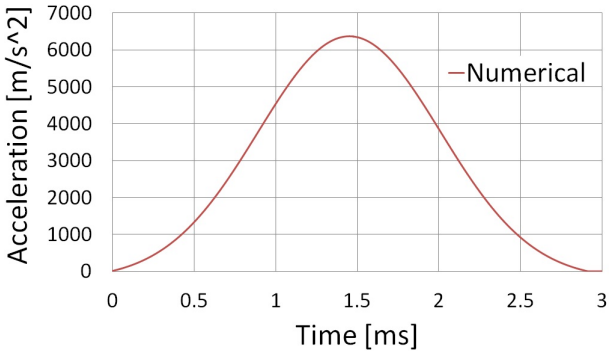

Figure B.13 Numerical acceleration for the medium impactor from a 66" drop.

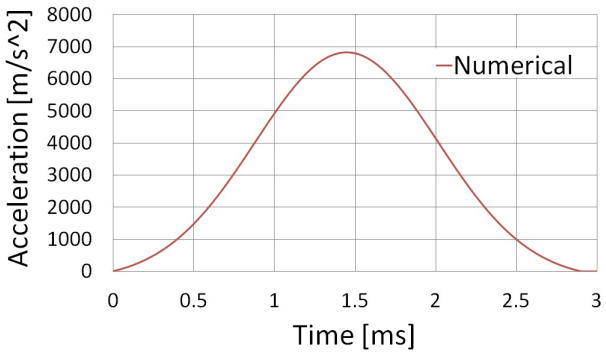

Figure B.14 Numerical acceleration for the medium impactor from a 72" drop.

APPENDIX C. NUMERICAL RESULTS: LARGE IMPACTOR

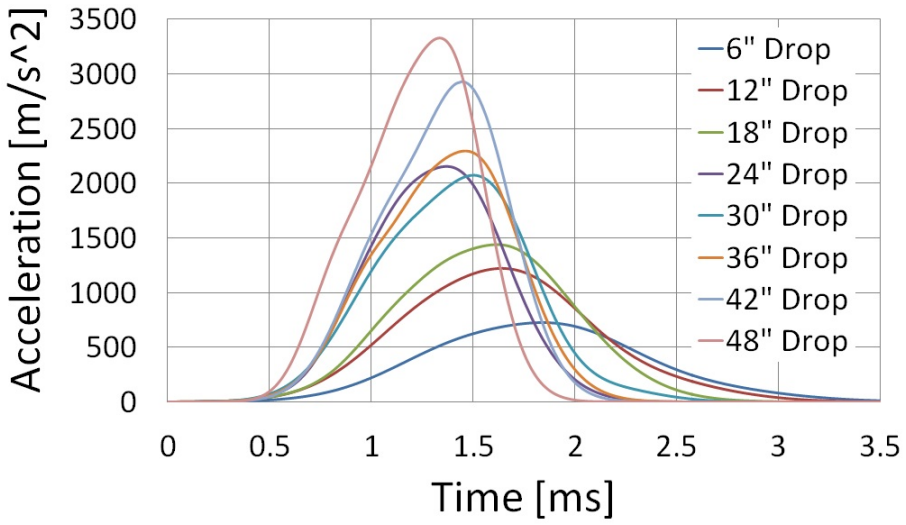

Figure C.1 Experimental accelerations for the large impactor.

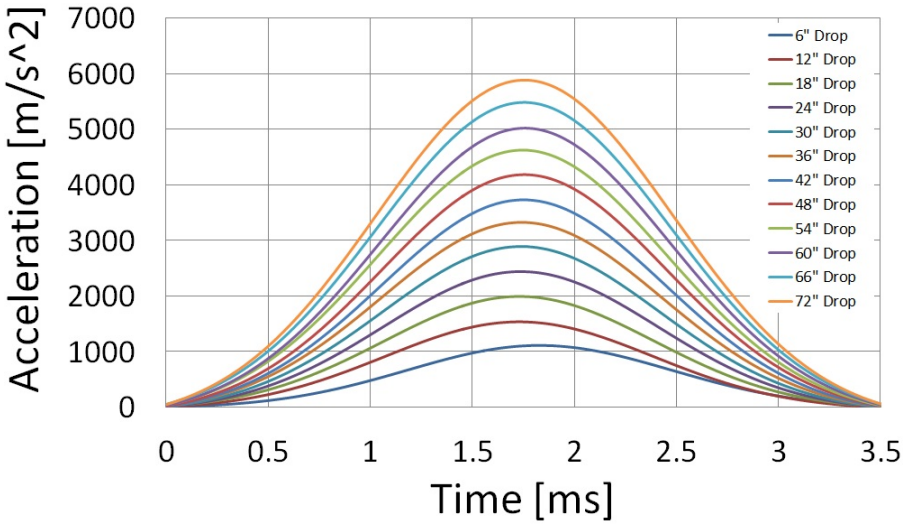

Figure C.2 Numerical accelerations for the large impactor.

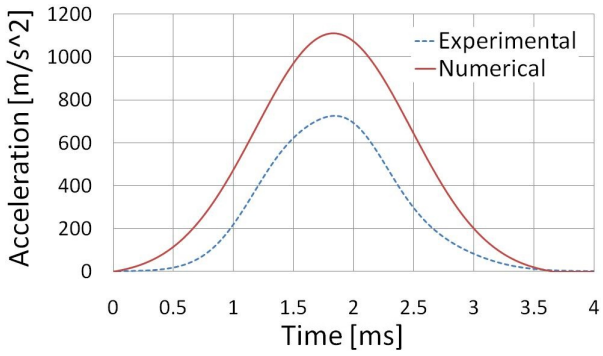

Figure C.3 Comparison of experimental and numerical accelerations for the large impactor from a 6" drop.

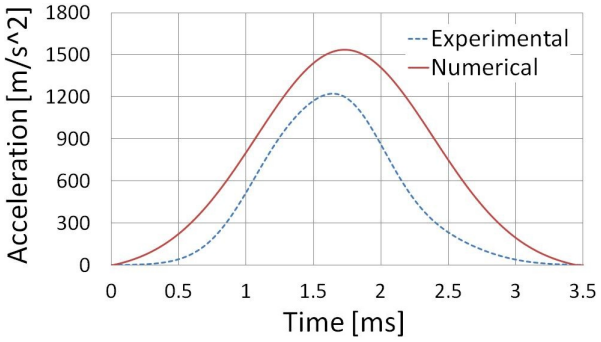

Figure C.4 Comparison of experimental and numerical accelerations for the large impactor from a 12" drop.

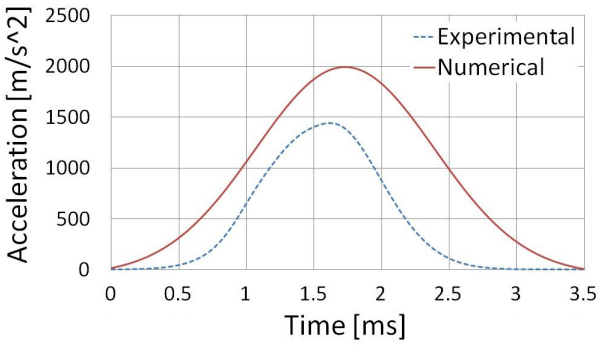

Figure C.5 Comparison of experimental and numerical accelerations for the large impactor from a 18" drop.

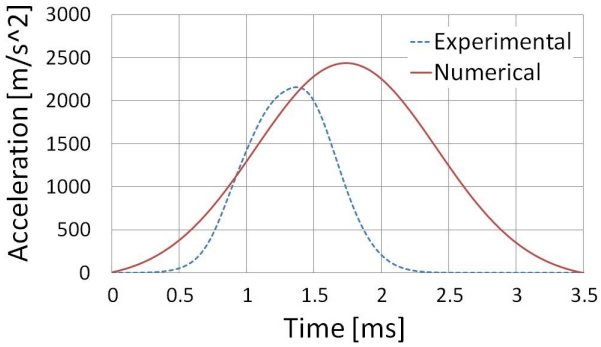

Figure C.6 Comparison of experimental and numerical accelerations for the large impactor from a 24" drop.

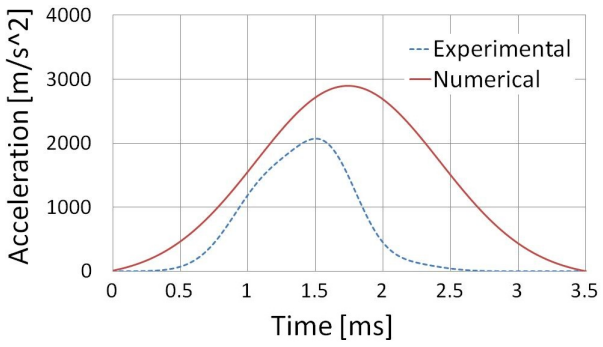

Figure C.7 Comparison of experimental and numerical accelerations for the large impactor from a 30" drop.

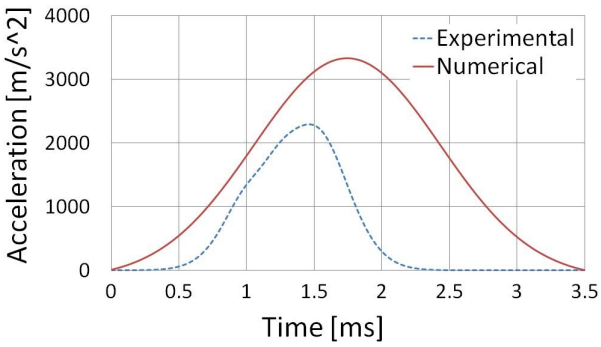

Figure C.8 Comparison of experimental and numerical accelerations for the large impactor from a 36" drop.

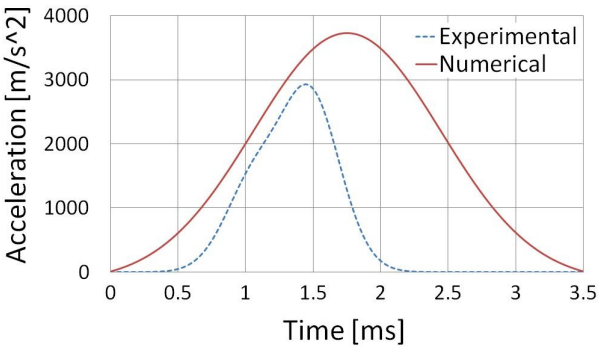

Figure C.9 Comparison of experimental and numerical accelerations for the large impactor from a 42" drop.

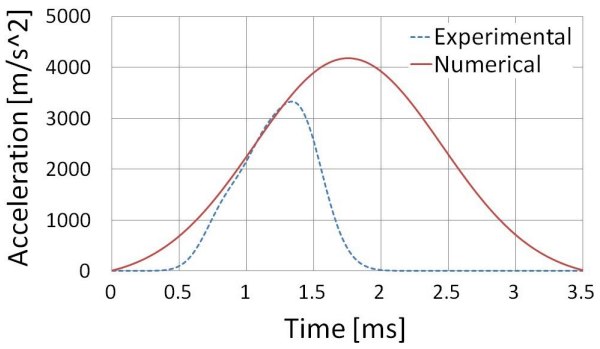

Figure C.10 Comparison of experimental and numerical accelerations for the large impactor from a 48" drop.

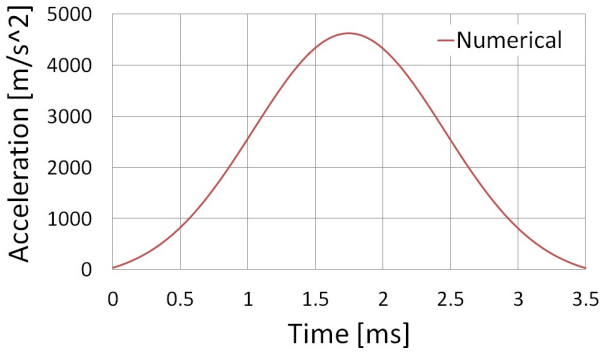

Figure C.11 Numerical acceleration for the large impactor from a 54" drop.

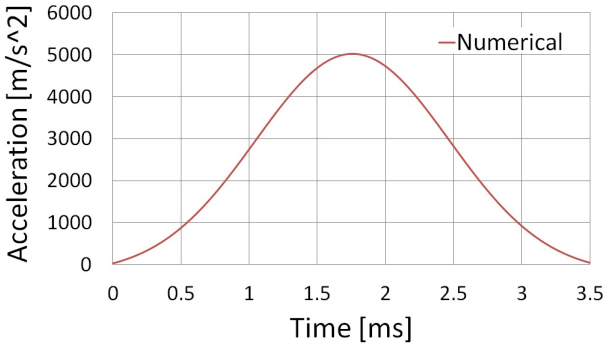

Figure C.12 Numerical acceleration for the large impactor from a 60" drop.

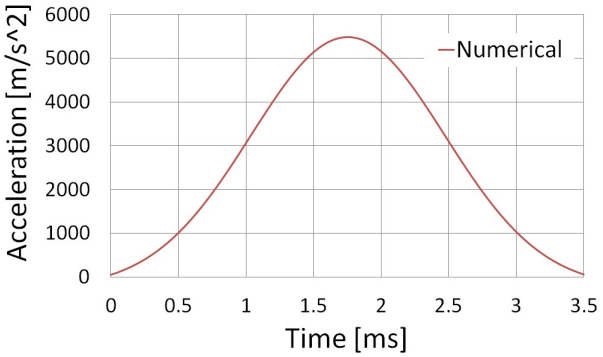

Figure C.13 Numerical acceleration for the large impactor from a 66" drop.

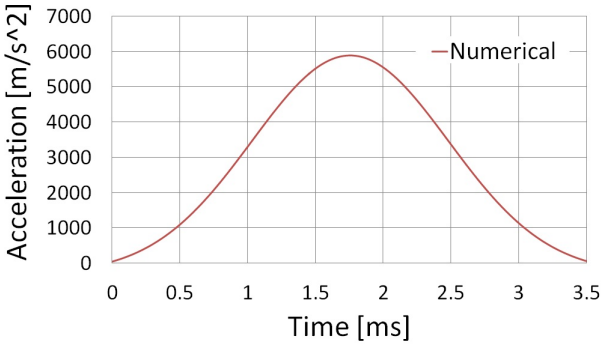

Figure C.14 Numerical acceleration for the large impactor from a 72" drop.

APPENDIX D. ANALYTICAL RESULTS: SMALL IMPACTOR

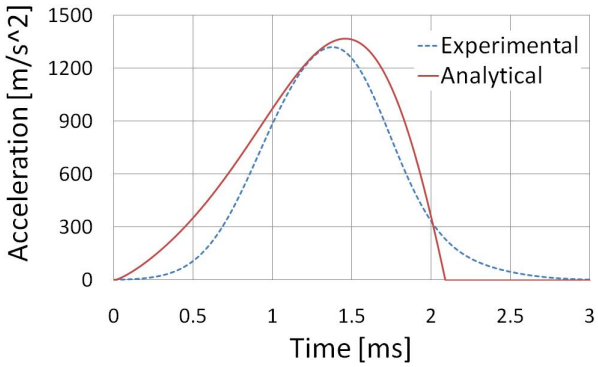

Figure D.1 Comparison of experimental and analytical accelerations for the small impactor from a 6" drop.

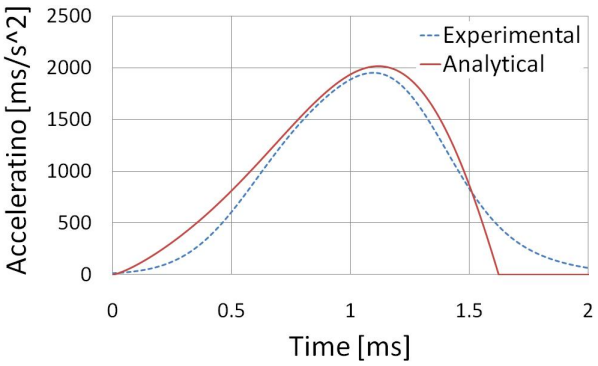

Figure D.2 Comparison of experimental and analytical accelerations for the small impactor from a 12" drop.

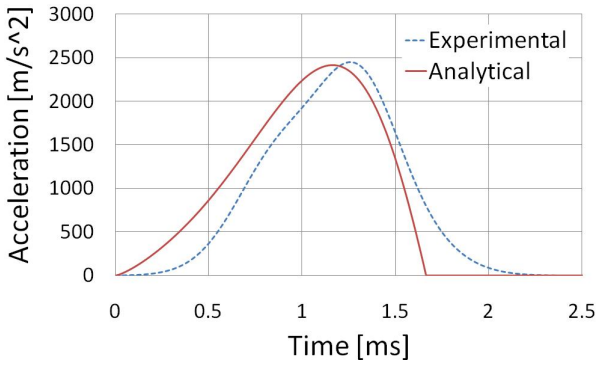

Figure D.3 Comparison of experimental and analytical accelerations for the small impactor from a 18" drop.

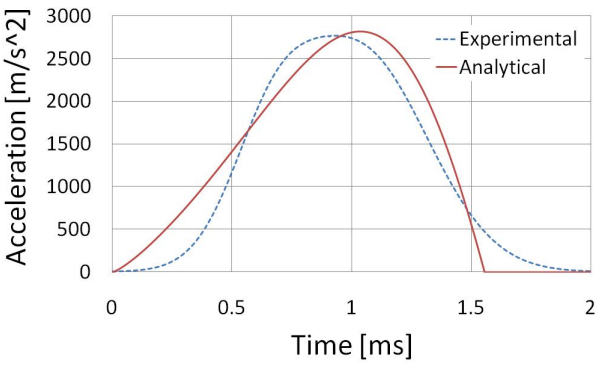

Figure D.4 Comparison of experimental and analytical accelerations for the small impactor from a 24" drop.

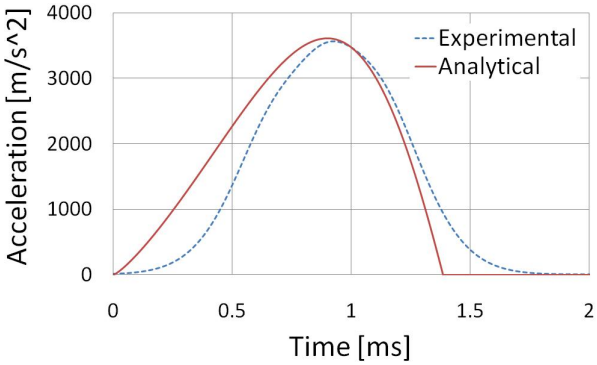

Figure D.5 Comparison of experimental and analytical accelerations for the small impactor from a 30" drop.

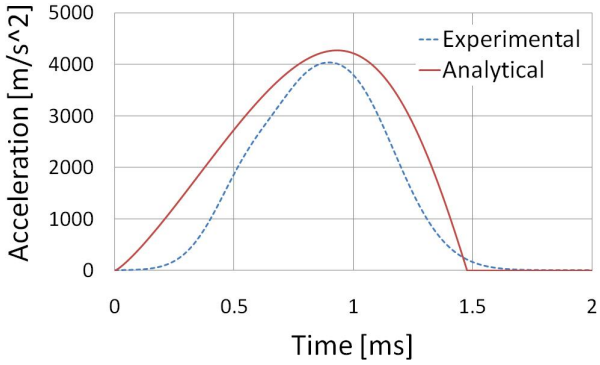

Figure D.6 Comparison of experimental and analytical accelerations for the small impactor from a 36" drop.

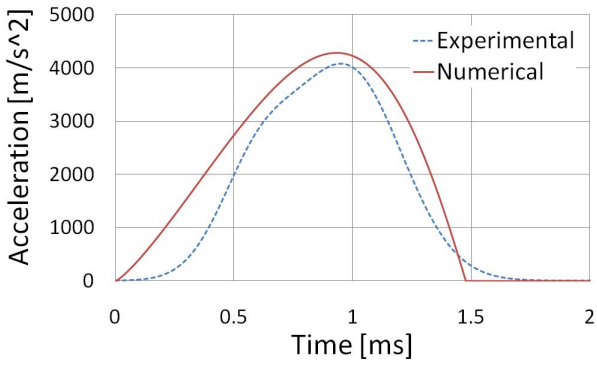

Figure D.7 Comparison of experimental and analytical accelerations for the small impactor from a 42" drop.

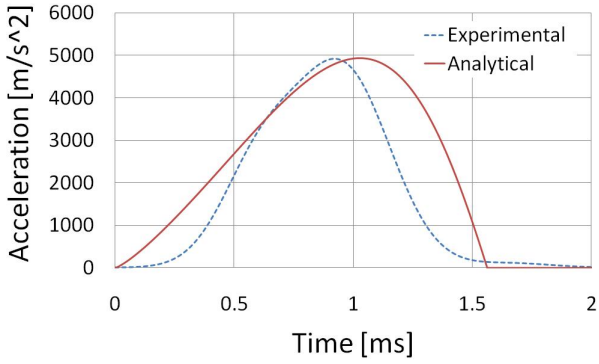

Figure D.8 Comparison of experimental and analytical accelerations for the small impactor from a 48" drop.

APPENDIX E. ANALYTICAL RESULTS: MEDIUM IMPACTOR

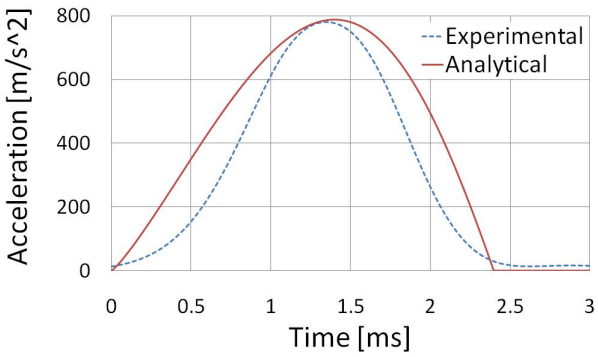

Figure E.1 Comparison of experimental and analytical accelerations for the medium impactor from a 6" drop.

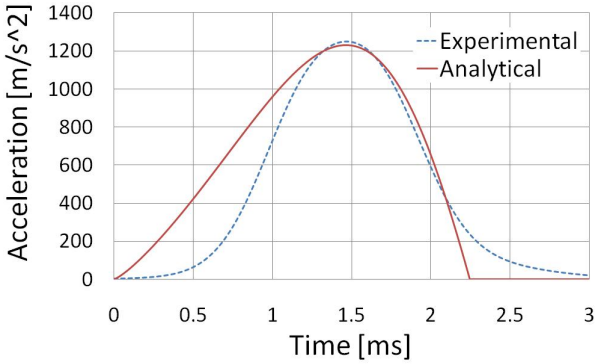

Figure E.2 Comparison of experimental and analytical accelerations for the medium impactor from a 12" drop.

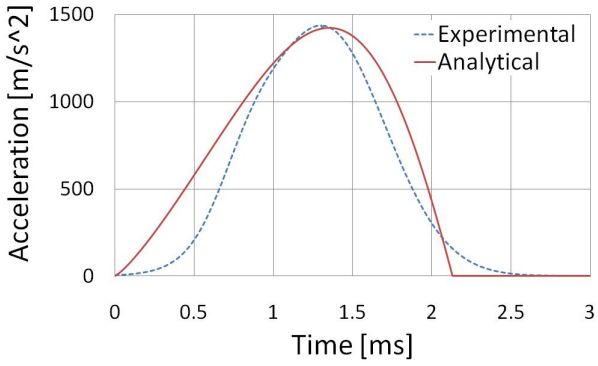

Figure E.3 Comparison of experimental and analytical accelerations for the medium impactor from a 18" drop.

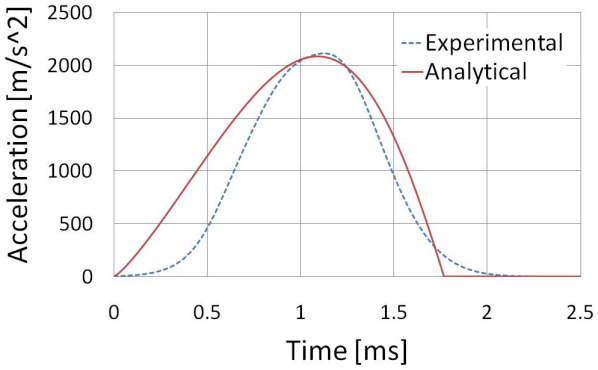

Figure E.4 Comparison of experimental and analytical accelerations for the medium impactor from a 24" drop.

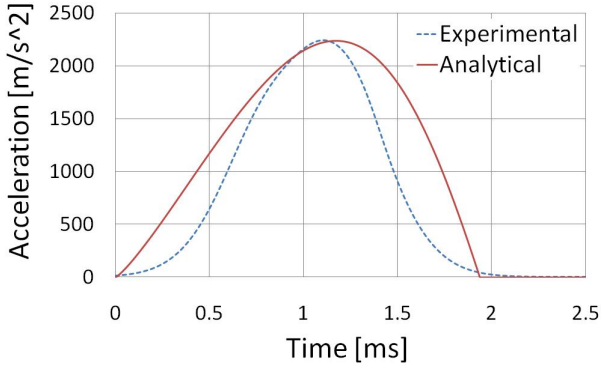

Figure E.5 Comparison of experimental and analytical accelerations for the medium impactor from a 30" drop.

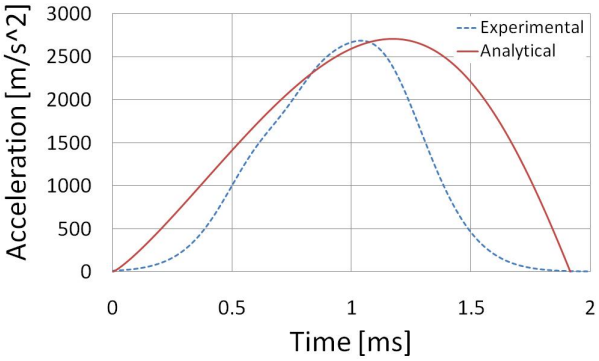

Figure E.6 Comparison of experimental and analytical accelerations for the medium impactor from a 36" drop.

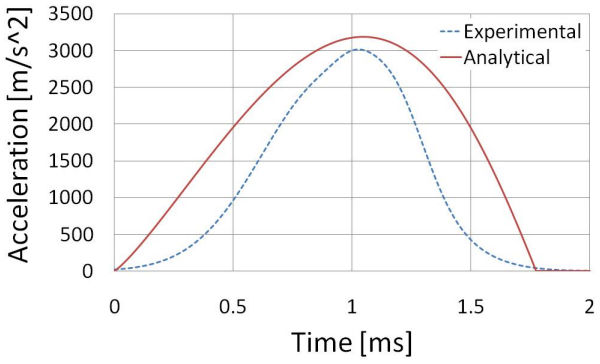

Figure E.7 Comparison of experimental and analytical accelerations for the medium impactor from a 42" drop.

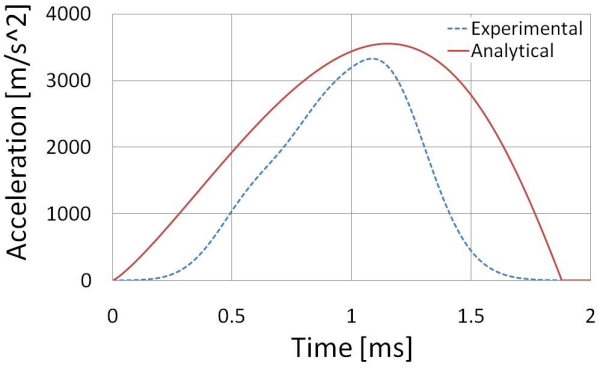

Figure E.8 Comparison of experimental and analytical accelerations for the medium impactor from a 48" drop.

APPENDIX F. ANALYTICAL RESULTS: LARGE IMPACTOR

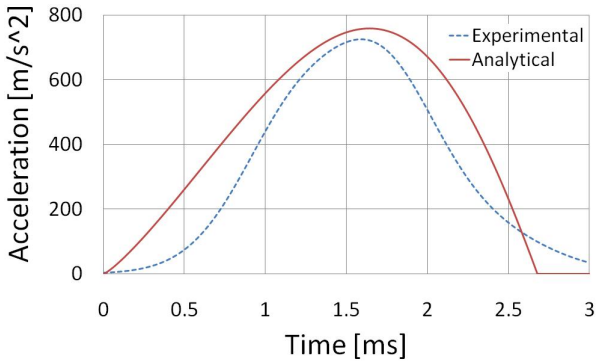

Figure F.1 Comparison of experimental and analytical accelerations for the large impactor from a 6" drop.

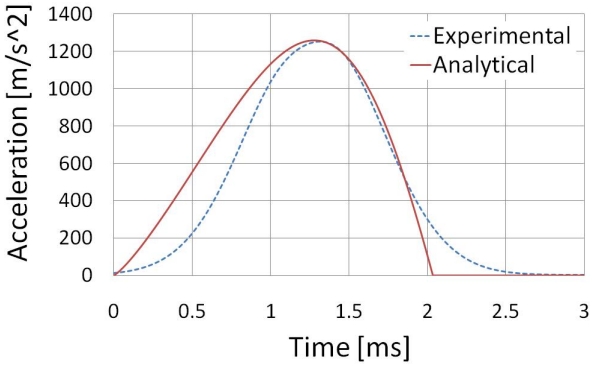

Figure F.2 Comparison of experimental and analytical accelerations for the large impactor from a 12" drop.

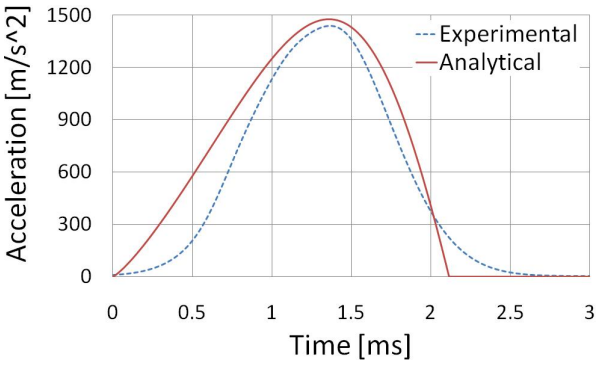

Figure F.3 Comparison of experimental and analytical accelerations for the large impactor from a 18" drop.

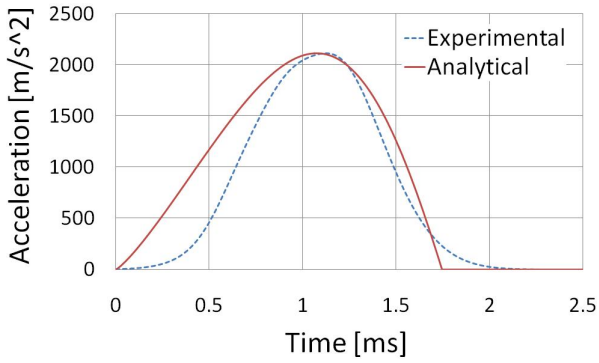

Figure F.4 Comparison of experimental and analytical accelerations for the large impactor from a 24" drop.

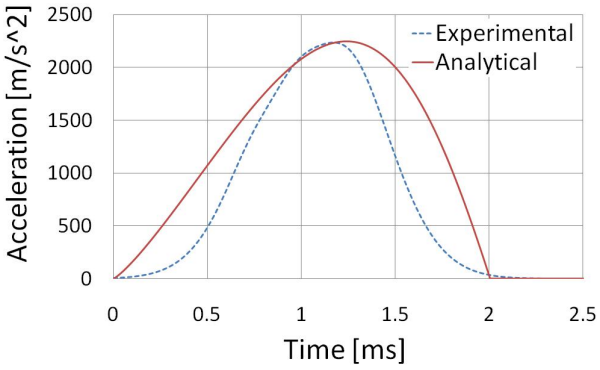

Figure F.5 Comparison of experimental and analytical accelerations for the large impactor from a 30" drop.

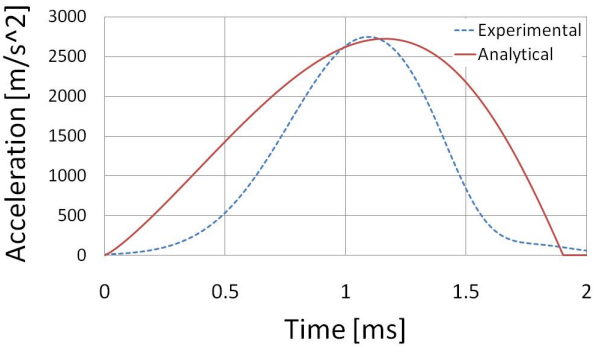

Figure F.6 Comparison of experimental and analytical accelerations for the large impactor from a 36" drop.

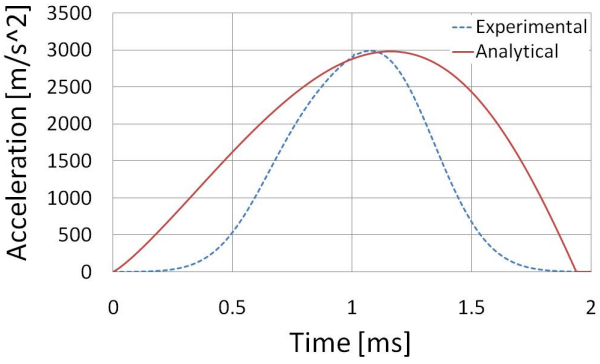

Figure F.7 Comparison of experimental and analytical accelerations for the large impactor from a 42" drop.

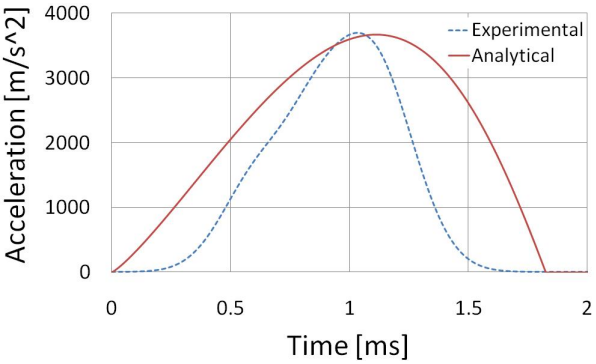

Figure F.8 Comparison of experimental and analytical accelerations for the large impactor from a 48" drop.

APPENDIX G. X-RAYS OF ARMOR PANELS PRIOR TO AND POST-BALLISTICS IMPACT

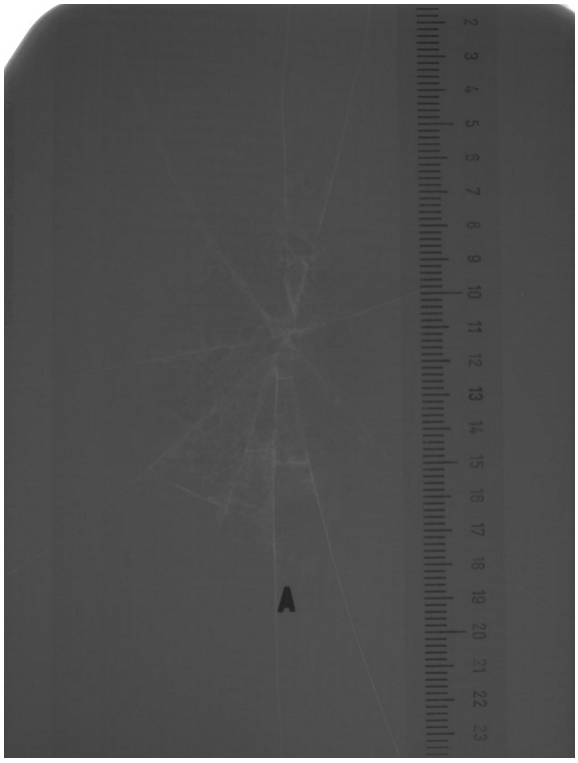

(a) Damaged panel A prior to ballistics impact.

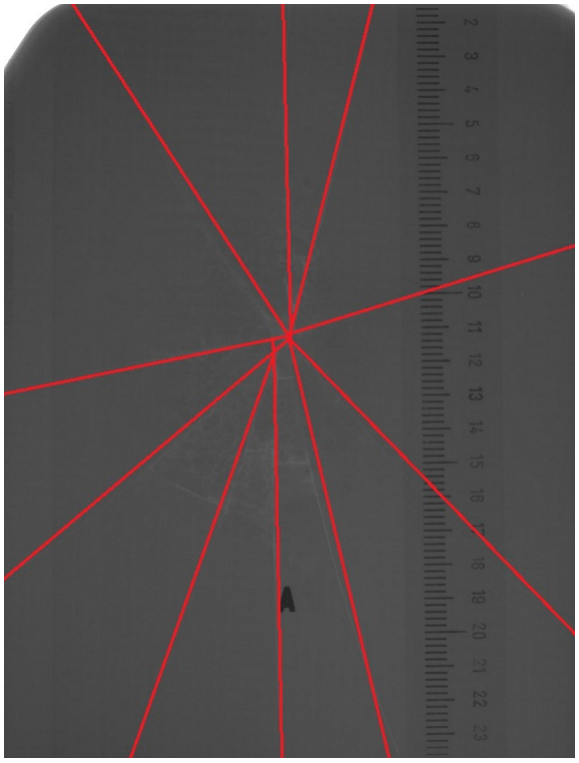

(b) Damaged panel A (cracks marked) prior to ballistics impact.

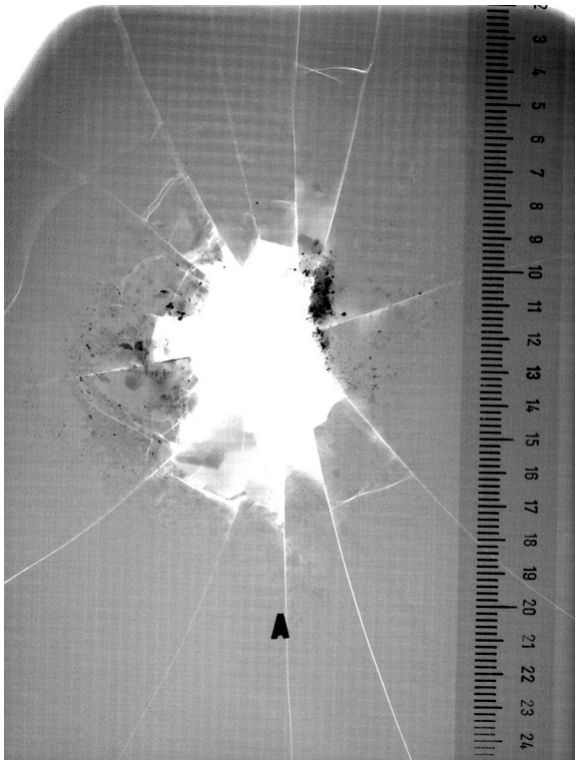

(c) Damaged panel A post-ballistics impact.

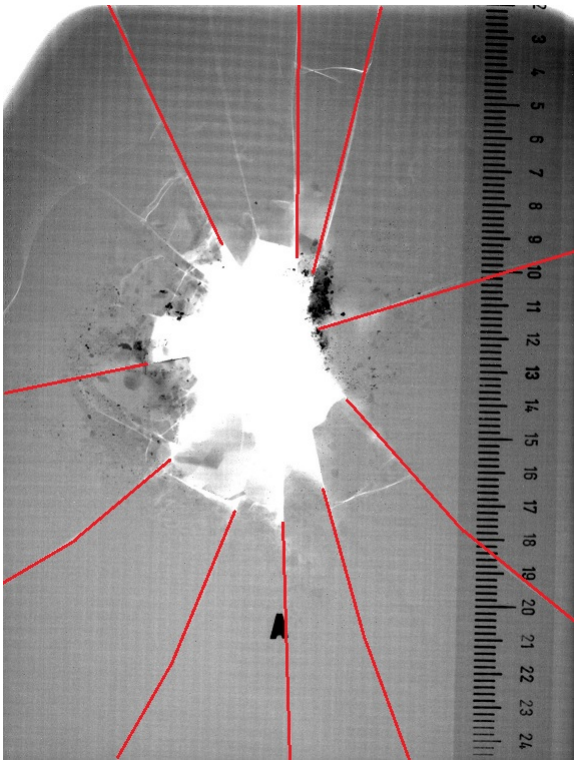

(d) Damaged panel A (pre-existing cracks marked) post-ballistics impact.

Figure G.1 X-rays of a damaged ceramic armor panel prior to and post-ballistic impact. (Scales in cm)

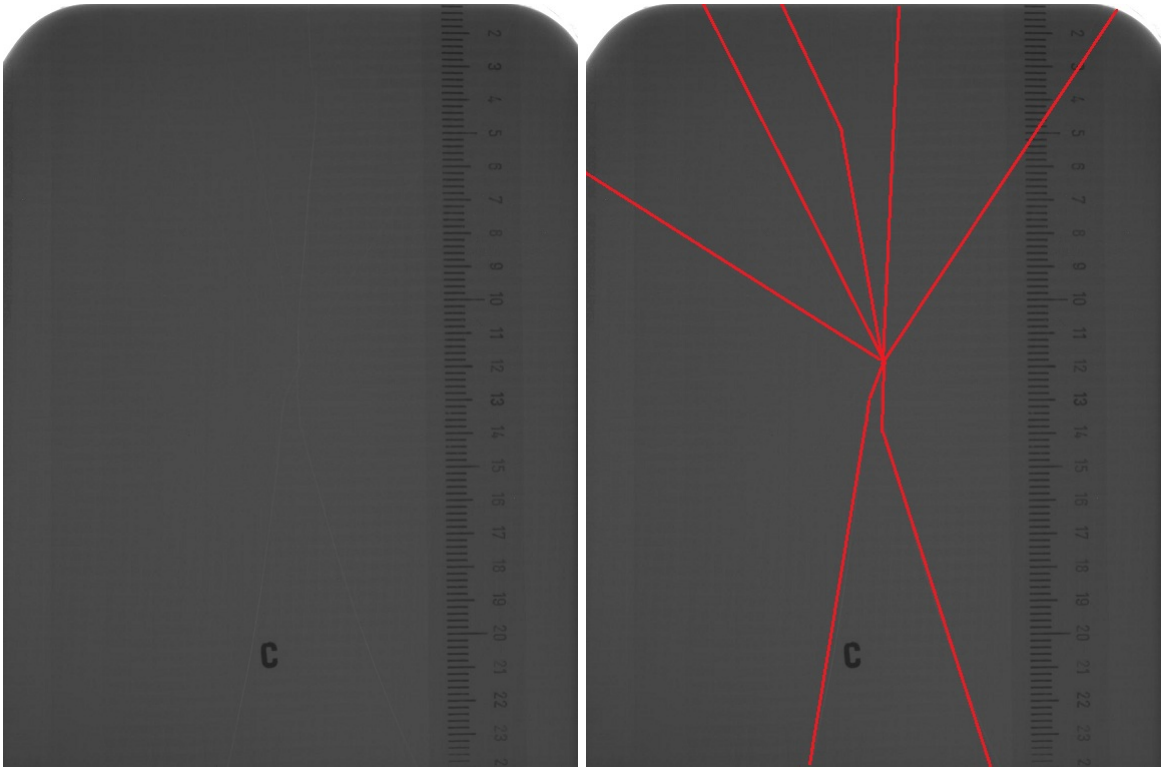

(a) Damaged panel C prior to ballistics impact.

(b) Damaged panel C (cracks marked) prior to ballistics impact.

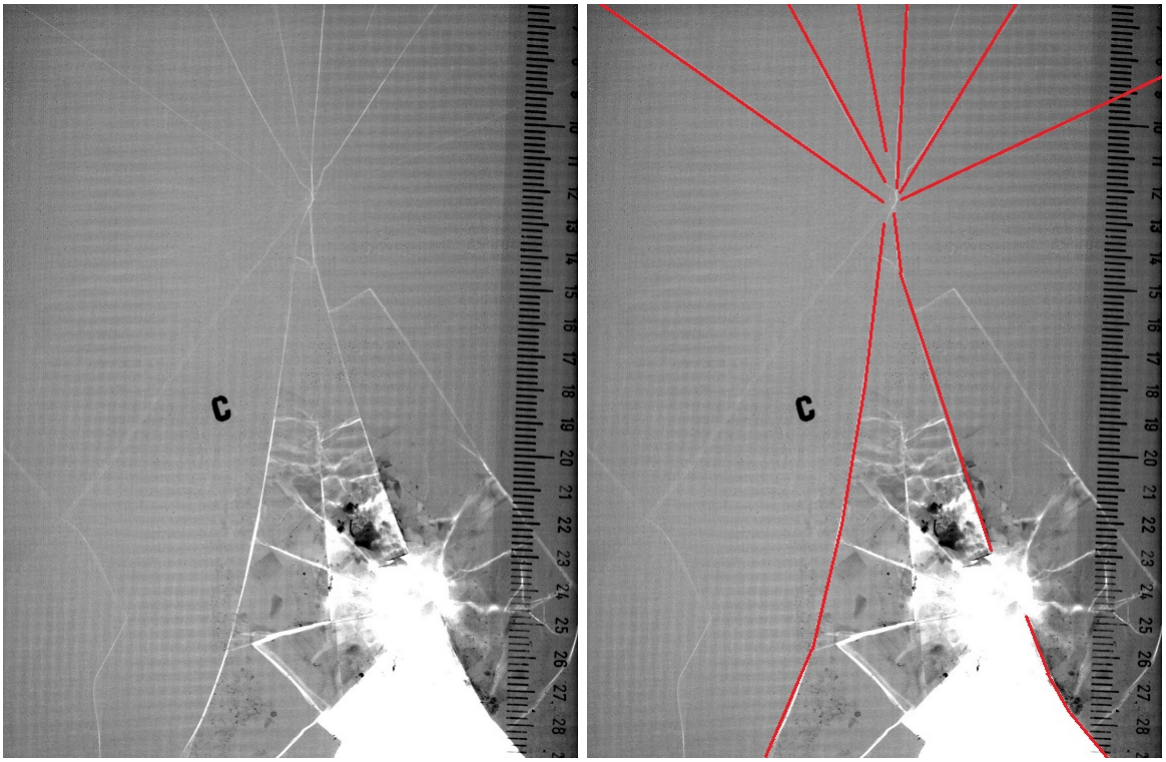

(c) Damaged panel C post-ballistics impact.

(d) Damaged panel C (pre-existing cracks marked) post-ballistics impact.

Figure G.2 X-rays of a damaged ceramic armor panel prior to and post-ballistic impact. (Scales in cm)

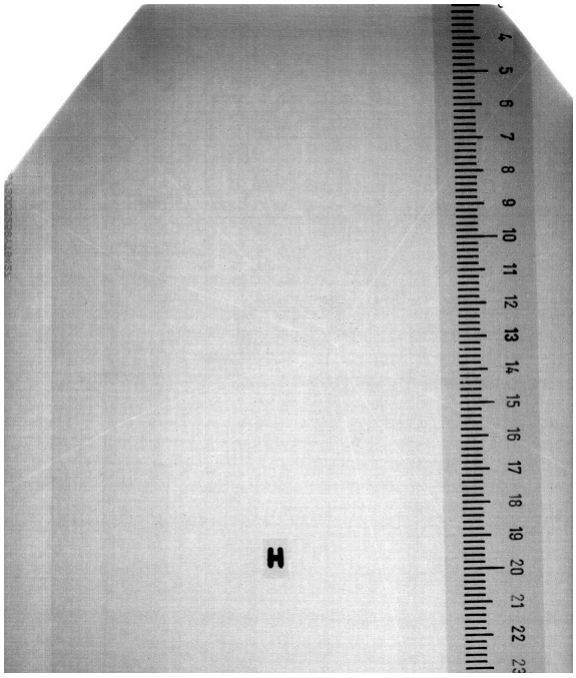

(a) Damaged panel H prior to ballistics impact.

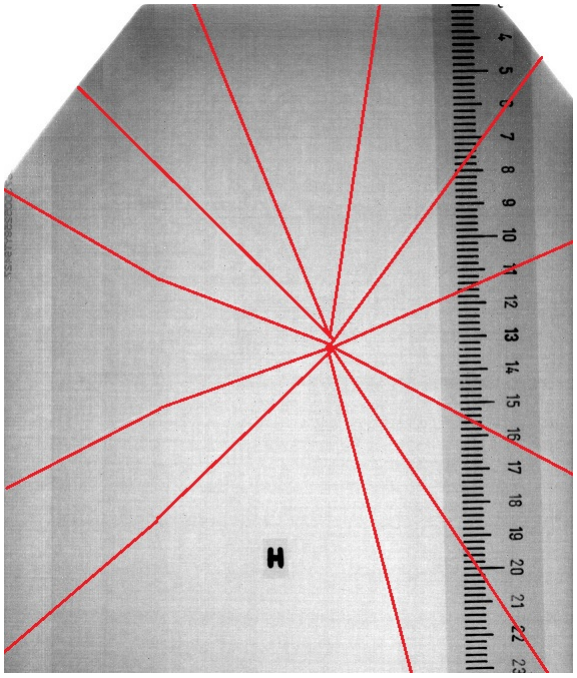

(b) Damaged panel H (cracks marked) prior to ballistics impact.

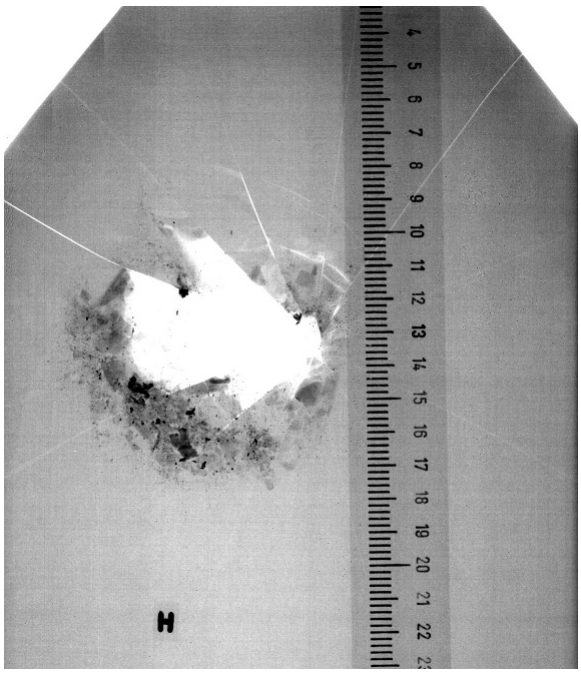

(c) Damaged panel H post-ballistics impact.

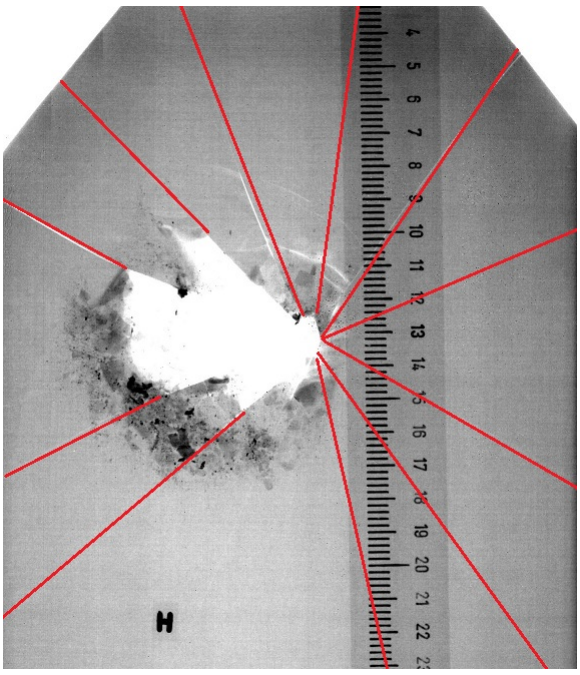

(d) Damaged panel H (pre-existing cracks marked) post-ballistics impact.

Figure G.3 X-rays of a damaged ceramic armor panel prior to and post-ballistic impact. (Scales in cm)

APPENDIX H. DETAILED OUTLINE OF EXPERIMENTAL PROCEDURE

H.1 Equipment

The force transducer and accelerometer employed in the impact experiments were both sensors from PCB Piezotronics. Figures H.1 and H.2 are of the force transducer and accelerometer respectively. The force transducer had a diameter of 0.5" and was rated for up to 5000-lb (22200-N). The accelerometer measured the acceleration in a single axis and was rated for up to 500-g (4900-$\frac{m}{s^2}$). The force transducer had a voltage output corresponding to 1 $\frac{mv}{lb}$ and the accelerometer had a voltage output corresponding to 10 $\frac{mv}{g}$.

Figure H.1 Force transducer employed in impact experiments.

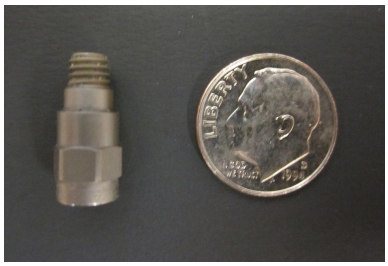

Figure H.2 Accelerometer employed in impact experiments.

Both the force transducer and the accelerometer required the use of a signal conditioner (from PCB Piezotronics). Figure H.3 is a image of the signal conditioner employed. Both instruments connected to a separate signal conditioner and the signal conditioner was connected to an oscilloscope. The oscilloscope employed was a LeCroy Waverunner LT224. Software provided by LeCroy and available from their website free of charge, Scope Explorer v2.25, was used to collect data from the oscilloscope and save on a computer as data files. Data files contained from the oscilloscope contained two columns, a time value and a voltage values, for 50002 data points.

Figure H.3 Signal conditioner intruments connected to.

H.2 Experimental procedure

2x2-in square pieces of medium, high, and super high PSF were cut and placed on a panel of ceramic armor at a location that corresponded to the location of the center of the CPR manikins chest once the armor panel was placed in the carrying vest. Prior to experiments the carrying vest had been fitted such that a location $\frac{1}{3}$ of the way down from the top of the armor panel was located approximately at the center of the manikins chest (as the armor would be positioned if worn by a soldier). The three squares of PSF were stacked on each other and then Scotch Tape was placed on the edges of the PSF to prevent them from moving on the armor panel. The armor panel was then placed inside the carrying vest.

The manikin with armor panel in carrying vest was then placed under the drop tube. The

drop tube had been set such that the spacing between the bottom of the tube and armor panel on the manikin was approximately $\frac{1}{4}$-in. Marks were placed on the outside of all sides of the carrying vest locating the center of the PSF squares. Those markings were used along with markings on the drop tube to align the manikin such that the location on the armor panel with the PSF squares was centered under the drop tube.

The accelerometer was attached to the top of an impactor by applying a small amount of wax to the bottom of the accelerometer and then firmly pressing it to the impactor. This was the recommended way of adhering the accelerometer as per procedures provided by PCB Piezotronics, wax was provided with the accelerometer. After the accelerometer was attached, a small layer of rubber cement was placed around the edge of the accelerometer and allowed to dry. This was done to prevent the accelerometer from popping off of the impactor over repeated impacts. The force transducer was placed inside the machined hole and the bottom of the impactor. The cable connection to the force transducer was placed in a groove that ran along the side of each impactor to keep it out of the way. Pieces of tape were placed on the edge of the force transducer, off of the sensor area, to ensure that it did not come loose from the hole. Figures H.4 and H.5 show the mounting of the accelerometer and force transducer respectively.

Each impactor had an I-bolt screwed into the top of it. Fishing line was attached to the I-bolt which came out the top of the drop tube, around a pulley, and then down the wall to allow for the impactors to be raised and lowered once they were placed in the drop tube. Fishing line was used as it had a high strength but a negligible mass compared to the impactor. For a given drop test, the impactor was raised to a specific height marked on the outside of the drop tube. From that point the impactor was released and impact occurred.

To capture the impact data with the force transducer and accelerometer, the oscilloscope was set to trigger off the accelerometer. An acceleration greater that 20-g triggered the oscilloscope to capture data from both the force transducer and accelerometer. The oscilloscope was offset so it would capture the full profile of the impact event. The Scope Explorer program was then used to obtain data files for the impact.

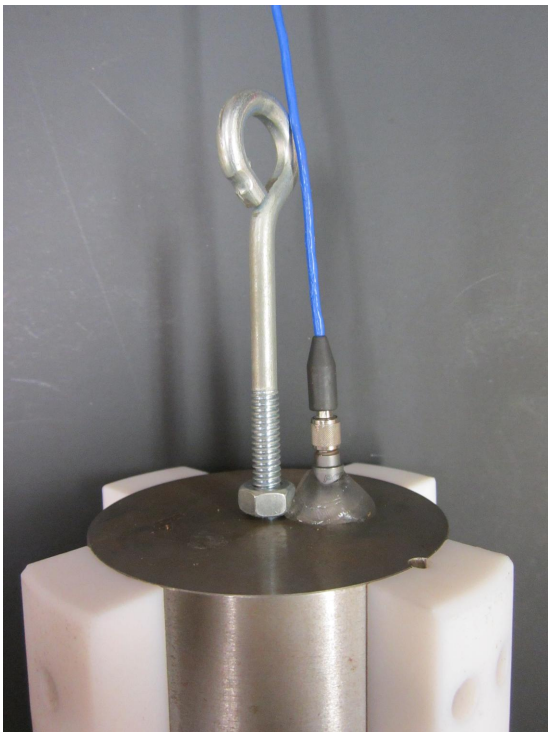

Figure H.4 Impactor with accelerometer attached.

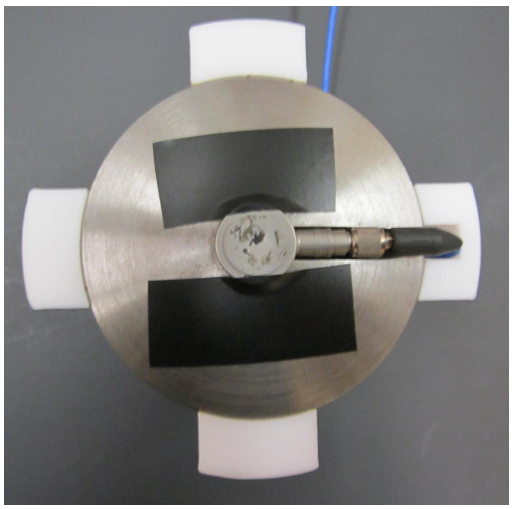

Figure H.5 Impactor with embedded force transducer.

BIBLIOGRAPHY

[1] D. J. Viechnicki, M. J. Slavin, M. I. Kilman, "Development and Current Status of Armor Ceramics", American Ceramic Society Bulletin **70**(6), 1035–1039 (1991)

[2] B. Matchen, "Application of Ceramic in Armor Products", Key Engineering Materials, **122**, 333–334 (1996)

[3] E. Medvedovski, "Alumina Ceramics for Ballistic Protection I", American Ceramic Society Bulletin, **81**(3), 27–32 (2002)

[4] E. Medvedovski, "Alumina Ceramics for Ballistic Protection II", American Ceramic Society Bulletin, **81**(4), 45–50 (2002)

[5] W. A. Gooch, Jr., "An Overview of Ceramic Armor Applications", Ceramic Transactions, **134**, 3–21 (2002)

[6] B. James, "Practical Issues in Ceramic Armor Design", Ceramic Transactions, **134**, 33–44 (2002)

[7] E. Medvedovski, "Armor Alumina Ceramics", Ceramic Transactions, **134**, 91–101 (2002)

[8] S. R. Skaggs, "A Brief History of Ceramic Armor Development", Ceramic Engineering and Science Proceedings, **24**(3), 337–349 (2003)

[9] E. Medvedovski, "Advanced Ceramics for Personnel Armor: Current Status and Future", Ceramic Transactions, **178**, 3–17 (2005)

[10] E. Medvedovski, "Lightweight Ceramic Composite Armour Systems", Advances in Applied Ceramics, **105**(5), 241–245 (2006)

[11] K. Sujirote, K. Dateraksa, N. Chollacoop, "Some Practical Requirements for Alumina Armor Systems", Ceramic Engineering and Science Proceedings, **28**(5), 71–89 (2008)

[12] P. G. Karandikar, G. Evans, S. Wong, M. K. Aghajanian, M. Sennet, "A Review of Ceramic Armor Applications", Ceramic Engineering and Science Proceedings, **29**(6), 163–175 (2009)

[13] R. Brennan, R. Haber, D. Niesz, J. McCauley, "Non-Destructive Evaluation (NDE) of Ceramic Armour: Fundementals and Testing", Ceramic Engineering and Science Proceedings, **26**(7), 223–238 (2006)

[14] J. M. Wells, "On the Role of Impact Damage in Armor Ceramic Performance", Ceramic Engineering and Science Proceedings, **27**(7), 225–236 (2007)

[15] R. Brennan, R. Haber, D. Niesz, G. Sigel, J. McCauley, "Elastic Property Mapping Using Ultrasonic Imaging", Ceramic Engineering and Science Proceedings, **28**(5), 213–222 (2008)

[16] J. M. Wells, "On Continuing the Evolution of XCT Engineering Capabilities for Impact Damage Diagnostics", Ceramic Engineering and Science Proceedings, **28**(5), 203–212 (2008)

[17] T. J. Meitzler, G. Smith, M. Charbeneau, E. Sohn, M. Bienkowski, I. Wong, "Crack Detection in Armor Plates Using Ultasonic Techniques", Materials Evaluation, **66**(6), 555–559 (2008)

[18] K. Schmidt, J. Little, W. A. Ellingson, "Portable Microwave Scanning Technique for Nondestructive Testing of Multi-layered Dielectric Materials", Ceramic Engineering and Science Proceedings, **29**, 179–189 (2009)

[19] K. Schmidt, J. Little, W. A. Ellingson, "Portable Microwave Interference Scanning System for Nondestructive Testing of Multi-layered Dielectric Materials", in *Review of Progress in Quantitative Nondestructive Evaluation* 28*B*, edited by D. O. Thompson and D. E. Chimenti, AIP Conference Proceedings, **1211**, American Institute of Physics, Melville, NY (2009)

[20] N. Haynes, K. Masters, C. Perritt, D. Simmons, J. Zheng, J. E. Youngberg, "Automated Non-Destructive Evaluation System for Hard Armor Inserts of Body Armor", Ceramic and Engineering Science Proceedings, **29**, 211–218 (2009)

[21] S. Bottiglieri, R. A. Haber, "High Frequency Ultrasound of Armor-Grade Alumina Ceramics"', in *Review of Progress in Quantitative Nondestructive Evaluation* 28*B*, edited by D. O. Thompson and D. E. Chimenti, AIP Conference Proceedings, **1211**, American Institute of Physics, Melville, NY (2009)

[22] K. Schmidt, J. Little, W. A. Ellingson, W. Green, "Portable Microwave Interference Scanning System for Nondestructive Testing of Multi-layered Dielectric Materials", Ceramic and Engineering Science Proceedings, **30**(5), 123–133 (2010)

[23] D. Dulay, et al. "Update on Practical Non Destructive Testing Methods for In-Service AQ of Ceramic Body Armour Plates", PASS 2006 (2006)

[24] W. H. Green, H. T. Miller, J. C. LaSalvia, D. P. Dandekar, D. Casem, "Evaluation of Ballistically-Induced Damage in Ceramic Targets by X-Ray Computed Tomography", Ceramic and Engineering Science Proceedings, **29**, 199–210 (2009)

[25] R. E. Brennan, W. H. Green, J. M. Stands, "Nondestructive Evaluation of as Fabricated and Damaged Encapsulated Ceramics", Ceramic and Engineering Science Proceedings, **30**(5), 135–146 (2010)

[26] I. Horsfall, D. Buckley, "The Effect of Through-Thickness Cracks on the Ballistic Performance of Ceramic Armour Systems", Int. J. Impact Eng., **18**(3), 309–318 (1993)

[27] Lieberman, Johnson,"An Analytical Model for Ball-Barrier Impact, Part I: Models for Normal Impact", in Science and Golf II, the Proceedings of the World Scientific Congress of Golf, eds. A.J. Cochran, M.R. Farrally (E&FN Spon), 309-314 (1994)

[28] J. Fisher, D. E. Chimenti, "Simple go/no-go test for subcritical damage in body armor panels", in *Review of Progress in Quantitative Nondestructive Evaluation* 30*B*, edited by D. O. Thompson and D. E. Chimenti, AIP Conference Proceedings, **1335**, American Institute of Physics, Melville, NY (2011)

[29] NIJ Standard-0101.06 (2008)